國立臺灣大學工學院化學工程學系

碩士論文

Department of Chemical Engineering

College of Engineering

National Taiwan University

Master Thesis

利用分子動力學模擬探討水合物晶體界面特性

Interfacial Properties of Methane Hydrate and Water via

Molecular Dynamics Simulations

何垚煌

Yao-Huang Ho

指導教授：林祥泰 博士

Advisor: Shiang-Tai Lin, Ph.D.

中華民國 108 年 7 月

July, 2019

致謝

感謝林祥泰老師。在我懵懂無知時,細心的指導我。從不直接告訴我答案,而是耐心引導,讓我自己想出解決辦法。另外,感謝老師認真聆聽我的意見,提供我一些工作選擇上的訊息與訊息,讓我明白除了工程師之外的道路。

感謝 David Wu 老師,在這兩年期間,於研究方面給予我很多的指導。

感謝旻聰學長帶我進入分子模擬的世界。學長的教學方法,當年的我覺得根本是放牛吃草,總是提個開頭,後面就要自己去想辦法解決。與其說學長教導我分子模擬的知識,倒不如是教導我如何使用 GOOGLE 去找到問題的答案。但對於現在的我來說,卻是萬分感謝。當我成為其他人的學長時,由於覺得當年的我學得太痛苦,所以就直接把所有我會的東西交給弟弟們,但後來才發現他們做了一年甚至快二年了,還常常會問我一些入門級問題,這時才對於學長的教學方法感觸良深。

感謝姿妤,與我一起在旻聰的教學下一同奮鬥的夥伴。很感謝我的碩士生涯有妳的相伴。由於我們進實驗室時,做 MD 的學長們都離開了,所有的東西都是我們兩個重新整理與自己摸索學習的。如果沒有妳我應該會崩潰。想當初我們連 qsub 後連去哪裡找 job 都不知道,還是依靠你偷偷看老師的指令才明白 qstat 的存在。

感謝昌哲。在我碩一時,一起陪我玩恰恰谷,與我分享很多生活點滴,以及時常在我研究有困難時與大仔一起給予我建議。

感謝 Billy。在我碩一還不太會寫 C++時,常常陪我到晚上 11 點,教導我寫程式,真的很感激你。

感謝子芳、軒豪、德謙、大仔、CCK,陪伴我二年的碩士生涯,從頭至尾。

感謝政廷、柏偉,在我碩二時,讓我遇見了你們,我很高興認識你們。

感謝曉丰、浩恩、藍天三個有點瘋瘋癲癲但都很屬害的專題生。你們帶給我很多歡笑與神奇小知識。

感謝亞叡、俊霖、大力行、威霖、旻賢與雲杰學長們在我碩零時給我的幫助。

感謝我父母提供我金錢上的補助,讓我不須煩惱金錢,將心思都放在做研

1

究上，以及在我研究做不出來時，給我加油打氣，真的非常感激。

感謝我自己。這兩年當中，我其實一度想要放棄研究，因為一直做不出東西，覺得自己很沒用。但我還是堅持了下來，碩二的 11 月，終於開始做出了一些成果。我忍受了 18 個月的艱難，最後還是小有成功，把這個研究題目做完。在這過程中，常常會思考著我想要的人生究竟是甚麼樣子。雖然這 18 個月過得很痛苦，但也因為如此，更加明白自己未來不想做什麼，以及想做甚麼事。感謝上帝的安排。

中文摘要

　　分子動態模擬被用來進行研究冰-h 以及甲烷水合物晶體的表面性質。我們特別關注於其熱力學性質以及表面波動的動態性質。根據毛細管波動理論，我們測量出對於冰-h 在 270K 以及甲烷水合物在 285K 下，其界面自由能各為 29.24 與 34.60 mJ/m^2。這個結果與實驗值非常相似。在實驗中，冰-h 在 250K 至 283K 下其界面自由能為 25 至 35mJ/m^2；而甲烷水合物則是在 260K 至 285K 下，其介面能為 31 至 36mJ/m^2。我們的模擬表明，晶體面相對於界面自由能的影響很小，冰-h 和甲烷水合物分別只有 1％和 3％。隨著冰-h 和甲烷水合物晶體的波長增加，表面波的弛豫會漸漸地被毛細波支配。此外，在液相擴散的時間尺度特徵中，甲烷水合物晶體的弛豫時間幾乎是冰-h-晶體的 40 倍。我們將這種差異歸因於復雜的氫鍵生成與斷裂和籠狀結構的水合物的存在。最後，我們通過模擬毛細波動力學來估計動力係數（晶體生長速率取決於過冷度），並將冰-h 和甲烷水合物晶體的動力係數與之前的模擬值與實驗值做比較

關鍵字：表面波動、界面自由能、晶體面相、熱力學、動力學、分子動力學模擬

3

ABSTRACT

Molecular dynamics (MD) simulations were conducted to study the crystal-melt interface of ice and sI methane hydrate crystals. In particular, we focus on both the thermodynamics and dynamics of surface waves. Based on the capillary fluctuation theory, we determined the interfacial free energy of Ice-H (I_h)/water and sI methane hydrate/water to be 29.24mN/m^2 at 270K and slightly higher value, 34.60 mN/m^2 at 285K, respectively. The results are consistent with experiment, 25~35 mJ/m^2 at 250K to 283K for I_h/water interface, and 31~36 mJ/m^2 at 260K to 285K, for the sI methane hydrate/water interface. Our simulations show that the effect of orientation of crystal to interfacial free energy is small, only 1% and 3% for I_h/water and sI methane hydrate/water, respectively. The relaxation of surface waves are dominated by the slow process as the wavelength increases for both I_h and sI methane hydrate crystal. Moreover, in a time scale characteristic for the diffusion of the liquid phase, the relaxation time of the crystal-melt interface of sI methane hydrate crystal is almost 40 times slower than that of I_h crystal. We ascribe this difference to the presence of complicate hydrogen bond network and cage-like configuration of hydrate. Finally, we estimate the kinetic coefficient (rate of crystal growth depends the degree of supercooling) from our simulation of the capillary wave dynamics and compare it with previous simulation studies and with experiments for the case of I_h and sI methane hydrate crystal.

Keywords: Surface Wave; Interfacial Free Energy; Crystal Orientation; Thermodynamics; Dynamics; Simulation.

LIST OF FIGURES

10

LIST OF TABLES

15

Chapter 1   Clathrate Hydrates

1.1   Clathrate Hydrates

From a macroscopic view, clathrate hydrates are a kind of non-stoichiometric crystal solid, in which guest molecules such as methane (CH_4), carbon dioxide (CO_2) or hydrogen can be trapped. CH_4 hydrate can naturally nucleate and grow under the environment of low temperatures and high pressures, like permafrost regions or the deep seafloor below the ocean. Because there are a great amount of methane gas trapped in the hydrate all over the world [1-3], it has been considered as a new potential source of energy

From a microcosmic view, gas hydrate is consisted of gas molecules, usually called guest molecules, are enclathrated by the rigid water cage via hydrogen bonds. The water cage is constructed by polygon rings, for example, the dodecahedron (5^{12}) is composed of twelve pentagons, and the tetrakaidecahedron ($5^{12}6^2$) is composed of twelve pentagons and two hexagons. Using different cages with specific ratio can constitute different types of structure of hydrate, the most common structures of hydrate are structure I (sI), structure two (sII) and structure H (sH), as shown in Figure 1.1-1. For instance, a unit cell of the sI hydrate is composed of two 5^{12} (small) cages and six $5^{12}6^2$ (large) cages. According to the thermodynamics stability, pentagons and tetrakaidecahedron can trap one guest gas, so there are 8 guests in a unit cell of sI under full-occupied cages condition.

Due to the size of guest molecules and the geometry of cages listed in Table 1.1-1, different kinds of guest will form specific hydrate structure which the thermodynamics property is the most stable. For example, the size of guest molecules between 4.2 Å and 6 Å, such as methane, ethane and carbon dioxide, can usually form sI and sII hydrate structures. The larger guest molecule, size in the range of 6.5 Å to 6.95 Å, such as tetrahydrofuran (THF) and propane, can be stabilized in sII hydrate structure.

16

In this work, we only discuss both the thermodynamics and dynamics properties for sI CH_4 hydrate structure under the liquid/solid coexistence condition.
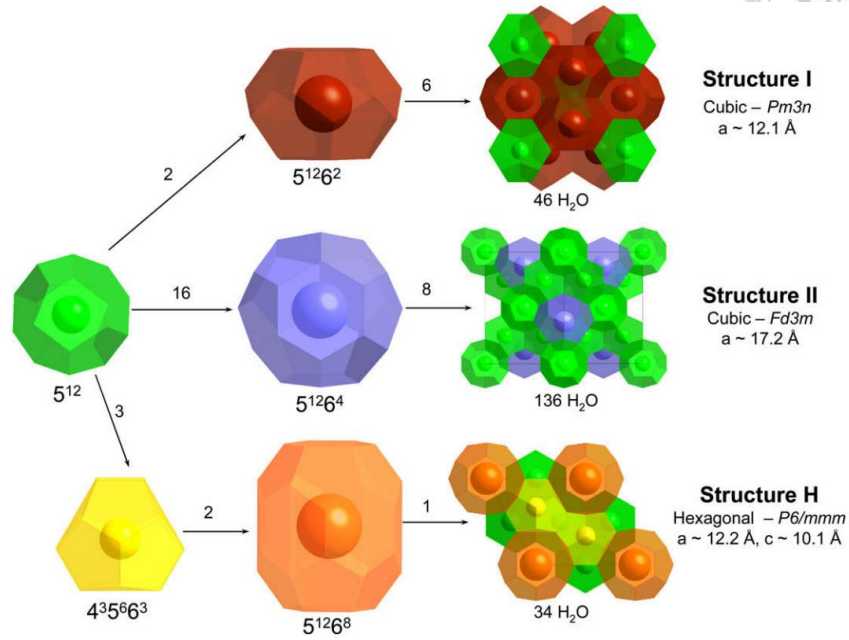
Figure 1.1-1 Different types of cages: pentagonal dodecahedron (5^{12}), tetrakaidecahedron ($5^{12}6^2$), hexakaidecahedra ($5^{12}6^4$), dodecahedron ($4^35^66^3$), icosahedron ($5^{12}6^8$). Different cages with specific ratio can constitute structure I, structure II and structure H [4].

Table 1.1-1 Geometry of cages in different hydrate structure [5].

structure	I		II		H		
Cavity	small	large	small	large	small	medium	large
Name	5^{12}	$5^{12}6^2$	5^{12}	$5^{12}6^2$	5^{12}	$4^35^66^3$	$5^{12}6^8$
No. of cavities/ unit cell	2	6	16	8	3	2	1
Average in radius (Å)	3.95	4.33	3.91	4.73	3.94	4.04	5.79
Variation in radius (%)	3.4	14.4	5.5	1.73	4.0	8.5	15.1
No. of water molecules /cavity	20	24	20	28	20	20	36

17

1.2   Application of Clathrate Hydrates
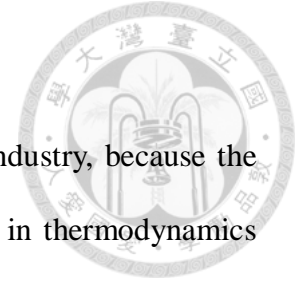
Gas hydrates have been first paid an attention in petroleum industry, because the temperature and pressure of the transporting-petroleum pipeline is in thermodynamics stable region of formation the nature gas hydrates resulting in the blockage of pipelines. [6-8]. However, in recent years, other applications of hydrate, such as gas transportation or direct energy source of methane gas attract much attention.

Although there are lots of different kinds of clathrate hydrates, the CH_4 hydrates are the most common one, which been found in permafrost and sea floors. The amount of methane enclathrated in hydrate and distribute whole the world, so that it is regarded as a new potential energy source [3, 9-11]. The distribution of CH_4 hydrate [12] is shown in Figure 1.1-1. The storage capability of methane in hydrate distributed whole the world is estimated to be around $\sim 3 \times 10^{13}$ m^3 [13], which is almost sane as the shale gas deposits in the USA [14]. Therefore, finding out feasible methods to exploit the methane from CH_4 hydrate is unstoppable, especially for Taiwan. In Taiwan, except for the great amount of CH_4 hydrate [15] discovered under the southwestern offshore Taiwan, there is nearly not found oil, shale gas or any other raw materials. Because of above reason, gas hydrate can become an important energy source for Taiwan.

In addition to being an energy material, hydrate can also be used as a medium of gas transportation. By boxing the gas molecules into the cages, such as natural gas [6, 16], CO_2 [6] and H_2 [17-21], comparing to traditional LNG method, the gas can be transported under a higher temperatures and lower pressures by a solid crystal form directly. Within certain distance, it's the most economical method of gas transportation [22].

In this few years, the issue about environment, such as the emissions of CO_2 and global warming has been paid a lot of attention. Although there are lots of energy source-

methane hydrates spread all over the world, exploiting these resources from the seafloors is concerned by the possibility of forming the tsunami. Furthermore, if the exploited CH_4 leaks into the atmosphere, the degree of global warming caused by CH_4 is more serious than CO_2. In recent years, some scientists propose a new method, called CO_2 sequestration, to overcome the problem of greenhouse gas and extracting CH_4 from the hydrates at the meanwhile. According to phase diagram shown in Figure 1.2-2, it is possible to recover the CH_4 gas from the hydrate and entrap the CO_2 into the cavity of the cage of the original methane hydrate. This method can achieve three goal simultaneously. First, extract the energy resource, methane gas, from the methane hydrate on the seafloors. Seconds, reducing the emissions of CO_2 in the atmosphere retards the global warming. Third, without melting the hydrate in the seafloors, there is not any possibility of occurring tsunami. [23].
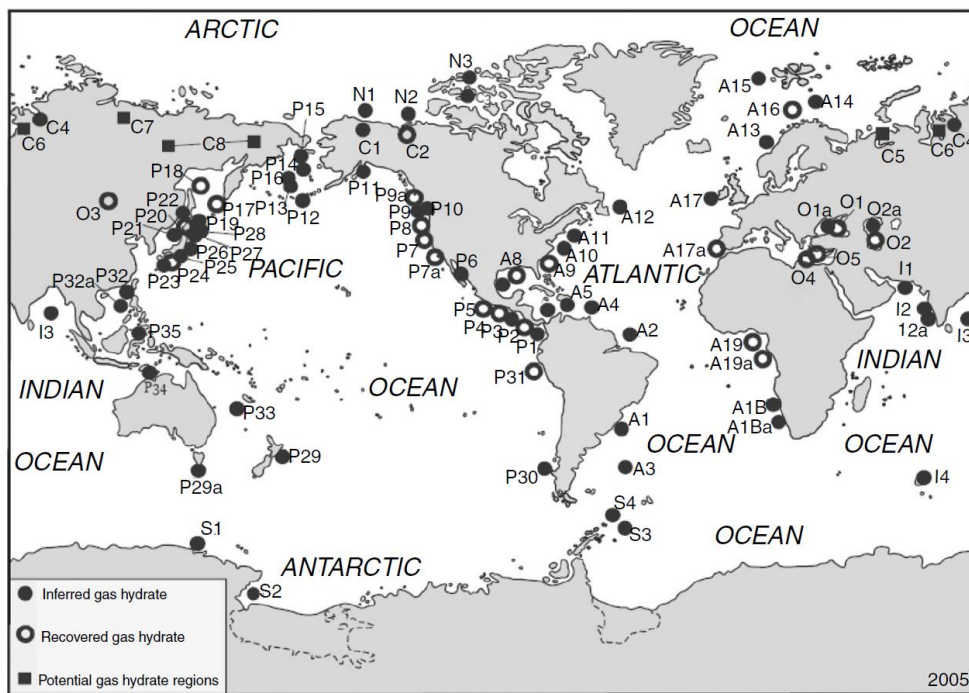
Figure 1.2-1 Distribution of gas hydrate around the world [12].

19
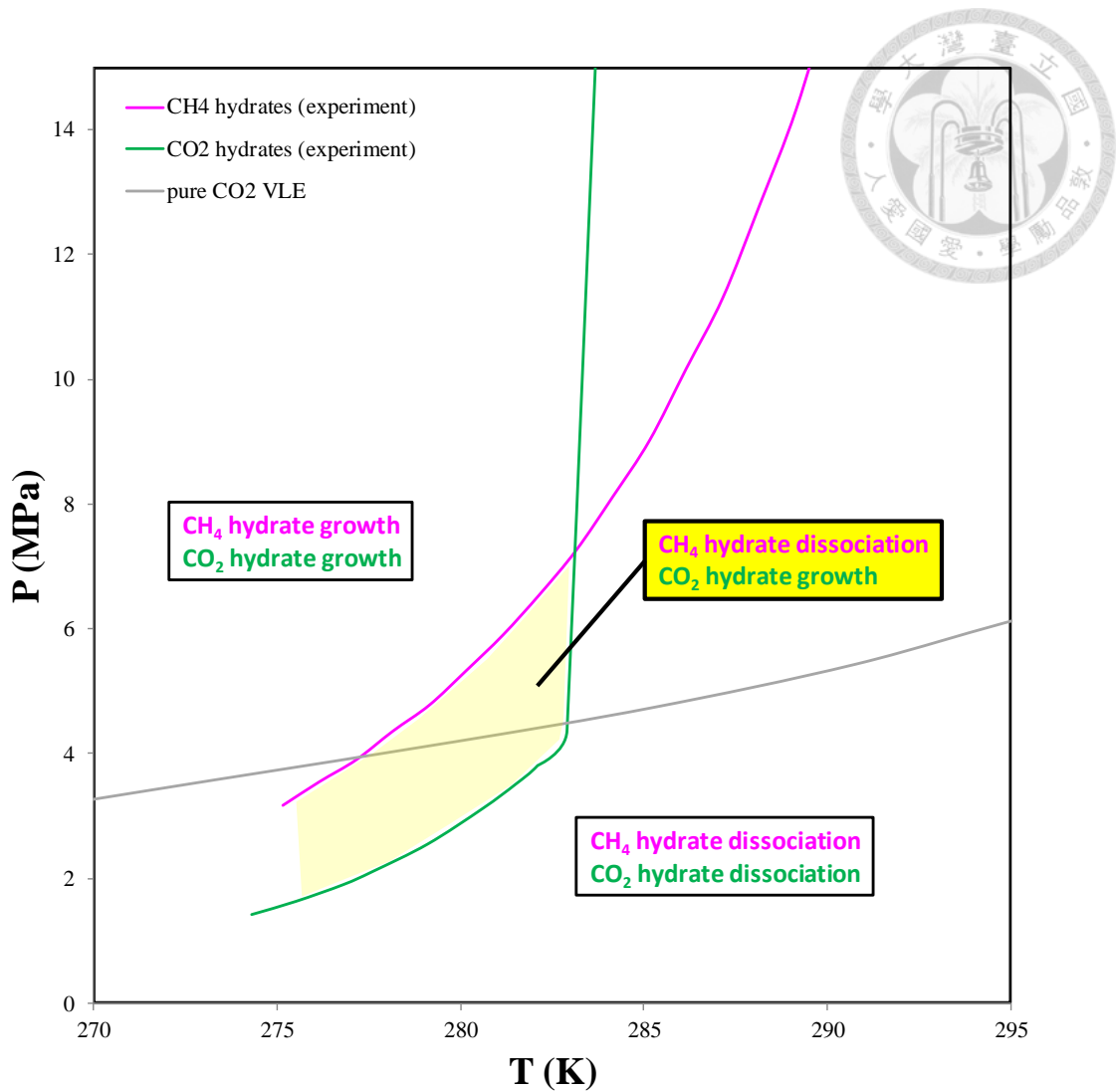
Figure 1.2-2 Phase diagram of hydrates. (pink line: equilibrium line of CH₄ hydrates from experiments; green line: equilibrium line of CO₂ hydrates from experiments; gray line: vapor- liquid equilibrium line of pure CO₂ [12].

1.3   Surface fluctuation of the interface of solid/fluid

The interfacial properties (e.g., stiffness, surface tension) of a crystal-melt interface (CMI) have a great influence on the nucleation and growth of the crystal [24-26]. However, the CMI is far less understood than fluid-fluid interface because the measurements involving CMI are much more challenging with typical experimental instrument and method. It is well accepted that the interfacial free energy between the water and air at normal condition is 72mN/m; however, there is a great discrepancy in the reported interfacial free energy between ice and water at ambient pressure, ranging from 25 to 35mN/m [27-30] The analysis of CMI dynamics is useful for understanding the crystal-growth properties [31]

The CMI interface is not static but undulates due to thermal fluctuations. For length scales below the capillary length, the surface wave (SW) is mainly dominated by the interfacial stiffness known as capillary waves (CW). The equilibrium thermodynamic and dynamics properties of CW at the fluid-fluid interface were studied by Smoluchowski and Kelvin [32]. For the CMI, the study of the CW spectrum provides static properties, like the interfacial stiffness and also the interfacial free energy [31, 33-36].

At smaller length scales and higher frequency, the surface of elastic media exhibits thermal vibration known as the name of Rayleigh wave [37]. These waves are small amplitude but high frequency vibrations that result from the elastic response of the solid. The solid phase is elastic and principally exhibit Rayleigh waves. On the other hands, the fluid phase is viscous and would rather show capillary wave.

Unfortunately, although there are fair amount of theoretical researches in this field, it seems like there is not an appropriate theory can fully describe the CMI dynamics through Rayleigh wave or Kelvin wave theory [38-41]. In 1993, Karma published a theory

21
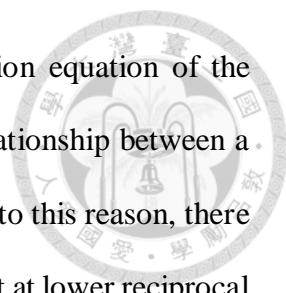
for the relaxation dynamics of crystal-melt CW based on a diffusion equation of the interfacial profile [33]. The theory shows there exist a power law relationship between a characteristic relaxation time and reciprocal space vector. According to this reason, there were fair amount simulations focused on CMI system and showed that at lower reciprocal space vector region, the simulation results agreed with the Karma's theory [31, 34-36, 42] and the interfacial stiffness and interfacial free energy, by means of an analysis of the spectrum of interface fluctuations, calculated by Karma's theory can reproduce the experiment results [36]. Although, there are existing other computational methods to calculate the crystal-fluid interfacial free energy: the cleaving method[43, 44], classical nucleation theory method[45] and mold integration method.[46, 47], it seems like these methods cannot measure the dynamic properties and other interracial properties.

22

1.4   Sodium Dodecyl Sulfate

Sodium Dodecyl Sulfate (SDS) is a kind of famous surfactant which is composed of hydrophilic head group and hydrophobic tail.

In the 1990s, Kalogerakis et al. first reported that the rate of methane hydrate formation could be enhanced by adding SDS.[48]

Okutani et al. later discovered that methane hydrate formed in the unstirred chamber with existing SDS not only can promote the nucleation rate but also worked better than other kinds of surfactant (sodium tetradecyl sulfate, hexadecyl sulfate).[49]

Beside, Yoslim et al. found that in the nucleation process, hydrates do not form as a thin solid layer on the gas/liquid interface without surfactant, however, if adding SDS, the nucleation will occur at the solid(container)/gas/liquid where a three phase intersection place.[50]
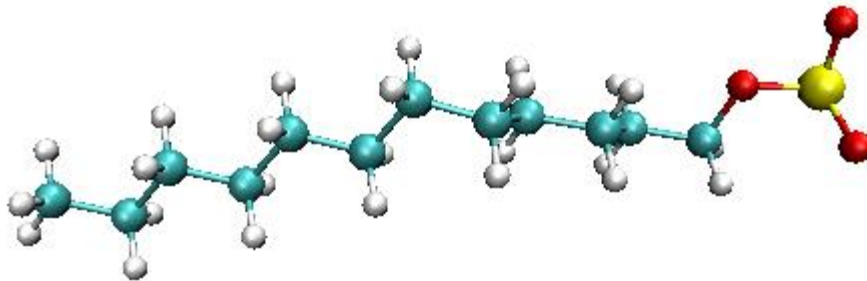
Figure 1.4-1 Structure of the SDS

23

1.5   Motivations
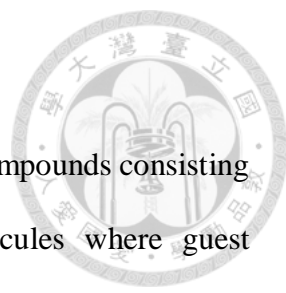
Clathrate hydrates are a kind of nonstoichiometric crystalline compounds consisting of cavities (or cages) formed by hydrogen-bonded water molecules where guest molecules are trapped.[51] The empty lattice (cavities) is thermodynamically unstable, and its existence is stabilized by hydrogen bond resulting from the enclathration of the trapped solutes in its cages. [51] Methane is one kind of guest molecules that stabilizes the water cages in the clathrate hydrate structure. There are three known common hydrate structures: sI, sII and sH. [51] In type I hydrate, methane clathrate hydrates have attracted much attention because the large amount found in nature can be a potential source of energy.[52] However, it is still unknown for the mechanism of hydrate formation (nucleation). There are many efforts made to better understand the nucleation mechanism of gas hydrates. Sloan et al.,[53-56] in order to describe the kinetic data of gas hydrate formation,[57] proposed a hypothetical model based on the labile cluster hypothesis (LCH), where the mixture of guest molecules and labile cages formed by water and then may combine to form a nucleus. Radhakrishnan et al.[58] argued that the high energy barriers of forming larger aggregates from labile clusters should not exist in a nucleation process. They proposed a local structuring hypothesis (LSH), where a group of the guest molecules are arranged in a configuration similar to that in the clathrate phase as a result of thermal fluctuation. When sufficient gas molecules are solved, the arrangement of the gas cluster also helps the surrounding water molecules re-orientate to form a nuclei. The LSH was later supported by the results of molecular dynamics (MD) simulations from Rodger and co-workers.[59] In 2009, Walsh et al.[60] reported the first unconstrained MD simulations of methane hydrate nucleation on the microsecond time scale. They observed that the cages formed in early stage are partial face-shearing with small cages

24
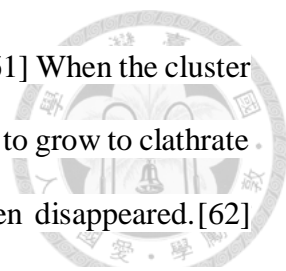
(5^{12}), also proposed the mutually coordinated guests theory (MCG).[61] When the cluster of MCGs size is larger than the critical size, the nuclei will be favorite to grow to clathrate crystalline structure; otherwise, the nuclei will be fluctuate and then disappeared.[62] Jacobson et al. studied the nucleation process using MD simulations.[63] They observed the constant formation and dissociation of guest-rich amorphous precursors (the morphology of a blob or cylinder) as a result of thermal fluctuation. As the size of the blob (or cylinder) becomes larger than some critical size, the blob can continue to grow and solved in water then transform into crystalline clathrate. Such two-step nucleation, or the blob hypothesis (BH), was also supported by atomistic MD simulations of Vatamanu and Kusalik.[64]

Although there were a lot of paper discussing the phenomenon of nucleation; however, the paper studied the interfacial free energy, a crucial parameter in nucleation and growth[45, 65, 66], between hydrate crystalline and water can be counted on fingers[67-69] L.C Jacobson *et al*. calculated the tension by Gibbs-Thomson equation and showed that the tension of amorphous crystal and crystalline are 32 and 36 mJ/m^2, respectively.[68] This result is consistent with the experimental results worked by R. Anderson also using Gibbs-Thomson equation.[67] B.C Knott *et al.* calculated the interfacial tension by classical nucleation theory, and found that the nucleation rate of homogeneous process is pretty low ($3*10^{-111}$ nuclei cm^{-3}s^{-1}). In other words, the homogeneous process is almost impossible reaction path of hydrate nucleation [69]. The curvature of the nuclei in this method theoretically changes during the simulation, but it is treated as constant owing to complication for discussing. Therefore, the value of interfacial energy in this method might not be accurate.

Even if there are handful paper calculating the interfacial free energy between hydrate and water, limited by analysis method, the precision of the interfacial free energy

25
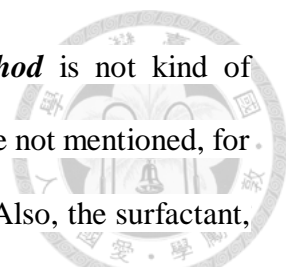
in other methods comparing to ***capillary fluctuation theory method*** is not kind of accuracy and also the further information about hydrate crystalline are not mentioned, for instance, the effect of orientation to hydrate, and kinetic properties. Also, the surfactant, SDS, is verified that can effectively promote the nucleation rate of hydrate forming rate, [48-50] however, the reason that SDS can promote the nucleation rate of CH_4 hydrate is still unknown. Though there are some papers claimed that it is caused by the forming SDS micelle,[70-72] but this hypothesis is soon rebelled from several experiments which indicate that SDS would not form the micelle under hydrate forming condition.[73-75] So far, there is still no any reasonable hypothesis can explain this phenomena. Motivated by these reasons, we use capillary fluctuation method to analyze the CMI between hydrate crystalline and water and also what will be different when SDS adsorb on hydrate interface. In this method, not only the interfacial free energy but also other surface dynamics properties of hydrate crystal can be measured. To get a deeper understanding of the dynamics of the CMI, we analyzed three different systems: ice/water, hydrate/water and SDS/hydrate/water. We show that that relaxation of crystal-melt SW is well described by a double exponential for both two cases. We also show that details of the microscopic dynamics are not important for the relaxation of crystal-melt. Then, we compare the relaxation dynamics of SW for hydrate/water and ice/water with several orientation of CMI. Finally, following the Karma's theory [33] and several method proposed in [31, 35], we estimate the kinetic coefficient (the constant ratio of crystal growth-rate to degree of supercooling) from our measurements of the CW relaxation dynamics.

Chapter 2   Theory

2.1   Molecular Dynamics Simulation

Molecular dynamics (MD) simulation is a kind of powerful method to study the microscopic dynamics behavior on a molecular level. By MD simulation, we can observe how molecules interact with each other directly, which cannot be easily measure in experiment. Therefore, MD simulation is a very suitable tool to analyze the interface properties between hydrate and water.

MD simulation can calculate the interaction force between atoms based on Newton's second law of motion at each simulation time. The standard operation process of the MD calculations is shown as Figure 2.1-1. Initially, the position of each atom in the system should be appointed, and the velocity of each atom will be assign by Maxwell-velocity distribution at specific temperature. The position of next moment can be calculated by current position, velocity and Newton's second law of motion. Since we can calculate the position of each atom in system at every times, in other words, the trajectory of the whole system in a specific time period can be known, so directly observing the microscopic mechanism of molecules is feasible. Furthermore, based on ergodicity, the postulate of statistical mechanics, some macroscopic properties such as total energy of the system or the diffusion coefficient of the molecules can also be obtained by analyzing the enough long ensemble simulation. Comparing the macroscopic results from MD simulation to experiment data, the validity of our simulation can be trusted.
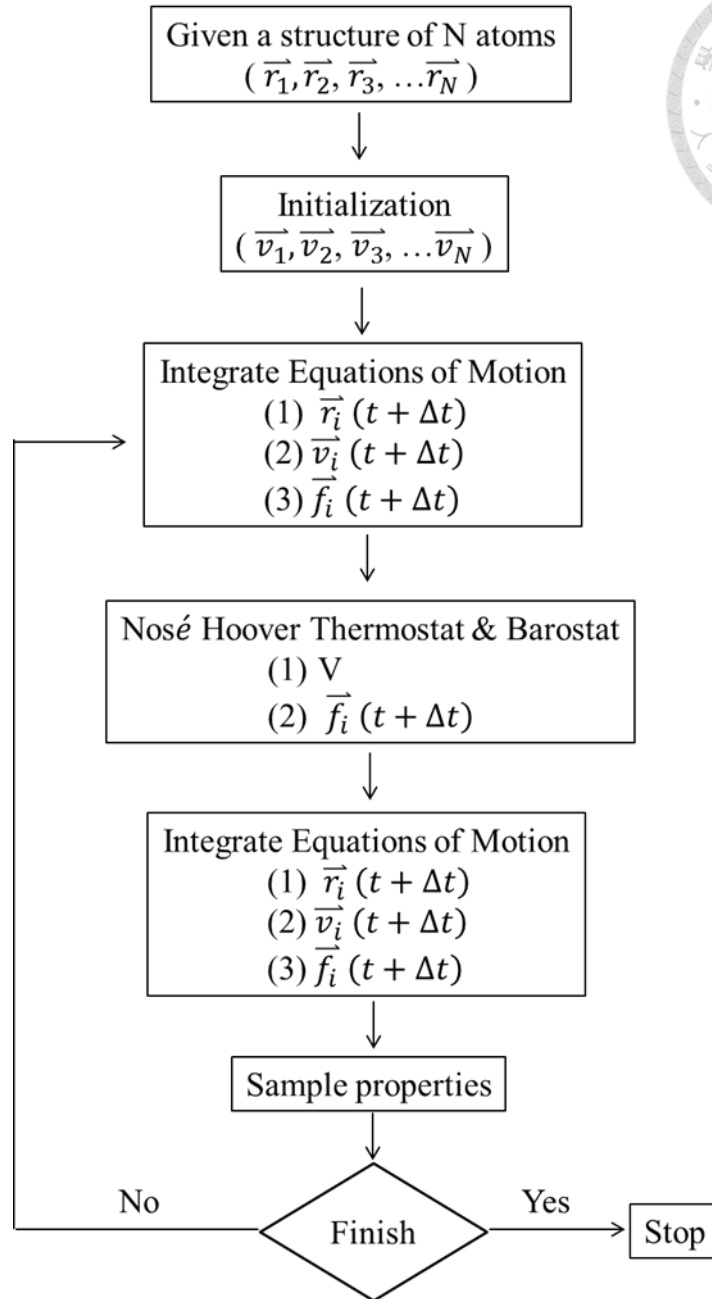
Figure 2.1-1 The flowchart of MD simulation.
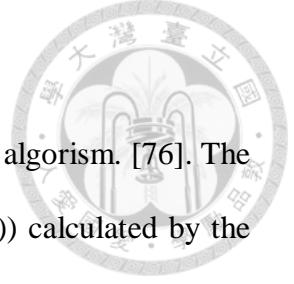
2.2   Integration of Equation of Motion

The Leapfrog integrator method is chosen as our MD integrator algorism. [76]. The positions and velocities are updated by atom-interaction force (**F** (t)) calculated by the positions at time t:

$$\mathbf{v}\left(t+\frac{1}{2}\Delta t\right)=\mathbf{v}\left(t-\frac{1}{2}\Delta t\right)+\frac{\Delta t}{m}\mathbf{F}(t) \tag{1}$$

$$\mathbf{r}(t+\Delta t)=\mathbf{r}(t)+\Delta t\mathbf{v}\left(t+\frac{1}{2}\Delta t\right) \tag{2}$$

The trajectories generated by Leapfrog are identical to the Verlet algorithm[77], shown as equation (3):

$$\mathbf{r}(t+\Delta t)=2\mathbf{r}(t)-\mathbf{r}(t-\Delta t)+\frac{1}{m}\mathbf{F}(t)\Delta t^2+O\left(\Delta t^4\right) \tag{3}$$

The velocity Verlet integrator[77] is one of the other generally used integrator. The equations are listed as equation (4) and (5):

$$\mathbf{r}(t+\Delta t)=\mathbf{r}(t)+\Delta t\mathbf{v}+\frac{\Delta t^2}{m}\mathbf{F}(t) \tag{4}$$

$$\mathbf{v}(t+\Delta t)=\mathbf{v}(t)+\frac{\Delta t}{2m}[\mathbf{F}(t)+\mathbf{F}(t+\Delta t)] \tag{5}$$

2.3   Force field

The force field refers to the parameter sets of potential model, which are calculated from quantum mechanics and experimental data. The potential energy, between any two atoms in the system, can be calculated by deriving force (according to Newton's second law) respect to the relative distance of a pair of atoms, shown as the equation (6):

$$-\frac{\partial U(t)}{\partial \mathbf{r_i}}=\mathbf{F}(t) \tag{6}$$

The potential energy of system, U(t) can be contributed into many parts, shown as equation (7):

29

$$U=E_{\text{non-bond}}+E_{\text{valance}}=E_{\text{vdw}}+E_{\text{coul}}+E_{\text{bond}}+E_{\text{angle}}+E_{\text{dihedral}} \tag{7}$$

The van der Waals interaction (E_{VDW}) and coulomb interaction (E_{coul}) are the non-bond terms, which are generated by inducing-interaction in the space. The valance terms, caused by the existence of valance bond, can be departed into bond interaction (E_{bond}), angle interaction (E_{angel}) and torsion interaction (E_{dihedral}). The atoms can combine with one or more valance bond(s).

The non-bond interactions are neglected for atoms consisted with 1 or 2 valance bond(s) (the bond and angle interactions). For the atoms combined with more than 4 valance bonds, they are considered as in the different molecules so that only the non-bond interactions are considered. For the atoms combined with 3 valance bond, the torsion interaction, caused from the dihedral-angle of valance bonds, is considered and also equal importance with the non-bond interactions, however, non-bond interaction are combined with a weighting factor in order to avoid non-bond interactions too powerful at this circumstance, and this phenomenon is called 1-4 interaction. In this study, there are only H_2O and CH_4 molecules, so we only consider about bond, angle interactions and non-bond interaction.

2.3.1 Non-Bond Terms

The van der Waals interaction in the MD simulation describes the repulsive and dispersive interactions. Lennard-Jones 12-6 function is the most popular model to describe the van der Waals in MD simulation, shown as equation (8).

$$E_{vdw}(r) = 4\varepsilon\left[\left(\frac{\sigma}{r}\right)^{12} - \left(\frac{\sigma}{r}\right)^{6}\right] \tag{8}$$

The model is described by two parameters, ε is the well depth and σ is the collision diameter. The energy is contributed by two parts: r^{-6} represents attractive term and r^{-12} represents repulsive term. The power-law relationship r^{-6} is same as a theoretical

30

treatment for the leading term in Drude model. The r^{-12} variation is quite reasonable for rare gases, however, it is still too steep for hydrocarbons. Even the above reasons, the Lennard-Jones potential is one of the most common model be used, especially in calculation of large system.

Usually we only define the parameters for pure substance, for example, atom A and B. When we want to consider the non-bond interaction between A and B, the parameters, ε_{AB} and σ_{AB} will be determined by mixing rule, shown as equation (9) and (10):

$$\varepsilon_{ij} = \sqrt{\varepsilon_{ii}\varepsilon_{jj}} \tag{9}$$

$$\sigma_{ij} = \sqrt{\sigma_{ii}\sigma_{jj}} \tag{10}$$

The other type of non-bond parameter is the coulomb interaction, it describes the electrostatic energy of atoms, shown as equation (11):

$$E_{coul}(\mathbf{r_{ij}}) = \frac{q_i q_j}{4\pi\varepsilon_0 \mathbf{r_{ij}}} \tag{11}$$

However, the coulomb interaction of point charge doesn't converge in a periodic boundary system since the order of distance-r is -1. To avoid this problem, Ewald et al. proposed the Ewald summation method[78], commonly applied in computational calculation, it can be efficiently summed the electrostatic interactions between particles in simulation system box or their infinite periodic images. In Ewald sum method, the coulomb interaction is constructed by two parts: short range, which can converge quickly in real space, and long range, which converge quickly in reciprocal space, as Figure 2.3-1.

31
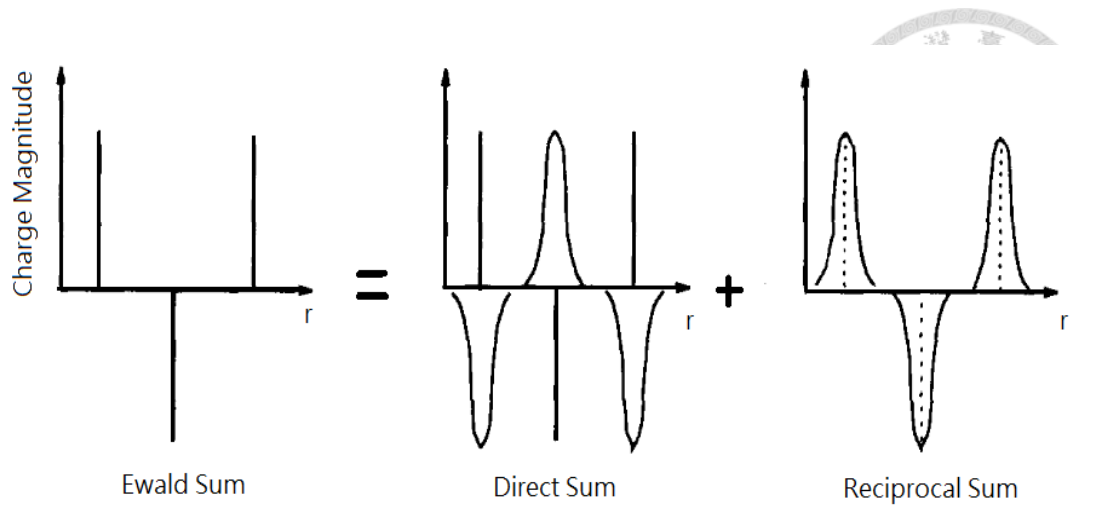
Figure 2.3-1 The component of Ewald summation[78].

By reorganizing the replica sum the coulomb interaction become:

$$E_{coul}(\mathbf{r_{ij}}) = \frac{1}{2}\sum_{\mathbf{m}}^{\infty}\sum_{i=1}^{N}\sum_{j=1}^{N}\frac{q_iq_j\text{erfc}(\sqrt{\alpha}\mathbf{r_{ij}})}{|\mathbf{r_{ij}}+\mathbf{mL}|} + \frac{1}{2V}\sum_{\mathbf{k}\neq 0}\sum_{i=1}^{N}\sum_{j=1}^{N}\frac{4\pi}{k^2}q_iq_je^{-i\mathbf{kr_{ij}}}e^{-(\frac{\mathbf{k^2}}{4\alpha})} - \frac{\alpha^{1/2}}{\pi}\sum_{i=1}^{N}q_i^2$$

(12)

It can predict the molecular dynamics motions more accurately with a carful parameterization. Furthermore, according to molecular dynamics motions, we can find out the interaction between atoms in the microscopic level, and observe the mechanism between particles that cannot directly observe in experiment.

2.3.2 Valence Terms

The bond energy describes the chemical bonding interaction between two atoms. The interaction is imagined as a spring states at the equilibrium length (bond length) l_0 and force constant k, shown as equation (13):

$$E_{bond} = \frac{1}{2}k_l(l-l_0)^2$$

(13)

The angle bending energy is also described by a harmonic potential. The various potential energy is contributed to the degree of deviation of angles from their equilibrium values θ_0, shown as equation (14):

$$E_{angle} = \frac{1}{2}k_\theta(\theta-\theta_0)^2$$

(14)

If the molecule is consisted of more than 3 continuous and linear valance bond, the torsion energy, the rotation of chemical bonds from basic plane, is needed to consider. The value of dihedral energy depends on the difference between dihedral angles and valance bonds, simplified to the following equation:

$$E_{dihedral}=k_\phi \cos m(\phi-\phi_S) \tag{15}$$

Where multiplicity m is 1~3. The ϕ_S is the dihedral angle with the strongest structural energy.

2.4   Ensemble

The concept of ensemble was first introduced into statistical thermodynamics by J.Willard Gibbs[79, 80]. Based on ergodicity, the postulate of statistical thermodynamics, we should analyze a large number of samples to make the simulation results consistent with macroscopic experimental results since not long enough ensemble will be influenced by uncontrollable microscopic details and may lead to different results. There are few different types of ensembles designed to fulfill different macroscopic constraints. For example, isothermal-isobaric ensemble (NPT), system with the same specific pressure and temperature in each sample. Canonical ensemble (NVT) was chosen to simulate the surface fluctuation phenomenon of hydrates at certain volume and temperatures.

2.5   Temperature Thermostat

Nos$é$-Hoover temperature thermostat[81] is applied to simulate a heat bath in order to control the temperature of system during whole simulation in this work. An additional external force ($\mathbf{F_i}$) is applied to atoms in the system to maintain the temperature at target value:

$$\mathbf{F_i}=-\frac{\partial U\left(r_i^{'N}\right)}{\partial r_i^{'}}+\xi m_i \mathbf{v_i} \tag{16}$$

33

$$\dot{\xi} = \frac{3N}{Q} k_B (T\text{-}T_{set}) \tag{17}$$

Where Q is a thermal inertia parameter, reflecting the rate of heat transfer between systems and surrounding heat bath; $\dot{\xi}$ is a friction factor determined by the difference between real-time temperature (T) and desired temperature (T_{set}) and Q. N is the number of particles in the simulation box, and k_B is the Boltzmann constant.

2.6   Pressure Barostat

In this study, there are two types pressure barostats applied. One pressure controlling we used for our system is Berendsen[82, 83]. The Berendsen barostat rescales the coordinates and box vectors every step, or every n_{PC} steps, with a matrix μ, which has the effect of a first-order kinetic relaxation of the pressure towards a given reference pressure P_0 according to equation (18):

$$\frac{dP}{dt} = \frac{P_0\text{-}P}{\tau_p} \tag{18}$$

The scaling matrix μ is given by equation (19):

$$\mu_{ij} = \delta_{ij} - \frac{n_{PC}\Delta t}{3\tau_p} \beta_{ij} \{P_{0ij}\text{-}P_{ij}(t)\} \tag{19}$$

where β is the isothermal compressibility of the system. In most cases this will be a diagonal matrix, with equal elements on the diagonal, the value of which is generally not known. It suffices to take a rough estimate because the value of β only influences the non-critical time constant of the pressure relaxation without affecting the average pressure itself, however, it is the most efficient way to scale a box at the beginning of a run.

The other pressure barostat we used is the Parrinello-Rahman barostat[84]. Parrinello-Rahman approach is similar to the Nosé-Hoover temperature coupling, and gives the true NPT ensemble in theory. By the Parrinello-Rahman barostat, the box vectors as represented by the matrix b obey the matrix equation of motion:

34

$$\frac{db^2}{dt^2} = V\mathbf{W^{-1}}b^{'-1}(P-P_{ref})$$ (20)

Where V is the volume of the simulation box, and W is a matrix parameter that determines the strength of the coupling. The matrices P and P_{ref} are the current and reference pressures, respectively.

Comparing Parrinello-Rahman to Berendsen barostat method, the former controls the system pressure more smoothly and naturally, and the latter one provides a direct pressure controlling, so that there will be a concern for kinetic section. Although there might be a problem for kinetic motions using Berendson, it is a nice choice to quickly let the pressure of system approach to the setting value. After approaching to the target pressure, Parrinello-Rahman is then used to collect the true simulation data.

2.7   MSD (mean square displacement)

To understand whether the guest molecules moved during all nucleation process, to determine the self-diffusion coefficient D_a of particles of type A is important, one can use the Einstein relation[85]:

$$\lim_{t\to\infty} < \|r_i(t) - r_i(0)\|^2 >_{i\in A} = 2ntD_A$$ (21)

Where $r_i(t)$ is the position of atom i at correlation time t and n is the number of dimension of system. Normally, simulations were hold at 3D space in MD simulation, so n is equal to 3.

2.8   ACF (autocorrelation function)

In the data analysis, sometimes we need to consider the correlation between the data. The autocorrelation function is a good method that can tell us the relationship between the data. The below line is the definition:

$$R(\tau) = \frac{<(X_t-\mu)(X_{t+\tau}-\mu)>}{\sigma^2}$$ (22)

35

Where τ is the correlation time, σ^2 is the variance of whole samples, μ is the average of all data and X denotes the sample. When R(τ)<0 and R(τ)>0, it means there is negative-correlation and positive-correlation between the specific time-lag (τ) of the data, respectively. When R(τ)=0, it indicates that there is no correlation between the specific time-lag (τ) of the data.

2.9 Physical meaning for some interfacial technical terms

2.9.1 Surface stress

Surface stress (σ) was first defined by Josiah Willard Gibbs as the amount of the reversible work per unit area needed to elastically stretch an existing surface.

2.9.2 Surface free energy

Surface free energy, which represents the excess free energy per unit area needed to create a new surface. The relation between the surface stress σ, and surface free energy γ, was first pointed out by Shuttleworth [86],

$$\sigma_{ij} = \gamma \times \delta_{ij} + \frac{\partial \gamma}{\partial \varepsilon_{ij}} \tag{23}$$

where σ_{ij} is surface stress tensor, γ is surface free energy, δ_{ij} is kronecker delta and ε_{ij} is strain tensor. It is noteworthy that when a liquid/vapor interface is stretched, atoms can move freely to the interface from the bulk. Therefore, the interface can remain its structural and energetic characters, indicating that derivative term in eq. 23 is negligible. In other words, the surface stress and surface free energy are the same for liquid/vapor system. These two terms have been referred to as the "surface tension."

However, for solid systems (including solid/vapor or solid/liquid systems), the derivative term cannot be neglected. In this case the surface stress and surface free energy are not same.

36
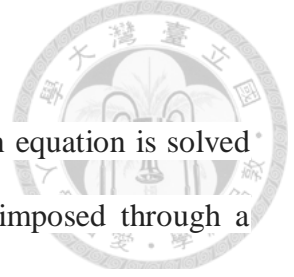
2.9.3 Stiffness

In the modeling of dendritic solidification the thermal diffusion equation is solved subjected to a boundary condition on the interfacial temperature imposed through a velocity-dependent Gibb–Thomson condition. Specifically, the temperature at any point along the moving crystal–melt interface depends on both curvature (R_i) and normal velocity (V_n) according to the equation:

$$T_L = T_M - \frac{T_M}{L}\sum_{i=1,2}[\gamma(\hat{n}) + \frac{\delta^2\gamma(\hat{n})}{\delta\theta^2}] * \frac{1}{R_i} - \frac{V_n}{\mu(\hat{n})} \tag{24}$$

where T_M is the melting temperature and L the latent heat of melting per unit volume. The second-term on the right-hand side of equation (24) represents the change of the local equilibrium melting point due to the curvature of the interface, where $\gamma(\hat{n})$ is the excess free-energy of the solid–liquid interface, θ_i are the local angles between the normal direction of the average interface and the normal directions on the local-interface, and R_i are the principal radii of curvature. The kinetic coefficient, $\mu(\hat{n})$, is defined to be the proportionality constant between the interface undercooling (T_M-T_L), and the normal velocity, V_n, of a planar interface for a given crystallographic growth direction $\hat{n}$.

The second-term of Equation. (21), $\gamma(\hat{n})$ denotes the energy needed to create the new interface and the second differential term originates from the energy needed to rotate locally the interface from its average orientation, respectively. The sum of these two terms defines as interfacial stiffness, $\widetilde{\gamma}$.

2.10 Calculation of surface stress from MD simulation

For a planar interface perpendicular to the z-axis, surface stress σ is given by[87],

$$\sigma = \frac{1}{n}\int_{-\infty}^{\infty}[P_N(z) - P_T(z)]dz = \frac{L_z}{n}[\overline{P_N} - \overline{P_T}] \tag{25}$$

37

Where $P_N = P_{zz}$ and $P_T = \frac{P_{xx}+P_{yy}}{2}$, L_z is the length of z-direction of the system and n is the number of interface.

2.11 Mold integration method

Even if the thermodynamics condition of a system is under two or more phase coexisting region, it is hard to observe the phase change of single phase system in molecular simulation due to the high energy barrier for creating a new phase.

To overcome this problem, the mold integration method was developed.[46, 47] In this method, it defines a kind of particles, called mold particles (or wells). There is an artificial non-bond interaction force between well and oxygen atom (takes I_h/water for example), so that the system can easily overcome the nucleation energy barrier. Because it is adjustable for the interaction force between well and atom, in other words, the progress that a system creates a new phase could be controlled so that the work needed to create the new surface can be determined by thermodynamics integration.

In order to apply the thermodynamics integration, the potential energy of the system is defined the following terms:

$$U(\lambda) = U_{pp}(r_1 \dots \dots r_N) + \lambda U_{pm}(r_1 \dots \dots r_N; r_{w_1} \dots \dots r_{w_{N_W}}) \tag{26}$$

where N is the number of particles and N_w the number of wells; r_1 ……r_N denotes the positions of all particles and r_{w1} …… $r_{w_{Nw}}$ the position of the wells (which are fixed during the simulation); U_{pp} is the potential energy between the atoms in the system (except the wells) and U_{pm} is the potential energy between the specific kind of atom and wells, in addition, this potential term is pair additive; λ is the degree of coupling between the specific kind of atom and wells, and the number is from 0 to 1.

$$U_{pm}\left(r_1 \dots \dots r_N; r_{w_1} \dots \dots r_{w_{N_W}}\right) = \sum_{i=1}^{N} \sum_{w_j=1}^{N_w} u_{pw}(r_{iw_j}) \tag{27}$$

38

where $u_{pw}(r_{iwj})$ is a square-well interaction between the ith particle and j^{th} well, and this

term also depends on the r_{iwj}, the distance between their center

$$u_{pw}\left(r_{iw_j}\right) = \begin{cases} -\varepsilon, & if \ r_{iw_j} \leq r_w \\ 0, & if \ r_{iw_j} > r_w \end{cases} \tag{28}$$

where r_w and ε are the radius and depth of the wells, respectively. In other words, r_w is the

range that wells can influence the specific atoms and ε is the magnitude of attractive force,

both of two parameters are adjustable parameters.

Now, applying the thermodynamics integration to the wells, the free energy

difference between the fluid and plus the interaction between the well and atoms, ΔG_m,

can be obtained.

$$\Delta G_m = \int_{\lambda=0}^{\lambda=1} d\lambda \langle \frac{\partial U(\lambda)}{\partial \lambda} \rangle_{\lambda,N,P_N,T} \tag{29}$$

Since the applying wells, the interface will be generated. The ΔG_m is departed into the

free energy changing caused by generating the interface, ΔG_s, and the interaction between

the well and atoms, the latter term is simplified by $-N_w\varepsilon$.

$$\Delta G_m = \Delta G_s - N_w\varepsilon \tag{30}$$

$$\Delta G_s = N_w\varepsilon + \int_{\lambda=0}^{\lambda=1} d\lambda \langle \frac{\partial U(\lambda)}{\partial \lambda} \rangle_{\lambda,N,P_N,T} \tag{31}$$

Based on the fundamental concept of free energy, the interfacial free energy is the free

energy caused by new interface creating, so that

$$\Delta G_s = 2A\gamma_{iw} \tag{32}$$

The physical meaning of pre-factor 2 is there are two interfaces generated when a new

phase created.

$$\gamma_{iw} = \frac{1}{2A}(N_w\varepsilon + \int_{\lambda=0}^{\lambda=1} d\lambda \langle \frac{\partial U(\lambda)}{\partial \lambda} \rangle_{\lambda,N,P_N,T}) \tag{33}$$

Combining equation (28) and equation (29), the equation (33) can be written as:

$$\gamma_{iw} = \frac{1}{2A}\left(N_w\varepsilon - \int_{\varepsilon=0}^{\varepsilon=\varepsilon_m} d\varepsilon \langle N_{fw}(\varepsilon)\rangle_{N,P_N,T}\right) \tag{34}$$

Where $N_{fw}(\varepsilon)$ is the number of the specific atoms filled in wells.

2.12 F4 order parameter

Some configurations are constructed by same species, for instance, the hydrate, ice-h, ice-c and water are all consisted by H_2O. In order to discriminate the difference among these construction, order parameters are used.

F4 order parameter is used to distinguish the hydrate-like, fluid-like of H_2O typically. The definition of F4 is listed below:

$$F4 = \langle cos3\phi\rangle \tag{35}$$

Where ϕ is the dihedral angle H^a–$O^a \cdot \cdot O^b$–H^b from two neighboring H_2O molecules (<3.5 Å), with H^a and H^b are the farthest hydrogen atoms on each of the water molecules.
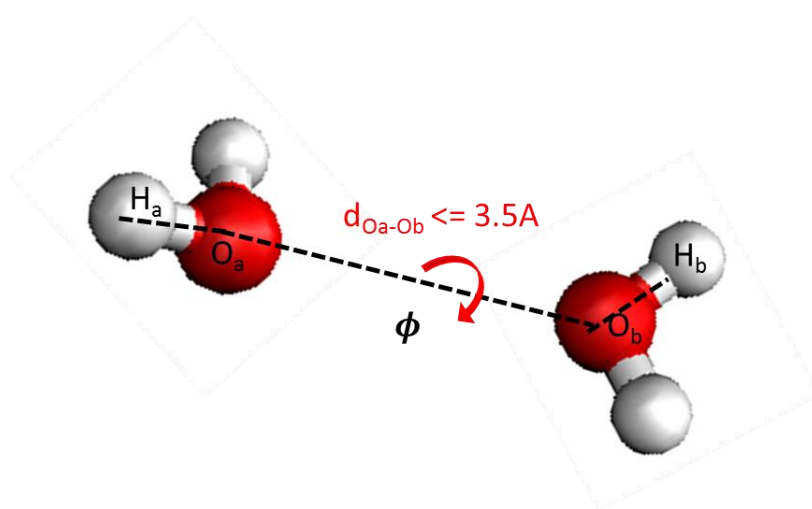
Figure 2.12-1 Illustration of criteria of F4 calculation

2.13 Capillary Fluctuation Theory

In order to calculate the interfacial free energy between solid crystalline and fluid, we use the capillary fluctuation theory.[33, 42]

Before we discuss the capillary fluctuation theory, there are some parameters should be

40

defined. First of all, the local surface position, or interface height is defined as $h(v_n)$, where v_n is discrete position along with the direction of wave propagation (i.e., x_n represents that discrete position along with wave propagation is forward to x direction). Detail explanations are written and shown in Figure 2.13-1.
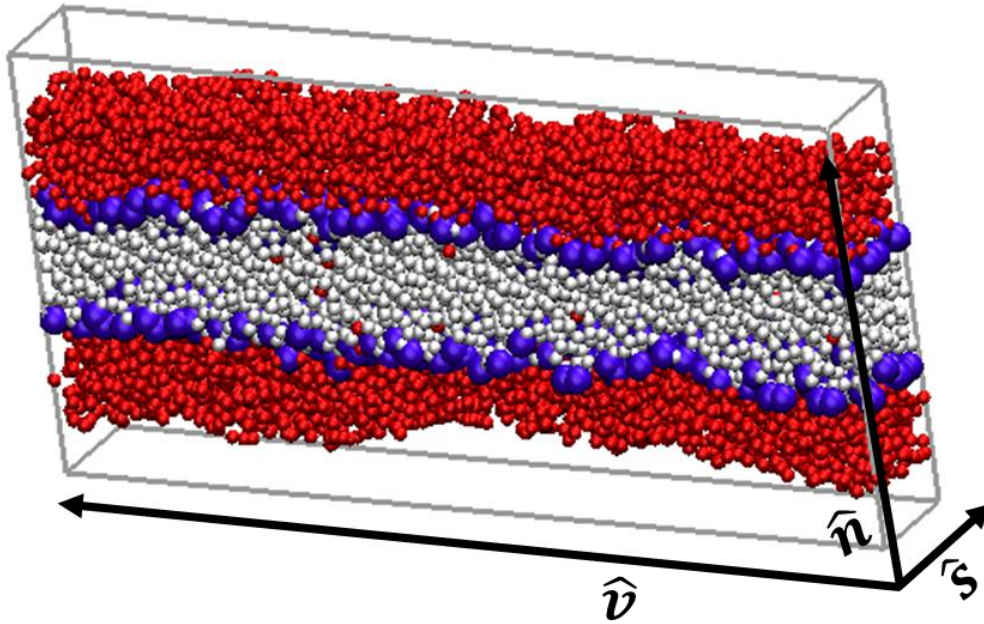
Figure 2.13-1 Snapshot of a typical configuration for capillary wave simulation. Only represents oxygen atom of H_2O. Particles colored by red denotes fluid-like, colored by white if they have crystalline behavior, and colored by blue represents the interface position. The symbols $\hat{v}, \hat{s}$ and $\hat{n}$ represent wave prorogation direction, the shortest depth length direction, and normal vector direction of CMI, respectively. L_v, L_s. and L_n denotes the length of simulation box along with $\hat{v}, \hat{s}$ and $\hat{n}$, respectively.

The interface profile is then applied to Fourier transformed, and Fourier modes h_q are defined as:

$$h_{q_k}(t) = \frac{1}{N} \sum_{n=1}^{N} h(v_n, t) e^{i q_k v_n} \tag{36}$$

where N is the number of discretization points along the wave propagation direction ($\hat{v}$) of the simulation system, each wave mode is associated with a reciprocal space vector, q_k, and defines as $2\pi k/L_v$ where k is a nature number (1,2,3 etc.), and v_n is L_v*n/N (n runs from 1 to N). Small q_k represents low frequency or large wave length vice versa.

The capillary fluctuation theory points out that there is a relationship between h_q and the interfacial stiffness, $\tilde{\gamma}$.[33, 42]

$$\langle |h_q|^2 \rangle = \frac{k_B T_M}{A\tilde{\gamma}q^2} \tag{37}$$

where $A=L_v*L_s$ is the interfacial area. The calculated stiffness depends on the crystal plane that is exposed to the fluid and on the direction along which the wave propagates.

We apply the stiffness, calculated from previous step, into the original definition of stiffness:

$$\tilde{\gamma}(\hat{n}, \hat{v}) = \left(\gamma(\hat{n}) + \frac{\delta^2 \gamma(\hat{n})}{\delta \theta^2} \right) \tag{38}$$

where θ are the local angles between the normal direction of the average interface and the normal directions on the local-interface, see Figure 2.13-2. In order to obtain the interfacial free energy through equation (24), it is necessary to consider the variation of the interfacial free energy with surface orientation, $\gamma(\hat{n})$ and $\gamma(\theta)$. We will carefully discuss this topic in the next section.

42
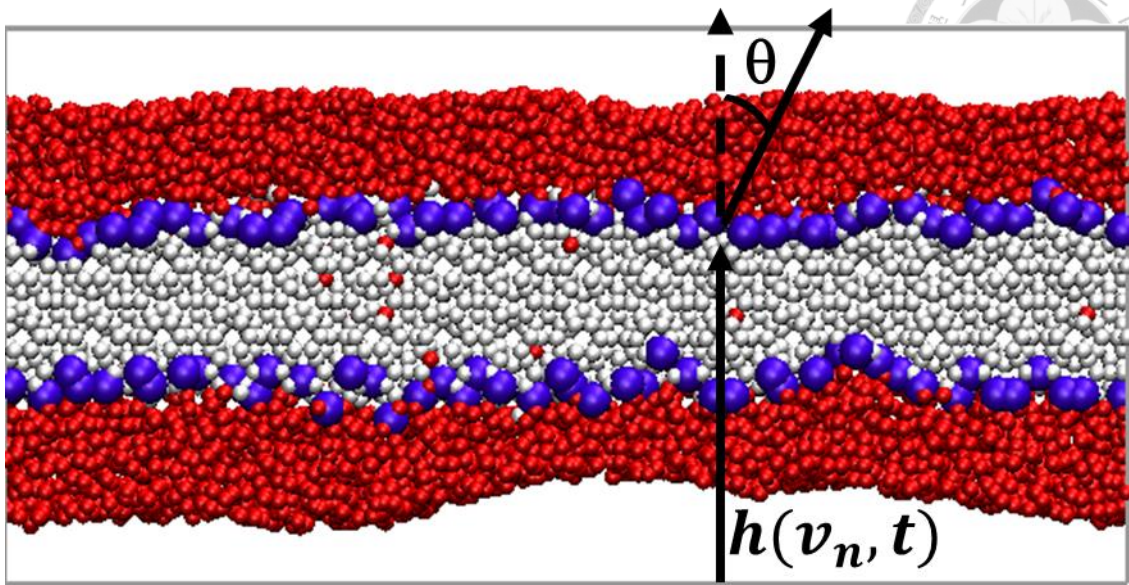
Figure 2.13-2 Illustration the $h(v_n, t)$ and θ. Snapshot of a configuration of a hydrate slab in equilibrium with liquid water, and the color symbols are as same as Figure3.

The dynamics of interfacial waves, the time-dependent autocorrelation function of h_q is then defined as:

$$f_q(t) = \frac{\langle h_q(0) h_q(t)^* \rangle}{\langle h_q(0) h_q(0)^* \rangle} \tag{39}$$

This function shows information about the relaxation behavior of the surface wave of each mode. Because of h_q is effected by both $\hat{n}$ and $\hat{v}$, $f_q(t)$ also depends on t, q, $\hat{n}$ and $\hat{v}$, however, we usually use Miller index to represent the crystalline orientation, so that we can write as $f_q \equiv f(t, q, (h\,k\,l), [i\,j\,k])$. One the f_q is known, we can use exponential equation to fit the equation and get the relaxation time of mode, τ.

The capillary wave theory indicates that:

$$\frac{1}{\tau} = \frac{\mu \tilde{\gamma} T_m}{\Delta H_m \rho} q^2 \tag{40}$$

where ΔH_m denotes the molar melting enthalpy, ρ is the crystal density and μ is the coefficient of the degree that crystal growth rate in a supercooled state ($v = \mu \, \Delta T$).

43

Apply all the parameters into equation (40), then the kinetic coefficient of crystal can be obtained.

Chapter 3 　 Computational Details

3.1 　 Models

We constructed 22 different models, A1 ~ G3 are labeled, using commercial software. Material Studio 5 was used to create the systems and MD were performed by Gromacs 4.5.5.[88, 89]

Table 3.1-1 The composition and simulation targets of model A1~G3.

Target of simulation	Model	Composition	Number of phase
Melting point of sI methane hydrate & I_h	A1	$1344H_2O$	2
	A2	$1656H_2O + 250CH_4$	3
Diffusivity of H_2O	B1&B2	$2112H_2O$	1
Heat of fusion for sI methane hydrate & I_h	C1/C2	$2112H_2O$	1
	C3/C4	$368\ H_2O+64CH_4$	1
Mold integration of I_h	D1	$1792\ H_2O+128mold$	1
	D2	$768\ H_2O+128mold$	1
	D3	$1792\ H_2O+128mold$	1
Capillary fluctuation of I_h	E1	$8064H_2O$	2
	E2	$9216H_2O$	2
	E3	$15360H_2O$	2
	E4	$9216H_2O$	2
	E5	$10800H_2O$	2

45
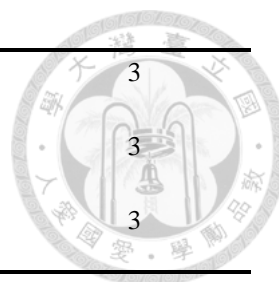
Capillary fluctuation of sI methane hydrate	F1	$16556H_2O + 2720CH_4$	3
	F2	$11170H_2O + 2022\ CH_4$	3
	F3	$9464\ H_2O + 1760\ CH_4$	3
Capillary fluctuation of SDS/sI methane hydrate	G1	$32SDS + 16556H_2O + 2720CH_4$	3
	G2	$32SDS + 11170H_2O + 2022\ CH_4$	3
	G3	$32SDS + 9464\ H_2O + 1760\ CH_4$	3

There are two things should be notable−First, the initial ice structure is zero-dipole and generated based on the rule proposed by *Hayward et al.* [90] Second, the zero-dipole of sI methane hydrate structure created based on **Takeuchi. F et al**.[91]

3.1.1   Models for melting point of sI CH₄ hydrate & Iₕ

The two- phase model A1, as shown in Figure 3.1-1, consisting of a I_h solid phase and a pure H_2O phase were used in this study to observe the melting point of I_h. The solid phase contained $6 \times 3 \times 3$ unit cells of perfect I_h hydrate and was created following the both *Hayward* rules. [90] and Bernal-Fowler ice rules [92] , and the pure H_2O zone totally composed of 864 molecules, which stayed in liquid phase under our simulation conditions. The size of this model was 27.26 Å $\times$23.62 Å $\times$65.00 Å .
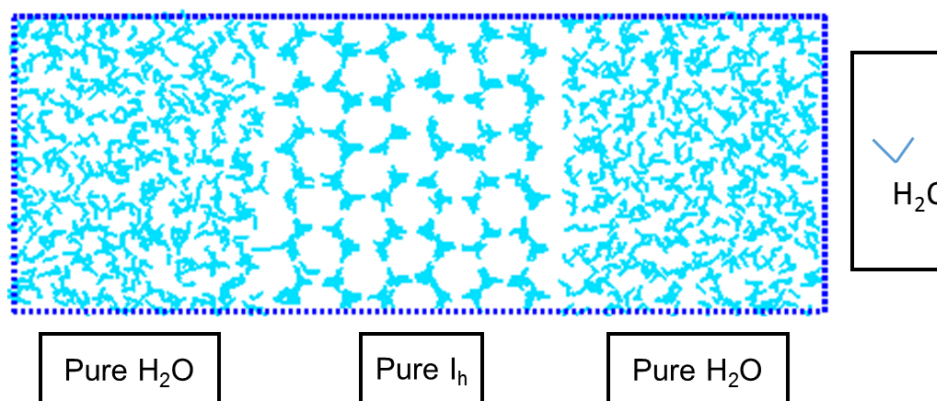
Model A1

Figure 3.1-1 Models for melting point of I_h crystal.

46

The four- phase model A2, as shown in Figure 3.1-2, consisting of a CH_4 solid phase, a pure CH_4 phase, a pure H_2O phase and a H_2O/CH_4 mixture phase were used in this study to observe the melting point of CH_4 hydrate. The solid phase contained $2\times2\times1$ unit cells of perfect sI methane hydrate and the cavities filled with 32 CH_4 molecules and created following the both Bernal-Fowler ice rules [92] , the pure H_2O zone composed of 738 molecules, the pure CH_4 zone composed of 90 molecules, and the H_2O/CH_4 mixture phase was consisted of 736 molecules and 128 molecules, respectively. The size of this model was 23.74 Å $\times$23.74 Å $\times$150.00 Å .

Model A2
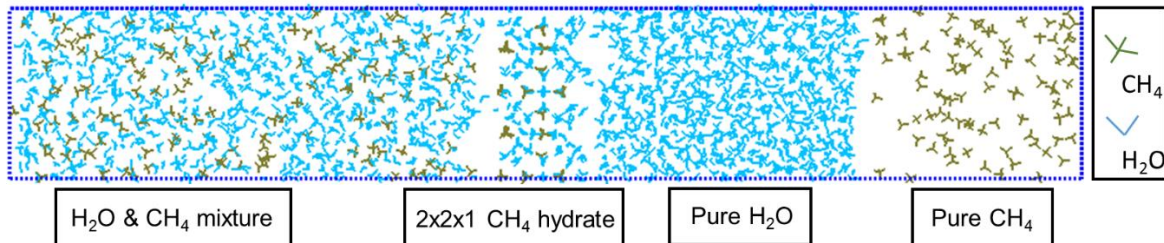
Figure 3.1-2 Models for melting point of CH_4 hydrate crystal.

3.1.2 Models for diffusivity of H_2O at different melting condition

After finding out the melting point of both I_h and CH_4 hydrate phase at specific pressure, the diffusivity of H_2O molecules at the each of two melting point conditions is also needed. Calculating the diffusivity is not only can check the accuracy of force field, but also used in the calculation of dynamics property for capillary fluctuation theory.

The single- phase model B1&B2, as shown in Figure 3.1-3, consisting of a pure H_2O phase, composed of 2112 molecules, was used in this study to observe the diffusivity of H_2O at the melting point condition. The size of this model was 40.00 Å $\times$40.00Å $\times$40.00 Å .

47
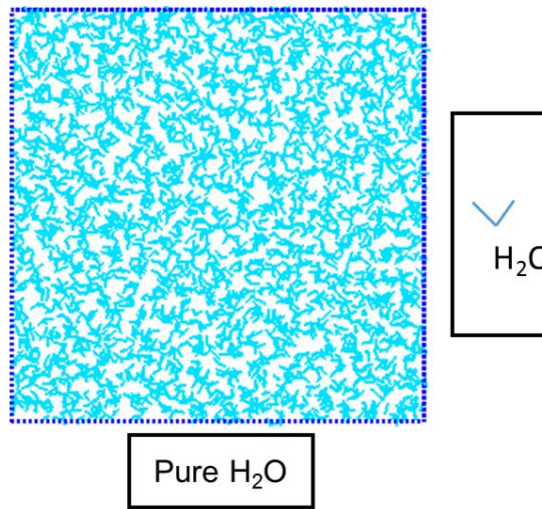
Figure 3.1-3 Models for diffusivity of fluid-like H_2O at melting condition of I_h and CH_4

hydrate

3.1.3 Models for heat of fusion of I_h & sI methane hydrate

There is another property, heat of fusion of solid phase, can be also used in confirming the accuracy of force field. Moreover, heat of fusion of crystal is also another parameter used in the calculation of dynamics property for capillary fluctuation theory.

There are two sets of single- phase model C1/C2 & C3/C4, as shown in Figure 3.1-4 and Figure 3.1-5. C1 and C3 consisting of a pure solid I_h and pure CH_4 hydrate crystal phase, respectively. C2 and C4 are the totally melting configuration of C1 and C3, respectively. In other words, the heat of fusion of crystal of I_h and CH_4 hydrate can be obtained by comparing the difference of enthalpy energy of both C1/C2 and C3/C4 system, respectively. The size of C1/C2 model was $27.05\,\text{Å} \times 31.23\text{Å} \times 29.44\,\text{Å}$, and that of C3/C4 model was $23.74\,\text{Å} \times 23.74\text{Å} \times 23.74\,\text{Å}$.

48
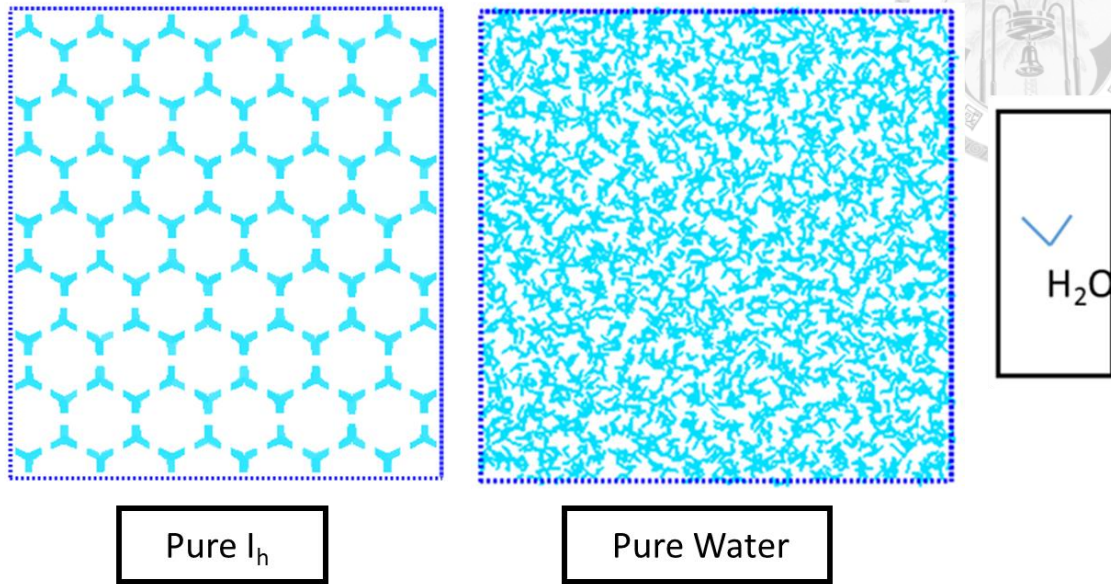
Figure 3.1-4 Models for heat of fusion of I_h hydrate.
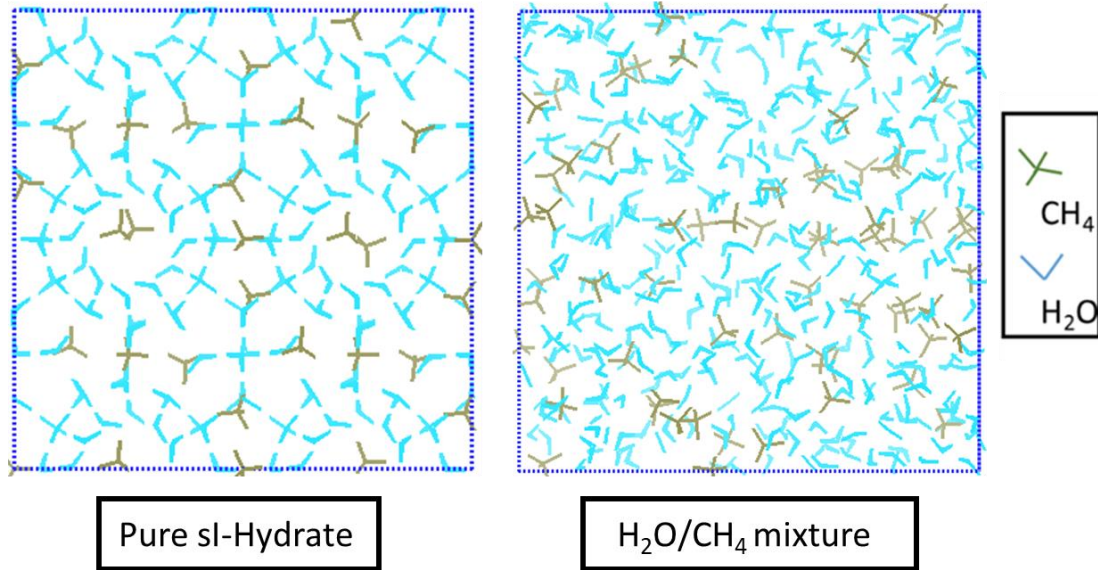
Figure 3.1-5 Models for heat of fusion of CH_4 hydrate.

3.1.4 Models for mold integration method of H₂O system

The one-phase model D1 ~ D3, as shown in Figure 3.1-6, consisting of a pure H_2O phase was used in this study to observe the interfacial free energy of different orientation I_h/water interface. The pure H_2O zone stayed in melting point condition during whole

49

simulation. The parameters of size and composition about this set of models are listed in
Table 3.1-2.

Table 3.1-2 System size and composition for the models of mold integration

Interface orientation	L_x (Å)	L_y (Å)	L_z (Å)	H_2O numbers	Mold numbers
pI	36.37	50.43	29.63	1792	128
pII	25.44	31.22	29.44	768	128
basal	36.37	31.35	47.66	1792	128
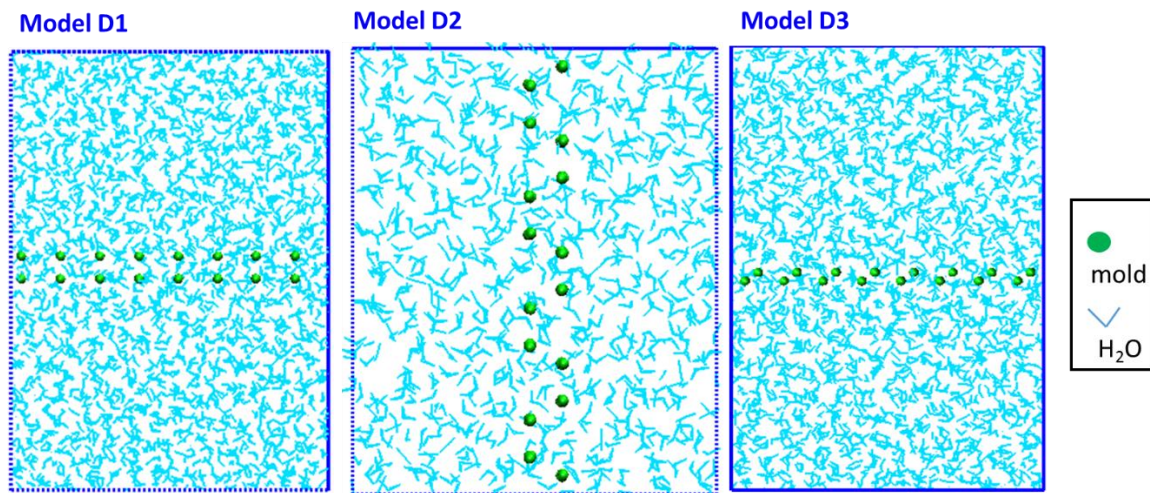
Figure 3.1-6 Models for mold integration of pI (D1), pII (D2) and basal (D3) plane of
I_h/water. The snapshots of all Figures are viewed from side of normal direction of
interface.

3.1.5 Models for capillary fluctuation method of I_h/water

The two-phase model E1 ~ E5, as shown in Figure 3.1-7, consisting of a pure H_2O phase
and pure I_h phase were used in this study to observe the fluctuation of interface between
fluid/solid phase, then interfacial free energy of different orientation I_h/water interface
can be calculated from the fluctuation data. The I_h/water systems stayed in melting point

50

condition during whole simulation. The parameters of size and composition about this set of models are listed in Table 3.1-3.

Model E1 ~ E5
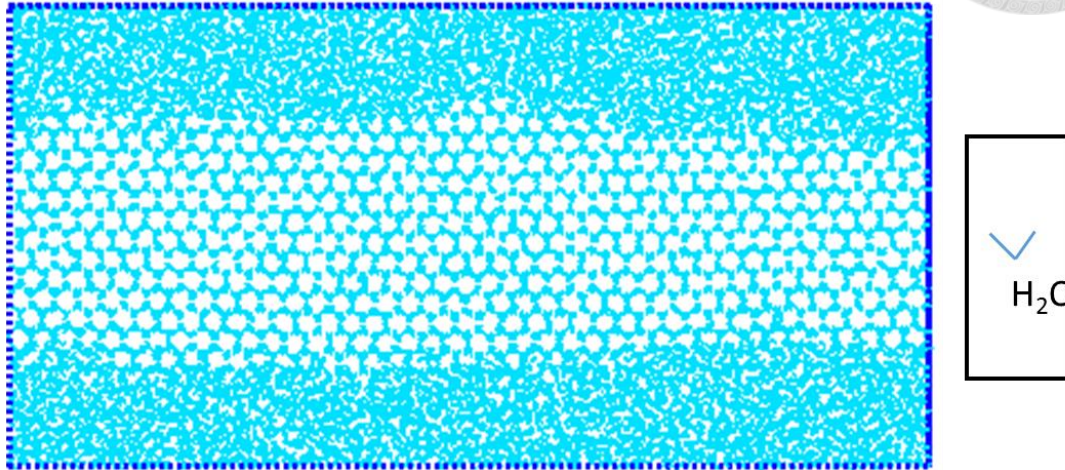
Figure 3.1-7 Models for capillary fluctuation of different orientation interface of I_h/water.

Table 3.1-3 The system size and composition for the models of capillary fluctuation for I_h/water system. The Miller index in the square bracket and parenthesis indicate the direction parallel to the direction of propagation of surface wave, and the direction parallel to the normal of the interface, respectively.

Interface orientation	L_s (Å)	L_v (Å)	L_n (Å)	H_2O numbers
[pI](basal)	18.151	165.242	85.805	8064
[basal](pII)	25.44	177.755	90.932	9216
[pII](pI)	29.587	181.548	90.97	15360
[basal](pII)	23.608	177.532	69.781	9216
[pI](pII)	22.190	196.688	78.776	10800

51

3.1.6 Models for capillary fluctuation of sI methane hydrate/water

The three-phase model F1 ~ F3, as shown in Figure 3.1-8, consisting of a pure CH_4 phase, H_2O/CH_4 mixture phase and pure sI methane phase were used in this study to observe the fluctuation of interface between water/hydrate-crystal phase, then interfacial free energy of different orientation methane hydrate/water interface can be calculated from the fluctuation data. The methane hydrate/water systems stayed in melting point condition during whole simulation. The parameters of size and composition about this set of models are listed in Table 3.1-4.

Model F1 ~ F3
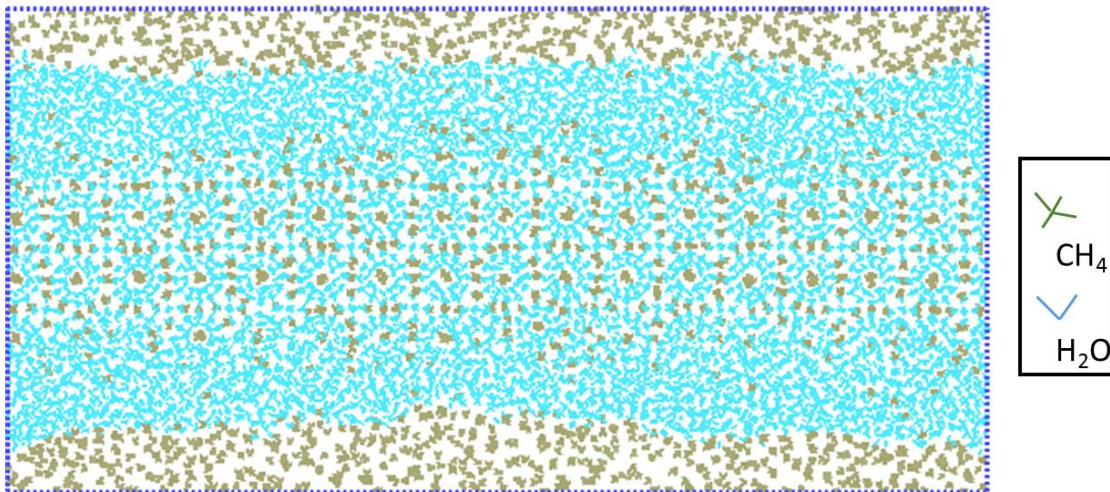
Figure 3.1-8 Models for capillary fluctuation of different orientation interface of

methane hydrate/water

Table 3.1-4 The system size and composition for the models of capillary fluctuation for

methane hydrate/water system.

Interface orientation	L_s (Å)	L_v (Å)	L_n (Å)	H_2O numbers
[110](100)	34.00	170.613	118.326	16556

52

[110]($\bar{1}$10)	24.212	171.363	117.836	11170
[010](100)	24.091	191.105	94.186	9464

3.1.7 Models for capillary fluctuation of SDS/methane hydrate/water

The three-phase model G1~G3, as shown in Figure 3.1-9, consisting of a pure CH_4 phase, H_2O/CH_4 mixture phase and pure sI methane phase which covered by around 30% of full coverage of SDS on surface were used in this study to observe the fluctuation of interface between water/hydrate-crystal phase, then interfacial free energy of different orientation methane hydrate/water interface can be calculated from the fluctuation data. The SDS/methane hydrate/water systems stayed in melting point condition during whole simulation. The parameters of size and composition about this set of models are listed in Table 3.1-5.

Model G1~G3
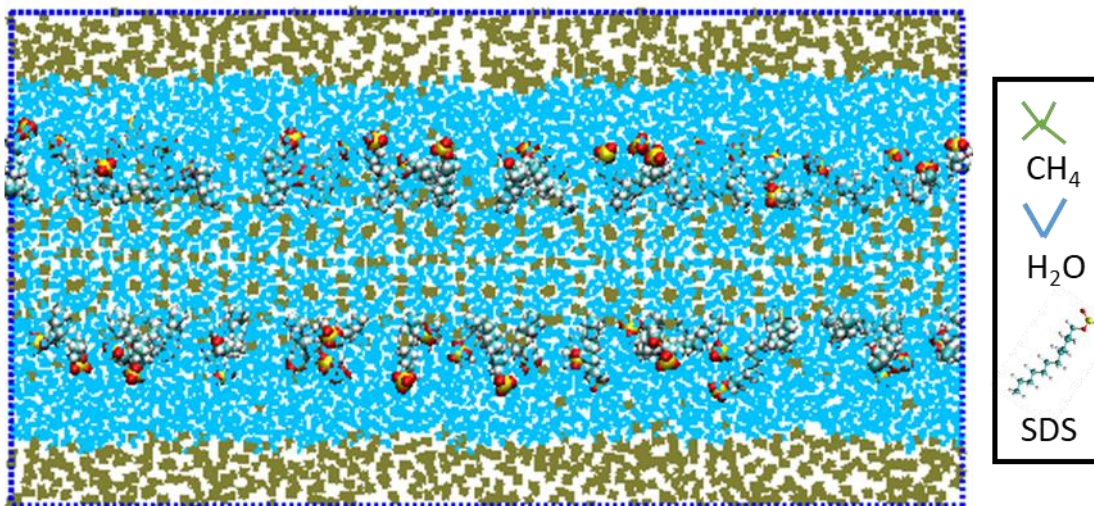
Figure 3.1-9 Models for capillary fluctuation of different orientation interface of

SDS/methane hydrate/water

Table 3.1-5 The system size and composition for the models of capillary fluctuation for

methane hydrate/water system.
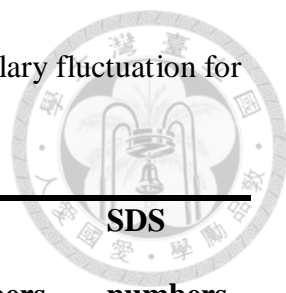
Interface orientation	L_s (Å)	L_v (Å)	L_n (Å)	H_2O numbers	SDS numbers
[110](100)	34.00	170.613	134.69	16556	32
[110]($\bar{1}$10)	24.212	171.363	135.443	11170	32
[010](100)	24.091	191.105	98.945	9464	32

3.2 The setting of temperature and pressure condition

Before starting the main simulation, doing the following steps can let the system shown as Figure 3.2-1. The initial structure was first energy minimized. A short, 200 ps, NVT simulation was then conducted at 200 K to relax extra-stresses in the system. The temperature was then increased to the desired value at a rate of 0.5 K ps^{-1} using NPT simulation at desired pressure. This was followed by a long, up to 10 ns NPT simulation to approach equilibrium state. The Nose–Hoover thermostat is used to maintain the temperature of the system throughout the simulation. The Berendsen barostat was applied to the third step in order to efficiently close to target pressure, and Parrinello-Rahman barostat was applied in the fourth and fifth steps to maintain the system at equilibrium. It is notable that the leap frog algorism was used for all ensemble, integrator time fixed at 1fs. PME and Lennard-Jones potential energy were used to calculate the intermolecular interaction and the long-range Coulomb energy, respectively. The cut-off of PME and LJ is 0.95nm.

For different purpose, different setting of target temperature and pressure was given to each part of simulation, the detail of setting was shown as Table 3.2-1.
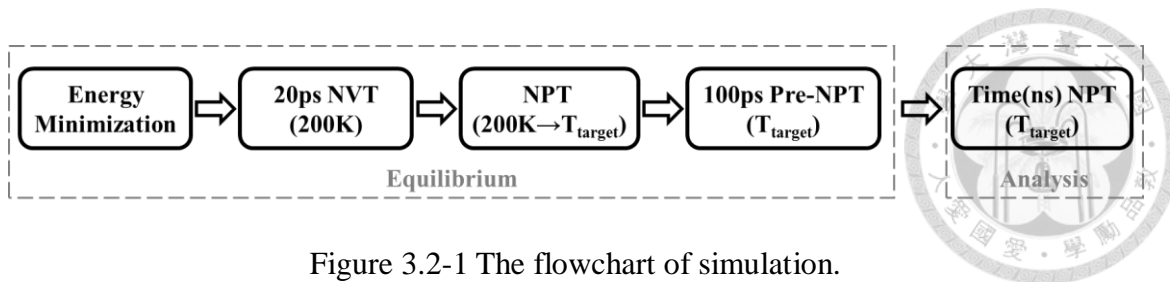
Figure 3.2-1 The flowchart of simulation.

Table 3.2-1. The composition and simulation targets of model A1~A2, B1~B2, C1~C4,

D1~D3, E1~E5, F1~F3 and G1~G3

Target of simulation	Model	P (bar)	T (K)	Simulation Time (ns)
Melting point of sI methane hydrate & I_h	A1	1	268~272	60
	A2	110	280~288	60
Diffusivity of H_2O	B1	1	270	10
	B2	110	285	10
Heat of fusion for sI methane hydrate & I_h	C1 & C2	1	270	10
	C3 & C4	110	285	10
Mold integration of I_h	D1 ~D3	1	270	1.5
Capillary fluctuation of I_h	E1 ~ E5	1	270	335
Capillary fluctuation of sI methane hydrate	F1~F3	110	285	840
Capillary fluctuation of SDS/sI methane hydrate	G1~G3	110	285	235

3.3   Method to generate the solid/liquid coexistence system

In order to get no extra-surface stress solid/liquid coexistence system, the most important is to generate no-extra surface stress crystalline. The detail of creating no extra-stress crystal are listed below:

55
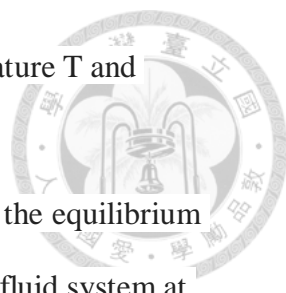
(1) The solid phase was equilibrated at the reference melting temperature T and pressure P using the anisotropic NPT ensemble.

(2) The L_v and L_s of simulation box of fluid phase should be fixed at the equilibrium length of solid phase. Then, following the step (1), simulated the fluid system at reference T and P using NP_nT simulation (n indicates the normal direction of the contact plane).

(3) Carefully connected the equilibrium solid and fluid phase, then fixed L_v, L_s and performed a short run of NP_nT ensemble simulation. After these three steps, the density of solid and fluid phase would equilibrium at reference T and P.

3.4   Force Field

TIP4P-ICE [93] four site model force field was chosen in this study to describe the molecular interactions of H_2O molecules. For TIP4P-ICE force field, water molecules were described as a rigid body, and the reported melting point of ice was 272K, with good consistency to experiment data. OPLS-AA [94] all atom force field was for CH_4 molecules. Generally, the off-diagonal terms (ε and σ) between atoms from different molecules is gotten by geometric mean, shown as equation (9) and (10), but for some special case, we will modify the off-diagonal terms to get a better result which is much closer to the experiment data. All the force field parameters we used are listed in Table 3.4-1. The Mold molecules is a kind of user defined molecules, which is applied into the mold integration method.

Table 3.4-1 Parameters used in this work: (a) Van der Waals and Coulomb (b) modified

cross term (c) bond (d) angle

56
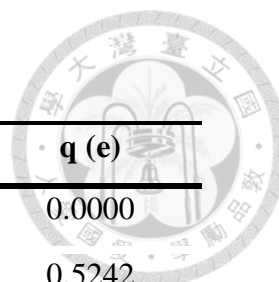
Molucule	Atom	ε(kJl/mol)	σ(Å)	q (e)
H$_2$O	O	0.680862	3.16437	0.0000
	H	0.000000	0.00000	0.5242
	M	0.000000	0.00000	-1.1794
CH4	C	0.276144	3.50000	-0.2400
	H	0.125520	2.50000	0.0600
Mold	wp	0~17.958	0	0

(c)

Molecule	Atom 1	Atom 2	k(kJ/mol/nm^2)	l(Å)
H$_2$O	O	H	-	0.9572
CH$_4$	C	H	2786980.80	1.090
Mold	wp	-	-	1.149

(d)

Molecule	Atom 1	Atom 2	Atom 3	k (kJ/mol/rad^2)	θ(^{o})
H$_2$O	H	O	H	-	104.52
CH$_4$	H	C	H	292.88	109.50
Mold	-	wp	-	-	-

3.5   Hydrogen Bond Identification

We choose Chandler's algorithm [95] to identify the hydrogen bonds between water molecules in this work. Shown as Figure 3.5-1, there are two criteria to form a hydrogen bonding:

(1) The distance between the oxygen atoms from donor and acceptor (d_{Od-Oa}) should

less than 3.5 Å .

(2) The angle of hydrogen from donor-oxygen from donor-oxygen from acceptor should

less than 30 degree.

Donor Oxygen Atom

$d_{Od-Oa} < 3.5Å$

$\theta_{H-Od-Oa} < 30°$

O_a

O_d H

Acceptor Oxygen Atom
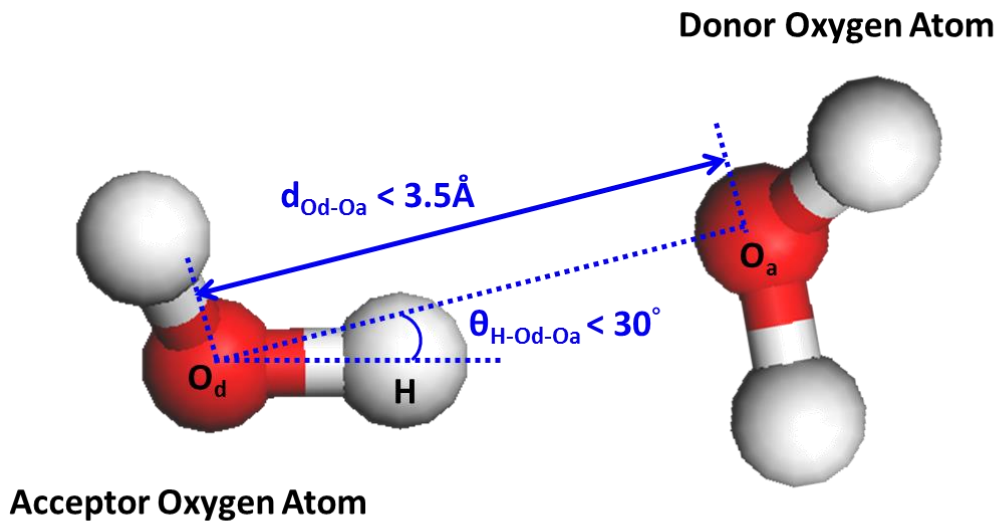
Figure 3.5-1 Two criteria of identification of hydrogen bond.

3.6   Position of Interface Solid/Fluid System Identification

To understand the position of interface between solid phase and fluid phase of two

phase coexistence system, an order parameters has been used.

In this work, no matter the I_h/water or methane hydrate/water system, the composition

of interface is H_2O molecule, so that the order parameter chosen in this case should work

well in distinguishing difference between the fluid-like H_2O and solid-like H_2O. Usually,

the order parameter $\bar{q}_l(i)$, proposed by Lechner and Dellago [96] is used to judge the

solid-like or liquid-like behavior of H_2O,[31, 36, 46] however, in our knowledge, it does

not be used to distinguish the hydrate solid-like. The F4 order parameter [97, 98] is used

to distinguish ice, water and hydrate-like molecules, so we finally decide to use F4 to find

58

out the CMI position, and the steps are listed below:

(1) We divided the system into grids of size around 4 Å ×4 Å × L_n Å , shown like Figure 3.6-1.

(2) Calculating the F4 value of every atom in the system.

(3) Generating neigbour lists, and then recording the index of atoms in every dividing grids

(4) For every grids, recording the information of highest atom , whose F4 value must at the solid-like region, in the normal direction of interface.

(5) Average the high of interface obtained in step 4 along with the $\hat{s}$ direction of interface, so that the data of $h(v_n)$ at every discrete point, v_n, can be obtained.
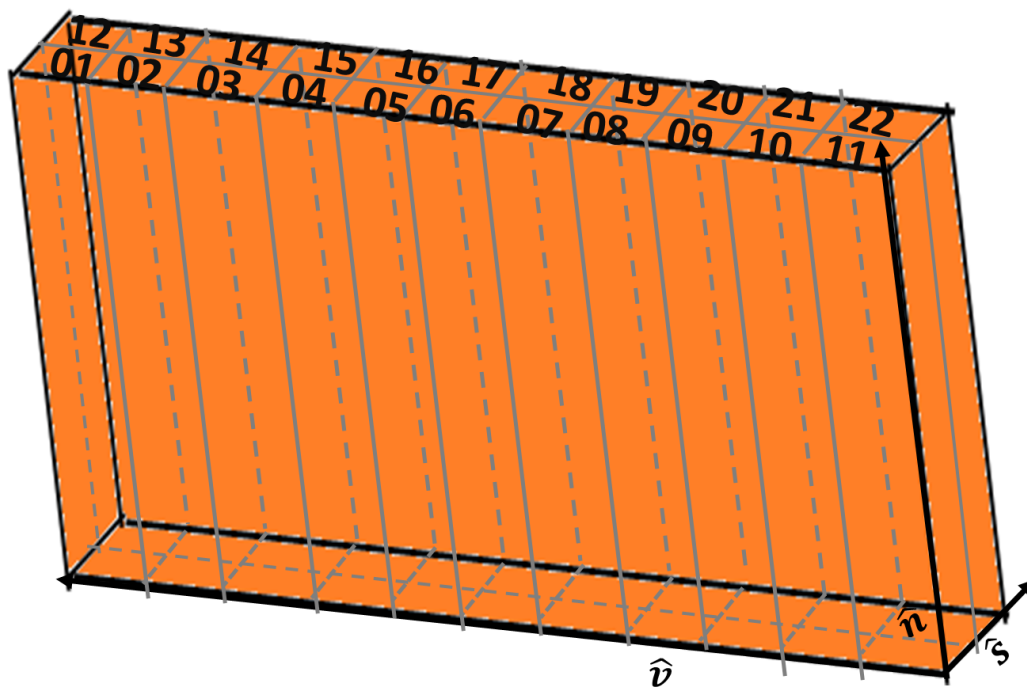
Figure 3.6-1. The schematic of interface position determination.

Chapter 4　Results and Discussion

4.1　Properties of CH$_4$ hydrate and I$_h$

In this part, model A was chosen to run NPT simulation under 1bar and 1.1 MPa, to find out the melting point of I$_h$ and methane hydrate, respectively. After finding out the melting point (see **chapter 4.1.1**), both the diffusivity of fluid-like H$_2$O (see **chapter 4.1.1**) and fusion heat (see **chapter 4.1.1**) are calculated by model B and model C, respectively, under the melting condition that we found.

4.1.1　Bulk Phase Properties of CH$_4$ hydrate and I$_h$

In melting point part, fixing the pressure at 1bar and 11MPa for I$_h$ and CH$_4$ hydrate, respectively. Furthermore, simulating the system for different temperature in order to observe the configuration changing. The potential energy will increase when the solid crystal convert to fluid phase, in contrast, the potential energy will decrease while fluid phase change to solid phase. In other words, if the potential energy of the system is fluctuated at specific value that means the system melts and grows, the temperature of that situation is called melting point. The result of potential energy for different temperature is shown as Figure 4.1.1. Obviously, the melting point for I$_h$ and CH$_4$ hydrate are 270K and 285K, respectively. The results are consist with both other simulation value [47, 99] and experimental data. The diffusivity calculate by equation (21) at melting point of two types of crystal are listed in Table 4.1-1, the result looks reasonable comparing to the experimental data.[100] The Tip4p_ice force-field is known for reproduce of the phase boundary between liquid water and ice, the density of both water and ice, and the heat of fusion. The self-diffusivity does not work as well as other properties, however, usually is around 40%~60% of experimental value.[101]

60
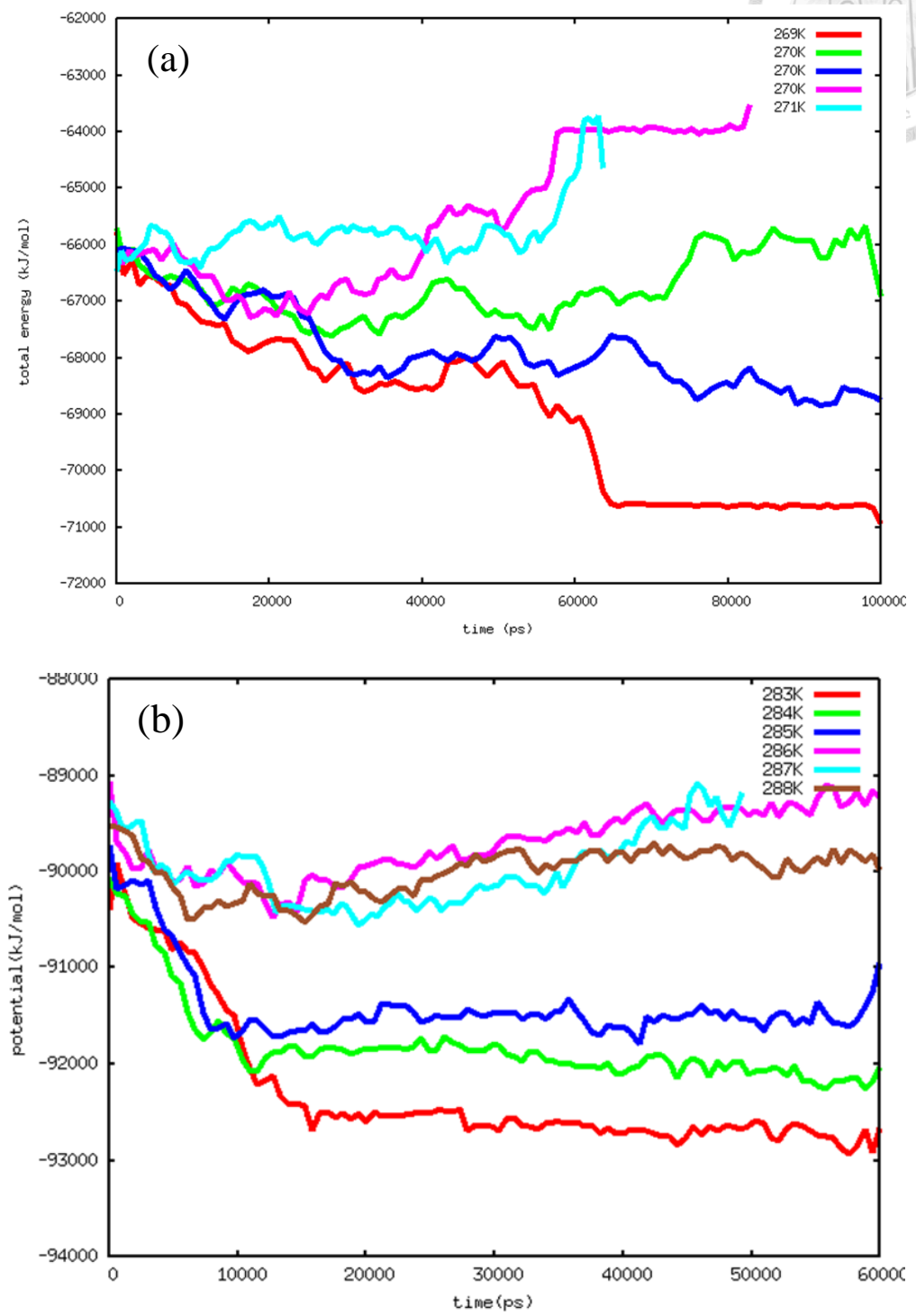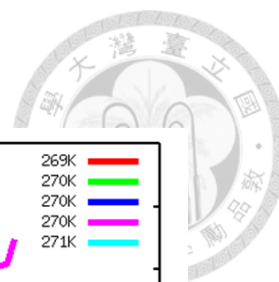
Figure 4.1-1 Potential energy of (a) I_h and (b) sI-CH$_4$ hydrate versus different

temperature.

61

Table 4.1-1 Overall work on detecting the melting point of I_h and sI CH_4 hydrate

	P=1bar	P=11MPa
This work	270K	285K
Ref (simulation)	270K[99, 101]	285K[102]
Ref (experiment)	273.15K[103]	286.5K[104]

Table 4.1-2 Overall work about diffusivity (unit: cm^2/s) of H_2O at various melting-point condition

	270K/1bar	285K
This work	0.3994	0.7932 (11MPa)
Ref (simulation)[101]	0.393	0.743 (1bar)
Ref (experiment)[100]	1.01	1.61 (1bar)

The last property needed to measure so as to calculate the dynamics property of crystal in CFT method is heat of fusion. There are two sets of systems, and each of set is contain two systems – the pure crystal phase and pure fluid mixture phase which is from the totally melting crystal phase. Comparing the equilibrium enthalpy energy difference between these two systems, the heat of fusion (ΔH_m) can be obtained, and listed at Table 4.1.1-2. It is consisted with the other simulation work [47] and also experimental data [103, 105].

Table 4.1-3 Fusion heat of I_h and sI CH_4 hydrate at melting-point condition

Fusion heat (kJ/mol)	270K/1bar (I_h)	285K/11MPa (hydrate)
This work	1.29	7.36

62

Other work	1.29 (*simulation,*[47]) 1.44 (*experiment*,[103])	7.73 (*experiment,*[105])
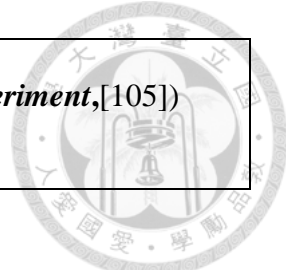
4.2   Interfacial Properties of Methane Hydrate and Water

For the purpose of studying the dynamics and thermodynamics of sI methane hydrate, the main method we used is capillary fluctuation theory.

In CFT, before calculating the fluctuation property of interface, the position of interface of solid/fluid phase should be distinguished. The F4 order parameter is used in discriminating the solid-like or fluid-like of H_2O (the reason was written in **chapter 3.6**). It is found that the performance is not good for F4 in describing atoms in the system without block-average of the coordinate of the atoms. In order to well differentiate solid-like and fluid-like water molecules, average of 40 steps (200ps) is chosen in this work (see **chapter 4.2.1**). However, there is one concern while using the coordinate block-average - ***Does the fluctuation of wave be averaged if using block-average technique or will the block-average generate the artificial CMI?*** We show that the block-average of the coordinate only influences the high-frequency wave (Rayleigh wave) and there is no influence for the low-frequency wave (capillary wave) (see **chapter 4.2.8**). Based on CFT, the interfacial free energy (see **chapter 4.2.2 and 4.2.3**) and the dynamics property (see **chapter 0 and 4.2.7**) are calculated. The results show that the effect of orientation of crystal to interfacial free energy is very small. The relaxation time of methane hydrate is slower than that of I_h by 30 times, and the kinetic coefficient of methane hydrate is 21 times slower than that of I_h.

To validate the results from capillary fluctuation theory (CFT), the mold integration method (MI) is also be used. We validate the capillary fluctuation theory by comparing

the interfacial free energy of CFT to MI because MI calculates the free energy from creating a new interface. The interfacial free energy by MI (see **chapter 4.2.5**) and CFT (see **chapter 4.2.2**) are almost same in the case of I_h, so that the results from CFT is reliable.

4.2.1 The performance of F4 order parameter

There was not any research using F4 order parameter to describe the population distribution of every each oxygen atom of whole system.[97, 98, 106, 107] In order to well distinguish the CMI position of the system, we have to carefully select the optimize value of F4, the result of F4 value of oxygen atoms distribution are shown in Figure 4.2.1(a)~(d). The average value of the F4 distribution that did not do any block-average analysis (Figure 4.2.1-(a)) for I_h, water and sI hydrate is -0.45, 0, and 0.86, respectively. These values correspond to data published, indicating that the distribution profile really reflects to the system.[97, 98, 106, 107] Figure 4.2.1 shows that if the block size below 20 (100 ps), the overlap area for I_h-water and sI hydrate-water is very large and the degree of the overlapping of I_h-water is much large than sI hydrate-water (see Figure 4.2.1-(b)). The reason we do not want to see the overlapping area is because it is hard to use F4 order parameter to differentiate the crystal and fluid-like H_2O at this condition. There will not be a critical F4 value can discriminate the difference of material. Finally, we decide to use the 40 of block size (200 ps) as our baseline of resolution. However, there is a main problem exist – ***Does the fluctuation of wave be averaged if using block-average technique or will the block-average generate the artificial CMI?*** We will discuss this problem in the last part, but we can spoil the answer at this time, the answer is – Block-average only affects the Rayleigh wave of the CMI, the capillary wave will not be affected by that.

64
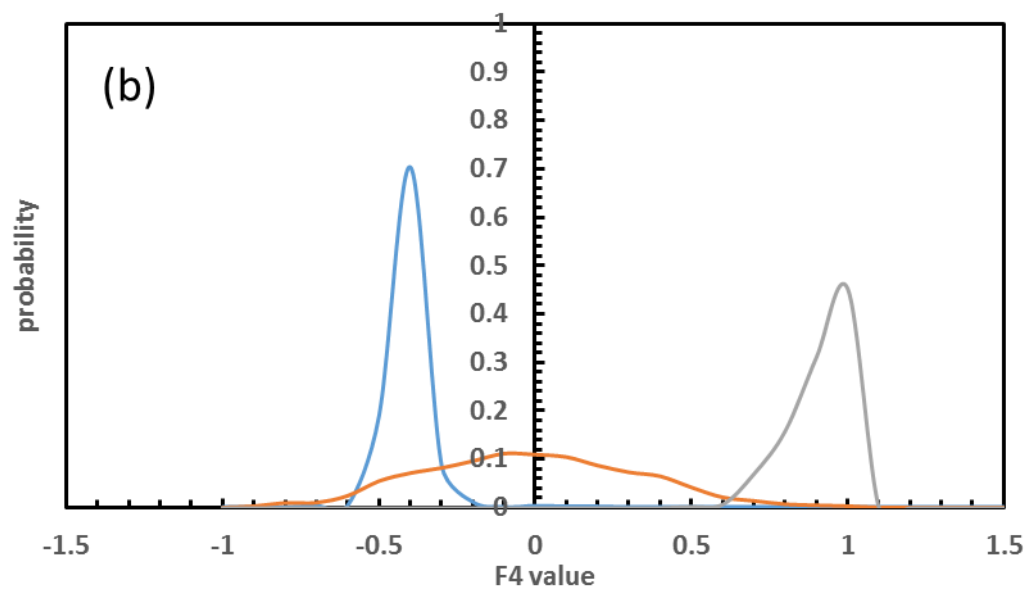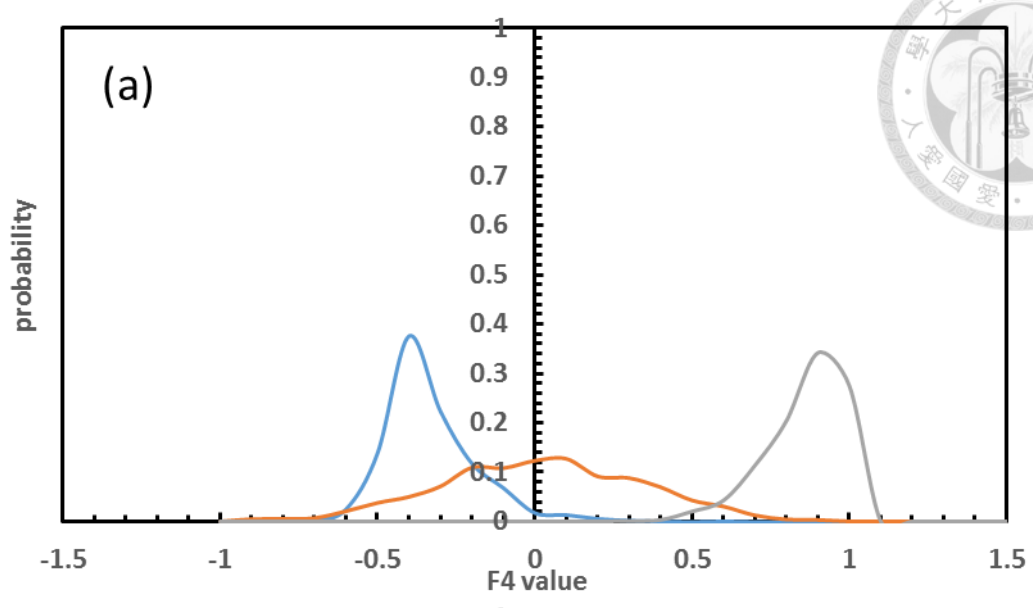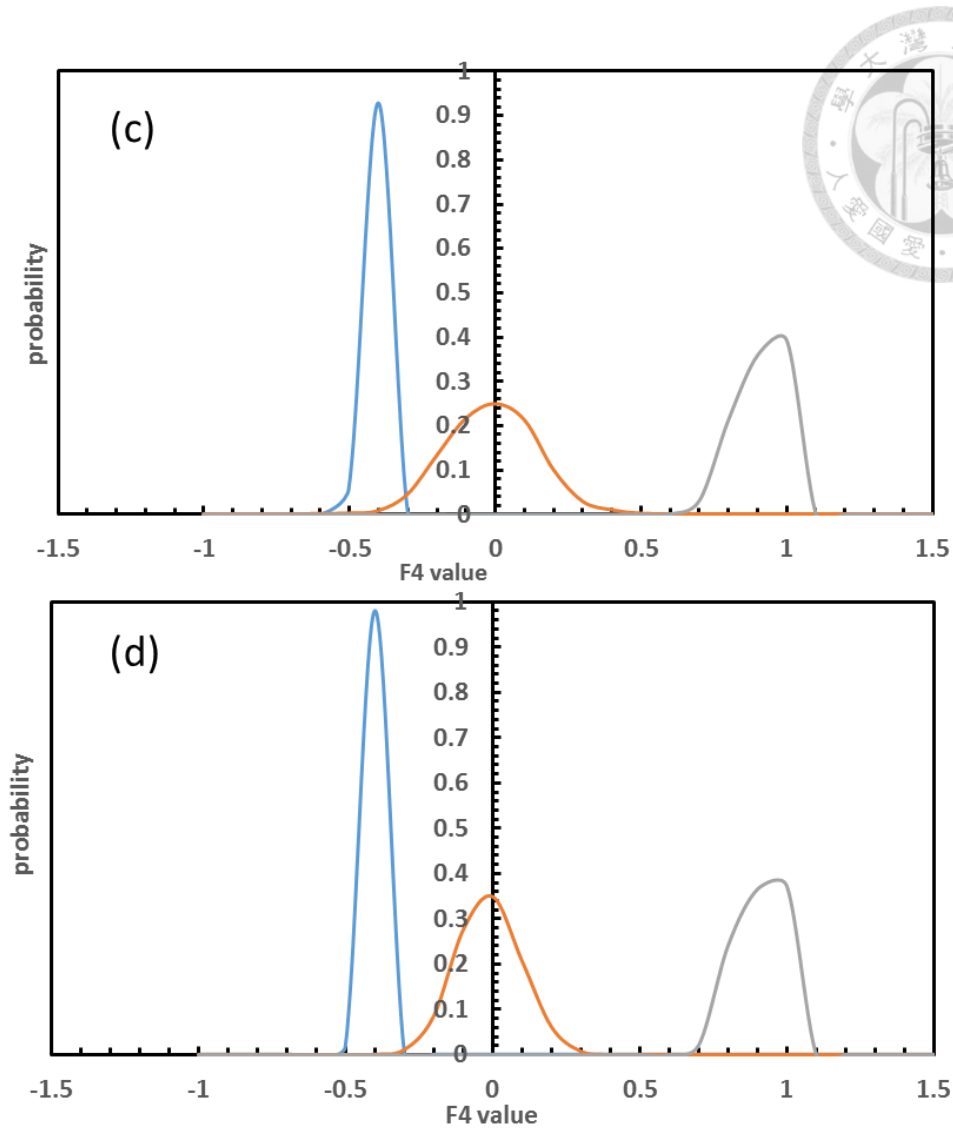
Figure 4.2-1 (a) F4 probability distribution of the system with no block-average. (b) block-average size is set as 4. (c) block-average size is set as 20. (d) block-average size is set as 40. The line colored by azure, orange and silver denote I_h, water, and sI hydrate, respectively.

4.2.2 Thermodynamics properties of CMI system of I_h

We have already shown that using F4 to find out the location of CMI is adequate. Then we input the $h(v_n,t)$ of each orientation system into the Fourier-transform formula, equation (**36**), to obtain the profile of $|h_q|^2$, then we average result to get $<|h_q|^2>$. For a

not smooth interface, by representing $\ln[\ <|h_q|^2>A/(k_BT)\ ]$ versus $\ln(q)$, according to

Equation.(37), we should obtain a straight line with -2 slope and the intercept $-\ln(\tilde{\gamma})$.

The data profiles are shown in Figure 4.2.2 for every orientation also be focused in

E.Sanz *et al*.[36] The blue solid-circle in Figure 4.2.2 correspond to our simulation data

and red solid-line denotes a straight fitting line with -2 slope at low-q region.

Obviously, our simulation data points in low-q region are perfectly described by

equation (37). These data points allow us to calculate the reasonable $\tilde{\gamma}$ from intercept,

and the result of calculation are shown in Table 4.2-1. We only use first 4 points,

determined by observing discrepancy level, in fitting for every orientation.

Once the stiffness is known for a set of different orientations, we can get the

interfacial free energy by solving Equation (38). In order to solve equation (38), the

relationship between θ and normal vector direction $\hat{n}$ should first determined. Since

the point group of I_h is 6/mmm (D_6h), the θ and $\hat{v}$ can be written as an expansion in

terms of Spherical Harmonics [108, 109] :

$$\gamma(\theta,\phi) = \gamma_0[1 + \varepsilon_{20}y_{20}(\theta,\phi) + \varepsilon_{40}y_{40}(\theta,\phi) + \varepsilon_{60}y_{60}(\theta,\phi) + \varepsilon_{66}y_{66}(\theta,\phi)] \tag{27}$$

where γ_0 is the interfacial free energy averaged over all orientations, θ,ϕ are spherical

coordinate defined in Figure 4.2-3 and ε_{lm} are anisotropy parameters.

The spherical $y_{lm}(\theta,\phi)$ represent normalized real harmonics functions taking into

the form shown in Table 4.2-2, and the results of applying the parameters θ,ϕ into the

Table 4.2-2 are listed in Table 4.2-3. Using Table 4.2-2 and Table 4.2-3, the equation

(24) could be solved for interfacial free energy. The expression of expansion of

spherical harmonics for the orientation in Table 4.2-1 are listed in Table 4.2-4. The

results are 3.963, 0.4297, -0.3575, 0, and infinite for $\varepsilon_{20},\varepsilon_{40},\varepsilon_{60},\varepsilon_{66},$ and γ_0, respectively.

Unfortunately, the equations of Table 4.2-4 are not totally linear independent, in other

67
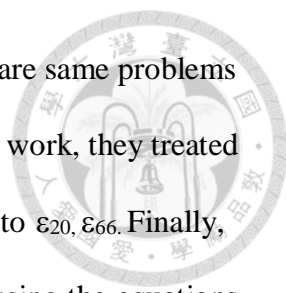
words, the four anisotropy parameter and γ_0 cannot be solved. There are same problems indicated in *ref. [109]* and ***E.Sanz's work***. Therefore, in both of their work, they treated ε_{40} and ε_{60} as zero because these two factors are too small comparing to ε_{20}, ε_{66}. Finally, we can accurately fit the remaining parameters with this strategy by using the equations listed in Table 4.2-4, and $\varepsilon_{20} = -0.027$, $\varepsilon_{66} = -0.0027$ and $\gamma_0 = 29.24(0.91)$ mN/m. The γ_0 value of TIP4P/Ice calculated in this method is in good agreement with both other simulation method and experiment data.[47, 65, 110] Since we also validate this simulation results by other simulation method, all simulation works including this work were sorted out in **section 4.2.5**. The interfacial energy of different orientations have also been calculated shown in Table 4.2-5, and the basal plane is the lowest energy plane, same as the experimental result.[111]
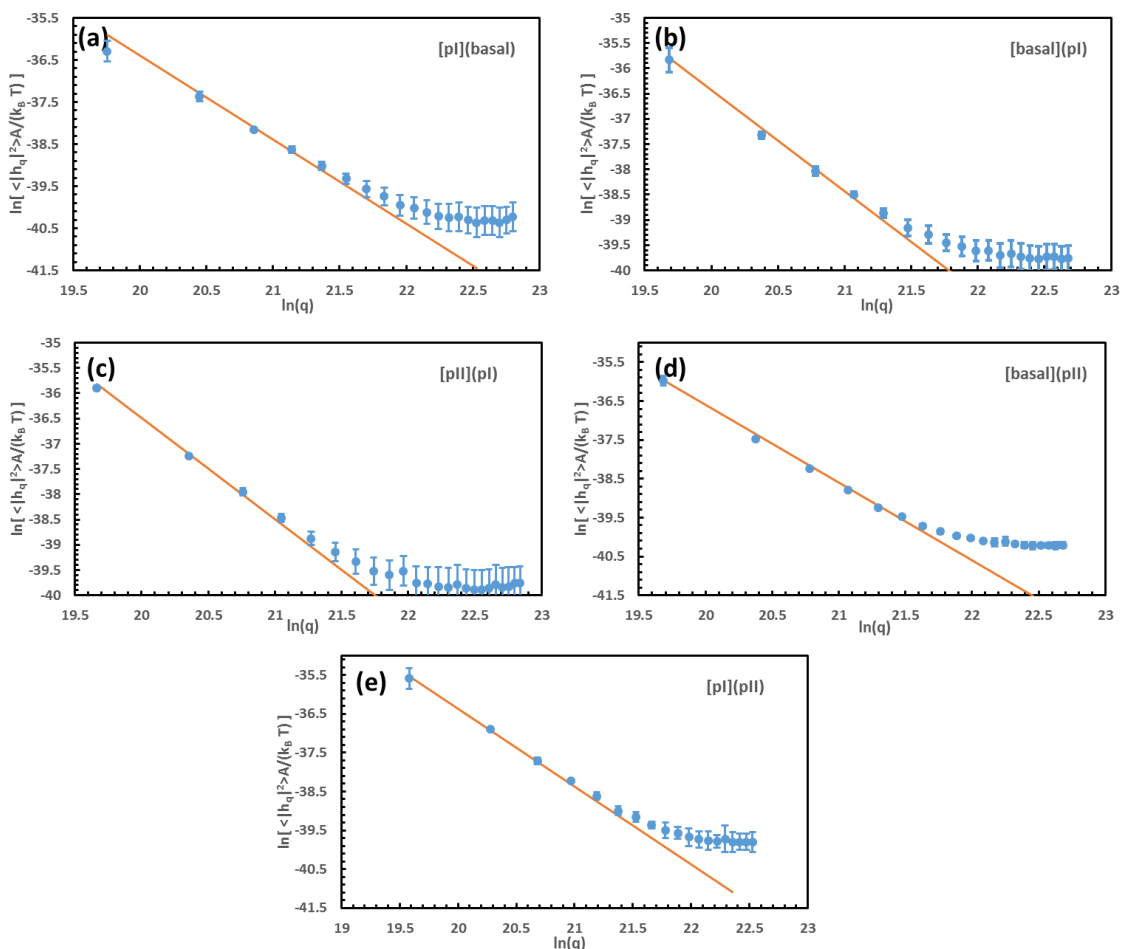
Figure 4.2-2 Plots of $\ln[<|h_q|^2>A/k_BT]$ versus $\ln(q)$ for all I_h/water with different orientations studies. The unit of $<|h_q|^2>A/k_BT$ is used in m^3*N^{-1} and q is given in m^{-1}. The red solid-lines shown in (a) ~ (e) are linear fits with slope -2 at low-q region. The intercept of the fitting is $-\ln(\tilde{\gamma})$, and the unit of $\tilde{\gamma}$ calculating by intercept is N/m.

Table 4.2-1 the interfacial stiffness (unit: mN/m) of each orientation for I_h/Water.

Orientation	This work	E.Sanz (Tip4p/2005)
[pI](basal)	28.10	28.04(0.43)
[basal](pI)	26.57	25.30(2.45)
[pII](pI)	30.19	29.01(0.15)
[basal](pII)	33.37	33.70(1.55)
[pI](pII)	27.13	26.83(0.42)
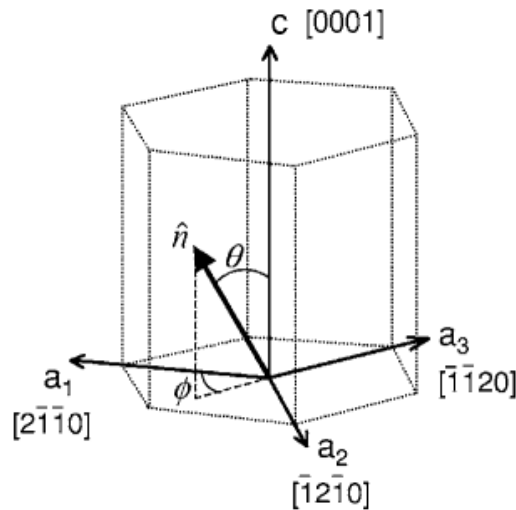
Figure 4.2-3 Coordinate system of I_h, θ, ϕ are spherical coordinate angles used to define the orientation of normal vector direction $(\hat{n})$ to CMI.[109]

Table 4.2-2 The expression of normalized spherical harmonics function [108]

69
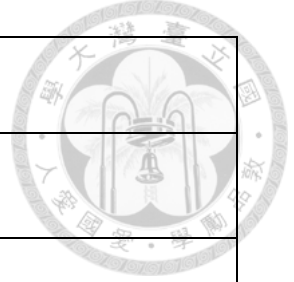
$$y_{20}(\theta,\phi) = \sqrt{\frac{5}{16\pi}}[3\cos^2(\theta) - 1]$$

$$y_{40}(\theta,\phi) = \frac{3}{16} * \sqrt{1/\pi}\,[35\cos^4(\theta) - 30\cos^2(\theta) + 3]$$

$$y_{60}(\theta,\phi) = \frac{1}{32} * \sqrt{\frac{13}{\pi}}\,[231\cos^6(\theta) - 315\cos^4(\theta) + 102\cos^2(\theta) - 5]$$

$$y_{66}(\theta,\phi) = \frac{1}{64}\sqrt{6006/\pi}\,[1 - \cos^2(\theta)]^3\cos(6\phi)$$

Table 4.2-3 Interfacial free energy in terms of normalized spherical harmonics for

different orientations

CMI plane orientation	θ	ϕ	$\gamma(\hat{n})/\gamma_0$
basal	0	0	$1 + \frac{1}{2}\sqrt{\frac{5}{\pi}}\,\varepsilon_{20} + \frac{3}{2}\sqrt{\frac{1}{\pi}}\,\varepsilon_{40} + \frac{1}{2}\sqrt{\frac{13}{\pi}}\,\varepsilon_{60}$
pI	$\pi/2$	$\pi/6$	$1 - \frac{1}{4}\sqrt{\frac{5}{\pi}}\,\varepsilon_{20} + \frac{9}{16}\sqrt{\frac{1}{\pi}}\,\varepsilon_{40} - \frac{5}{32}\sqrt{\frac{13}{\pi}}\,\varepsilon_{60} - \frac{1}{4}\sqrt{\frac{6006}{\pi}}\,\varepsilon_{66}$
pII	$\pi/2$	$\pi/3$	$1 - \frac{1}{4}\sqrt{\frac{5}{\pi}}\,\varepsilon_{20} + \frac{9}{16}\sqrt{\frac{1}{\pi}}\,\varepsilon_{40} - \frac{5}{32}\sqrt{\frac{13}{\pi}}\,\varepsilon_{60} + \frac{1}{4}\sqrt{\frac{6006}{\pi}}\,\varepsilon_{66}$

Table 4.2-4 Stiffness in terms of normalized spherical harmonics for different

orientations

CMI plane orientation	$\tilde{\gamma}(\hat{v},\hat{n})/\gamma_0$
[pI](basal)	$1 - \sqrt{\frac{5}{\pi}}\,\varepsilon_{20} - \frac{27}{2}\sqrt{\frac{1}{\pi}}\,\varepsilon_{40} - 10\sqrt{\frac{13}{\pi}}\,\varepsilon_{60}$
[basal](pI)	$1 + \frac{5}{4}\sqrt{\frac{5}{\pi}}\,\varepsilon_{20} - \frac{171}{16}\sqrt{\frac{1}{\pi}}\,\varepsilon_{40} + \frac{205}{32}\sqrt{\frac{13}{\pi}}\,\varepsilon_{60} + \frac{5}{64}\sqrt{\frac{6006}{\pi}}\,\varepsilon_{66}$
[pII](pI)	$1 - \frac{1}{4}\sqrt{\frac{5}{\pi}}\,\varepsilon_{20} + \frac{9}{16}\sqrt{\frac{1}{\pi}}\,\varepsilon_{40} - \frac{5}{32}\sqrt{\frac{13}{\pi}}\,\varepsilon_{60} + \frac{35}{64}\sqrt{\frac{6006}{\pi}}\,\varepsilon_{66}$
[basal](pII)	$1 + \frac{5}{4}\sqrt{\frac{5}{\pi}}\,\varepsilon_{20} - \frac{171}{16}\sqrt{\frac{1}{\pi}}\,\varepsilon_{40} + \frac{205}{32}\sqrt{\frac{13}{\pi}}\,\varepsilon_{60} - \frac{5}{64}\sqrt{\frac{6006}{\pi}}\,\varepsilon_{66}$
[pI](pII)	$1 - \frac{1}{4}\sqrt{\frac{5}{\pi}}\,\varepsilon_{20} + \frac{9}{16}\sqrt{\frac{1}{\pi}}\,\varepsilon_{40} - \frac{5}{32}\sqrt{\frac{13}{\pi}}\,\varepsilon_{60} - \frac{35}{64}\sqrt{\frac{6006}{\pi}}\,\varepsilon_{66}$

Table 4.2-5 Interfacial free energy of different orientation of I_h

	This work (mJ/m^2)
Basal	28.73(1.00)
pI	29.55(0.88)
pII	29.44(0.86)
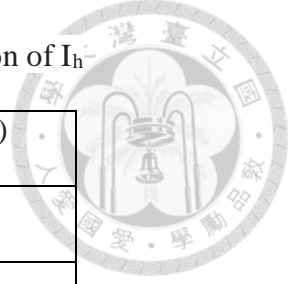
4.2.3 Thermodynamics properties of CMI system of CH_4 hydrate

Same as the part of evaluating the thermodynamics properties by representing $\ln[\ <|h_q|^2>A/(k_BT)\ ]$ versus $\ln(q)$, according to Equation.(37). However, the question that needs to be addressed is how many independent stiffness measurements are needed to calculate γ of CMI of sI hydrate crystal? The experiment data using diffraction data shows that sI hydrate crystalline is a cubic crystal and belongs to P_m3_n space group.[112] The $\widehat{x_1}, \widehat{x_2}$ and $\widehat{x_3}$ are the unit vectors parallel to the [100], [010], and [001] directions, respectively, and by n_i (i∈ [1,3]) the components of the interface normal direction, $\hat{n}$, in the (x_1 , x_2 , x_3) coordinate system. The $\hat{x}$ is parallel to the wave propagation direction, and $\hat{y}$ is normal to CMI plane.

The spherical harmonics for cubic symmetry can be written in:[113]

$$\frac{\gamma(\hat{n})}{\gamma_0} = \ 1 - 3\varepsilon + 4\varepsilon\sum_{n=1}^{3} n_i^4 + \delta\left(\sum_{n=1}^{3} n_i^6 + 30n_1^2n_2^2n_3^2\right) \tag{41}$$

Since the interface fluctuates in the (x,y) plane and θ is the angle between $\hat{n}$ and $\hat{y}$, the stiffness for a given choice of slab orientation ($\hat{x}$, $\hat{y}$) is simply obtained by substituting the expression $n_i = (\cos(\theta)\hat{y} + \sin(\theta)\hat{x})\dot{}\hat{x}_i$ into equation (41).

This information tells us that there are at least three different orientation of CMI systems needed if we want to get interfacial free energy from interfacial stiffness property.

According to above reason, we simulate the several CMI systems and the result are

shown in Figure 4.2-4. The blue solid-circle in Figure 4.2-4 corresponds to our simulation data and orange solid-line represents a straight fitting line with -2 slope at low-q region. The CMI simulation data points are located on -2 slope straight line. However, the data point of lowest frequency in all orientation is divergent from -2 slope, the reason is that the statistical data points is not sufficient, and it will discuss in **section 4.2.7**. According to the above reason, the first data point of all orientation is abolished in fitting, also the 2nd to 6th data point is used to fitting stiffness (the reason will discuss in **section 4.2.7**)**.**
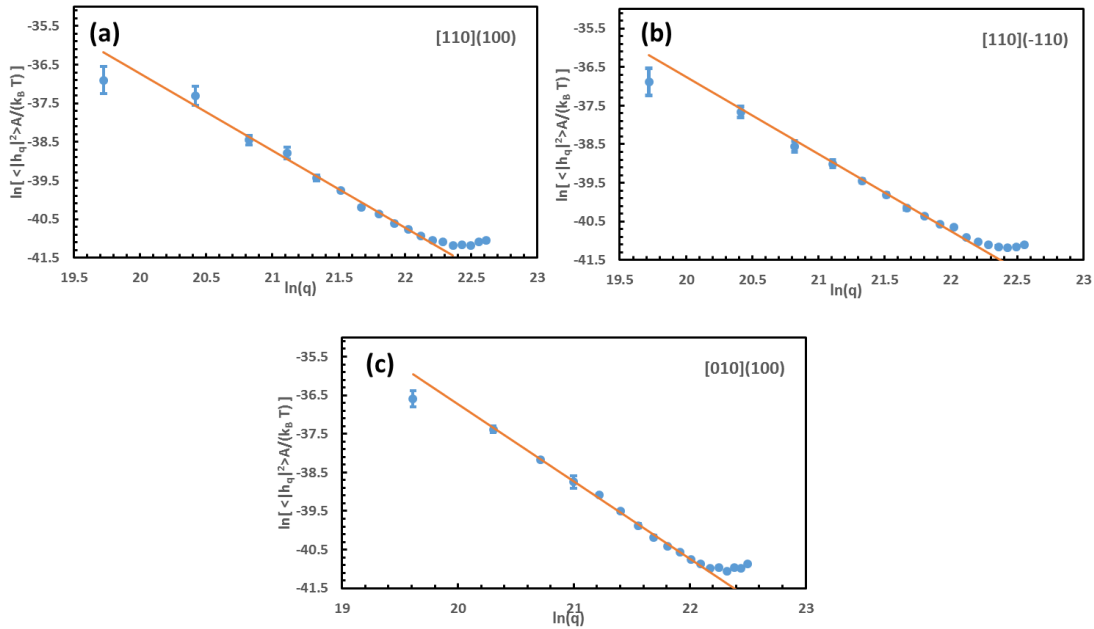
Figure 4.2-4 Plots of $\ln[\ <|h_q|^2>A/k_BT\ ]$ versus $\ln(q)$ for all sI hydrate/water with different orientations studies. The unit of $<|h_q|^2>A/k_BT$ is used in m^3*N^{-1} and q is given in m^{-1}. The orange solid-lines shown in (a) ~ (c) are linear fits with slope -2 at low-q region. The intercept of the fitting is $-\ln(\tilde{\gamma})$.

Once the stiffness is known, we can solve the interfacial free energy by equation (41). The parameters are recorded in Table 4.2-6. The result of parameters are $\gamma_0 = 34.60(0.6)$ mJ/m^2, $\varepsilon = -0.0089$ and $\delta = -0.005$. The interfacial free energy is in good

72

agreement for both other simulation data and experiment data [67-69], listed in Table 4.2-7. The anisotropy parameter is very small, and it indicates that the effect of orientation for sI hydrate crystal to interfacial free energy can be neglected.
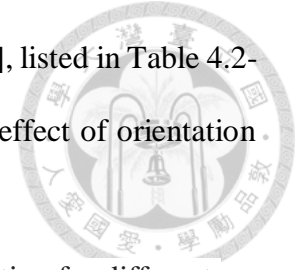
Table 4.2-6 The stiffness and expression of cubic harmonics function for different

orientations

Orientation	$(\gamma+\gamma'')/\gamma_0$	Stiffness (mJ./m^2)
[110](100)	$1 + 9\varepsilon + 10\delta$	36.22(0.58)
[110]($\bar{1}$10)	$1 + 15\varepsilon + (25/4)\delta$	34.05 (0.36)
[010](100)	$1 - 15\varepsilon - 5\delta$	35.69(0.87)

Table 4.2-7 Comparison of interfacial free energy of methane hydrate and water with

experiment

Source	Type	Condition	Method	γ (mJ./m^2)
L.C. Jacobson[68]	**simulation**	500bar/270K	G-T equation	36(2)
B.C. Knott [69]	**simulation**	900bar/273K	CNT	31
R. Anderson[67]	**experiment**	270K~286K	G-T melting condition	32(3)
T. Uchido[67]	**experiment**	270K~286K	G-T melting condition	34(6)
This work	**simulation**	110bar/285K	CFT	34.60(0.6)

4.2.4 Thermodynamics properties of CMI system with SDS of CH₄ hydrate

In this part, the detail of orientation and cubic harmonics are as same as those of
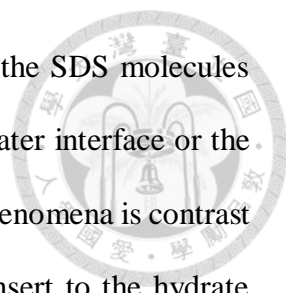
section 4.2.3. However, in this case, the problems we faced is that the SDS molecules could not adsorb on the hydrate interface then leaving to the CH_4/water interface or the hydrophobic tails of SDS aggregate together forming micelle. This phenomena is contrast to other simulation works which shows that the hydrophobic tail insert to the hydrate surface, the adsorption free energy is lowest and the most stable.[114, 115] Even we have tried that removing the CH_4 layer, the problems still exist. If the SDS could not adhere on the interface when the system approach to the equilibrium state, the results of CFT method are meaningless.

But even so, we still did several independent run of this kind of system though existing there problems, the results are shown as Figure 4.2-5. Apparently, the data point in the low frequency region is divergent between every independent run, this is reasonable because the SDS was detaching from the CMI during the simulation and the detaching-sequence of this process is random. Also, we have tried to add the potential field at the C12, which is the last carbon atom far from the hydrophilic head group of SDS, fixing it at the position of hydrate surface, however, this manner causes the interface behavior be artificial, so it does not observe the CFT (see red points in Figure 4.2-5).

It is a coincidence though several points of *run 1* in the middle frequency region are located at the -2 slope, and the result of fitting stiffness reduce from 35.69 to 29.7 mN/m, According to CNT, the nucleation rate accelerates almost 100 times.
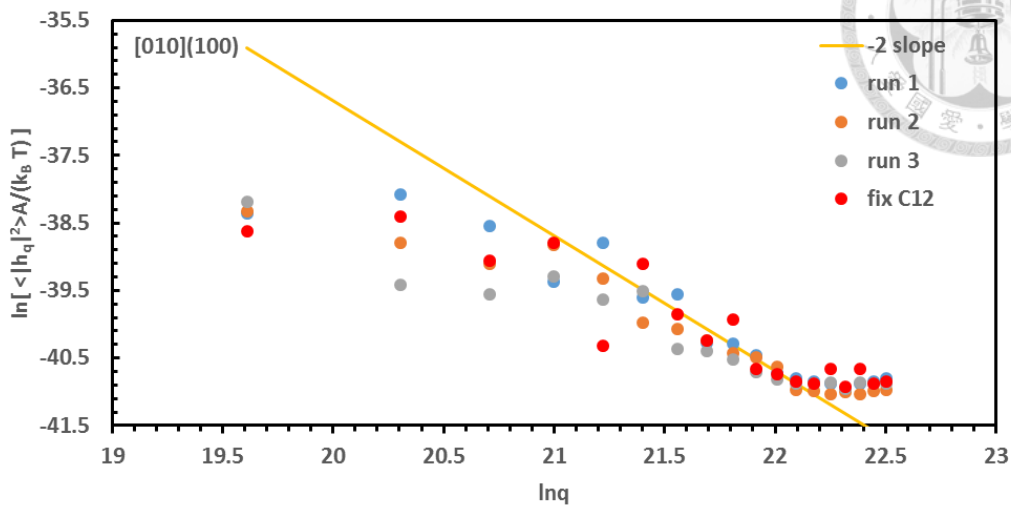
Figure 4.2-5 ln[$<|h_q|^2>A/k_BT$] versus ln(q) for [010](100) sI hydrate/water case. The -2 slope is fitted by the data point at the middle frequency region of run 1.

4.2.5   The validation by Mold Integration method

The first step is to find out the optimal well radius, r_w^o (that for the right γ is obtained). This can be done by performing several simulations and judging the behavior of the system. If $r_W \leq r_w^o$, an ice slab will grow in all trajectories with no induction period indicated that there is no free energy barrier for the formation of the crystal. If $r_w > r_w^o$, a barrier must be overcome, which is reflected in some trajectories with having an induction time before the slab grows or even no slab formation at all if r_w is too large. To know the growth of a crystal slab occurring or not, we monitor the F4 for whole system, the F4 value of the system are -0.45 and 0, if the crystal slab forming or not, respectively, shown as Figure 4.2.5. We find $r_w^o = 0.98$ Å, which corresponds with the outcome studied by **_J.R.Espinosa et.al_**.[47] So we directly used the results of **_ref.[47]_** for the r_w^o of other different plane, as shown Table 4.2-8.

75
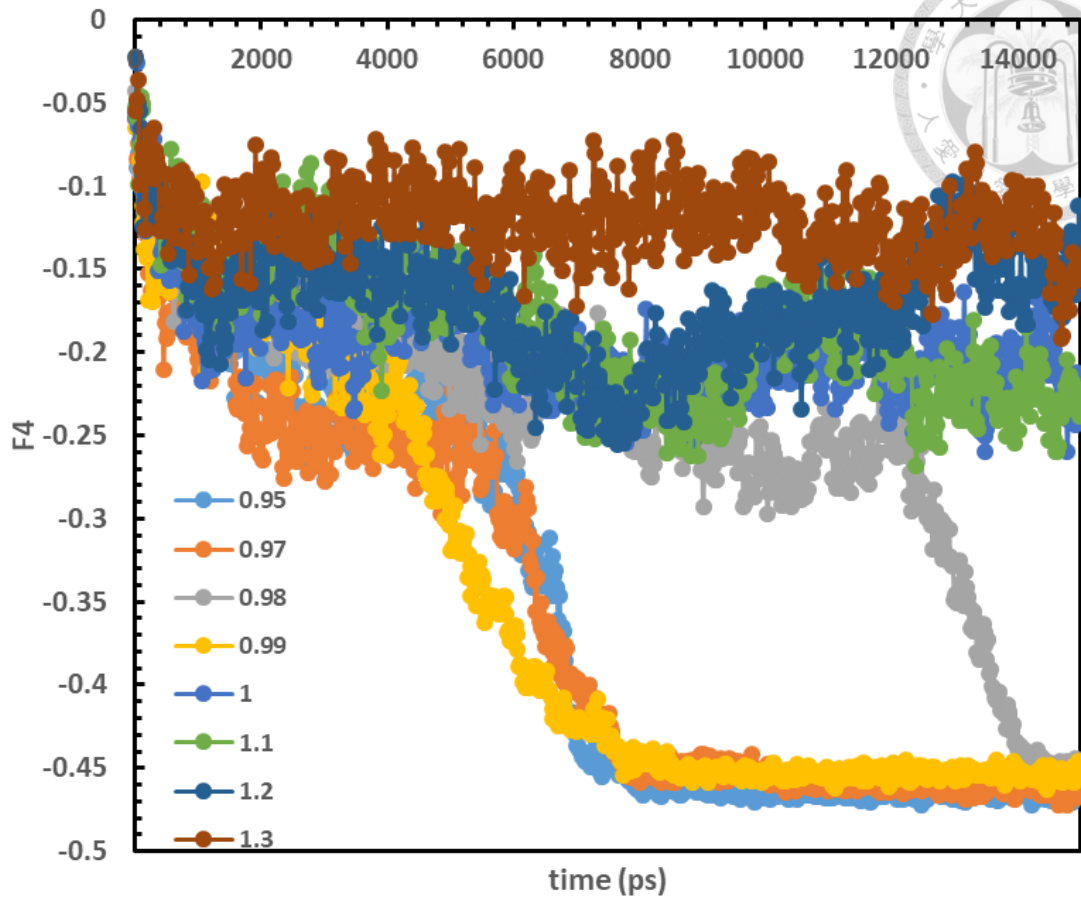
Figure 4.2-6 The F4 of the system at different r_w conditions.

Table 4.2-8 Summarize the r_w^o and interfacial energy of basal, pI, and pII plane.

Orientation	r_w^o	γ (mJ./m^2)
Basal	0.83	26.9
pI	0.77	31.3
pII	0.98	30.6

Table 4.2-9 Comparing the interfacial energy of basal, pI, and pII plane by MI and CFT

in this work.

Orientation	r_w^o	γ (mJ./m^2)
Basal	26.9	28.9

76

pI	31.3	29.3
pII	30.6	29.1

Once we get the r_w^o, the interfacial free energy could be obtained by calculating the γ for $r_w > r_w^o$ condition using thermodynamics integration, and then extrapolating the γ to the r_w^o. However, there is one problem needed to consider – ***What is the proper ε_m in thermodynamics integration?*** In the thermodynamics integration, the free energy difference is calculated from state A to state B. In this work, the state A indicates there is no interaction between the mold and oxygen atom, and state B symbolize the specific orientation plane of I_h fully be generated, however, but we do not know what is the suitable non-bonding interaction should be measured between the mold and oxygen. If the interaction force is too small, the ice layer will not be created. According to the above reasons, we adjust a set of different parameter of interaction force and detect the relationship between that and the numbers of filled mold in order to find out the suitable ε of final state B, shown as Figure 4.2.6. Obviously, when the ε is larger than $6k_BT$, the filled number of wells do not change, it indicates that the magnitude of ε required to well describe the ice layer created in the liquid phase is at least $6k_BT$, in this work, we chose $\varepsilon = 8k_BT$ as final state. Based on the equation (34), the interfacial free energy can be determined from integrating the area under the line of Figure 4.2-7. We also show that the result of the relationship between ε and the numbers of filled mold will not be influenced by initial configuration, in other words, the numbers of H_2O molecules fill in molds initially is not relevant to the results. The results of γ at $r_w > r_w^o$ are shown in Figure 4.2-8, and γ at r_w^o for pI, pII and basal are 26.9, 31.3 and 30.6 mJ/m^2, respectively. These results are in the agreement of other simulation works, listed systematically of overall

77

results including other works in Table 4.2-9Table 4.2-10. Besides, existing little influence of the number of mold to results is verified, shown as Figure 4.2-9. The result is in our expectation, because the perturbation of system is more obvious on fewer sample points system than numerous one, however, there is only 3% error between small and larger system. Finally, according to results of γ from MI consisting with that frim CFT shows that results of CFT is reliable.
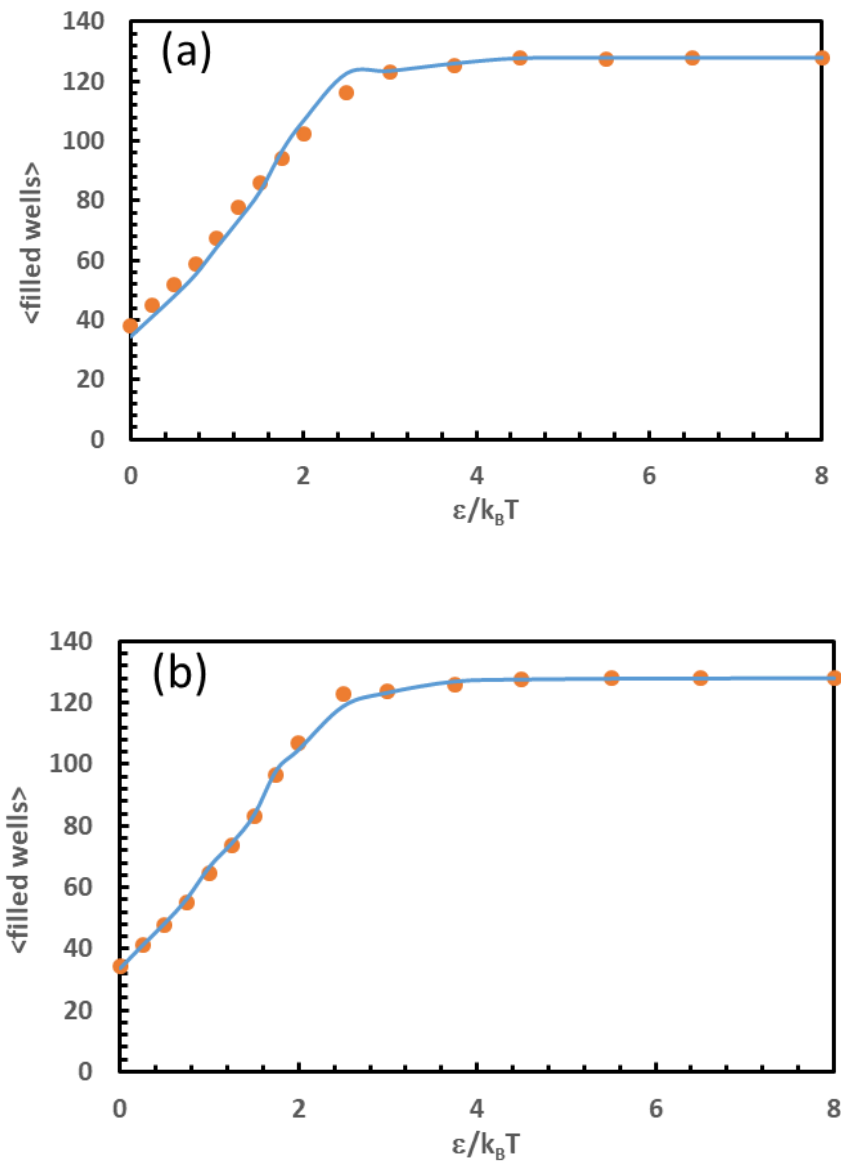
Figure 4.2-7 Average number of filled wells versus well depth (ϵ/k_BT) for the pII plane of the TIP4P/Ice model. The radius of the mold wells is (a) r_w=1.30 Å and (b) 1.25 Å.

78

Orange circles (blue line) correspond to simulations starting from an equilibrated configuration with the mold switched on (off).
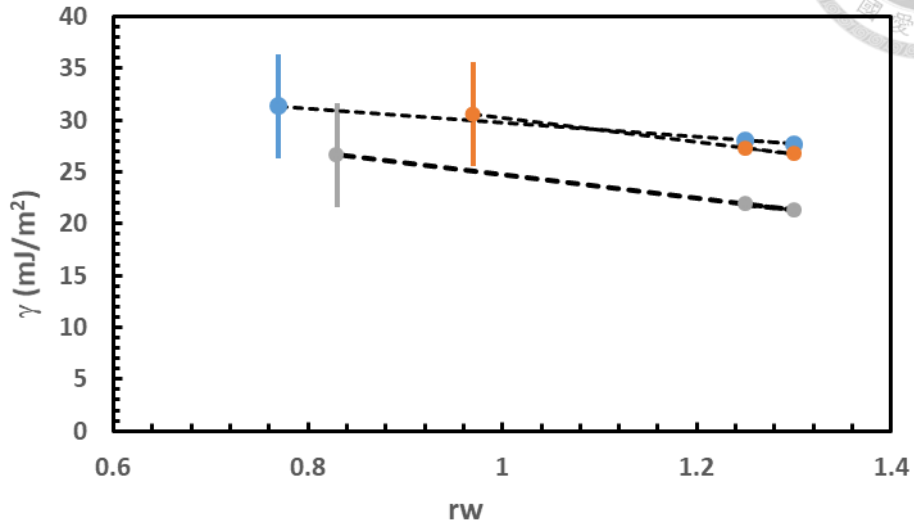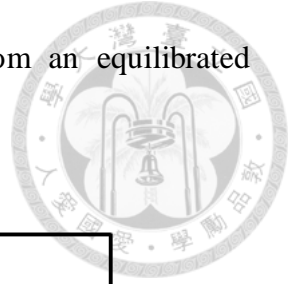
Figure 4.2-8 Filled symbols: interfacial free energy for different values of the well radius and crystal orientations of I_h. Orange, blue, and gray denote pII, pI and basal, respectively. Dash lines indicate the linear fits to filled symbols. Points with vertical line indicate r^o_w.
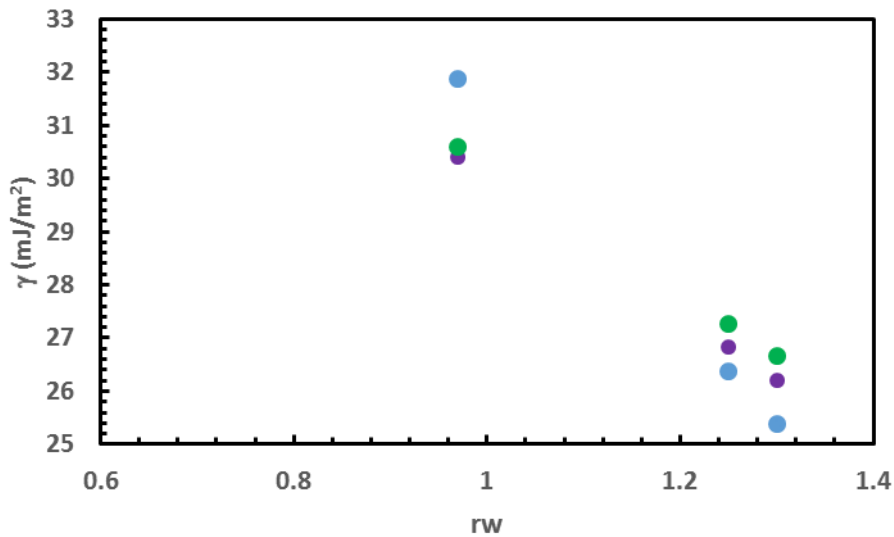
Figure 4.2-9 Filled symbols: interfacial free energy for different values of the well radius of pII plane of I_h. Blue, purple, and green denote 32, 64 and 128 numbers of mold, respectively.

79
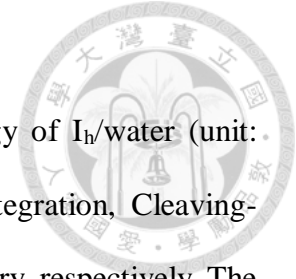
Table 4.2-10 Overall simulation work about interfacial free energy of I_h/water (unit: mN/m). MI, CMS, CNT, and CFT are corresponded to Mold-integration, Cleaving-methods, Classical-nucleation theory, and Capillary-fluctuation theory, respectively. The value of interfacial tension of MI, CMs, CNT, and CFT is obtained from ref. [31, 43, 45, 47], respectively. The * mark denotes the result verified by this work.

Method	MI			CMs			CNT	CFT		
Orientation	Basal	pI	pII	Basal	pI	pII	–	Basal	pI	pII
Tip4P/Ice	26.9*、27.2	31.3*、31.6	30.6*、30.7				28.7	28.7*	29.6*	29.4*
Tip4P/2005	27.2	29.5	30.0				28.7	27	28	28
Tip4P	25.5	28.2	28.0	24.5	27.6	27.5				
mW	34.5	35.1	35.2							

4.2.6 Dynamics properties of CMI system of I_h

For each CMI orientation system of I_h described in Table 4.2-1, we evaluate $f_q(t)$ by equation (42) for several values of q. Some of these autocorrelation functions are shown in Figure 4.2-10. The correlation functions decay from 1 to 0 as the wave-modes relax, and the relaxation for a given interface is the slower of the smaller wave frequency q. The result of $f_q(t)$ is consistent with the previous simulation studies of CMI, where the decay of correlation functions were found to be pure monotonous exponential decay.[31, 34, 35] Furthermore, the wave can be categorized to Rayleigh wave and Kelvin wave, the latter is high frequency behavior caused by elastic movement, not same as capillary wave. Therefore, the described dynamics functions should not be a single exponential function but a double exponential:[31]

80

$$f_q(t) = Ae^{\frac{-t}{\tau_{ds}}} + (1-A)e^{\frac{-t}{\tau_{df}}} \tag{42}$$

where A is fraction of contribution for the slow relaxation behavior , τ_{ds} is a characteristic time for slow relaxation process (low frequency behavior) and τ_{df} is a characteristic time for fast relaxation process (high frequency behavior), and these three are the fitting parameters.

The parameter $A \in [0:1]$ in equation (27) quantifies the weight of slow relaxation behavior of CMI wave. When A is close to 1, the decay of $f_q(t)$ is dominated by the slow relaxation process. However, there are infinite sets of solution for equation (42) if there is not constrain. In order to obtain the parameters with reasonable physical meaning, we assume:

$$f_q(t) \approx A\,exp\left(-\frac{t}{\tau_{ds}}\right) \tag{43}$$

According to the relaxation time of slow process usually is an order larger that fast process, we make an assumption that the fast relaxation process can be neglected when getting the initial guess for slow relaxation characteristic time parameter, so that we take the derivative of equation (43):

$$\frac{d\ln(f_q(t))}{dt} = -\frac{1}{\tau_{ds}} \tag{44}$$

Using the equation (44), we plotted the dln(f_q(t*))/dt* versus t*, shown in Figure 4.2.10, then τ_{ds} is obtained.
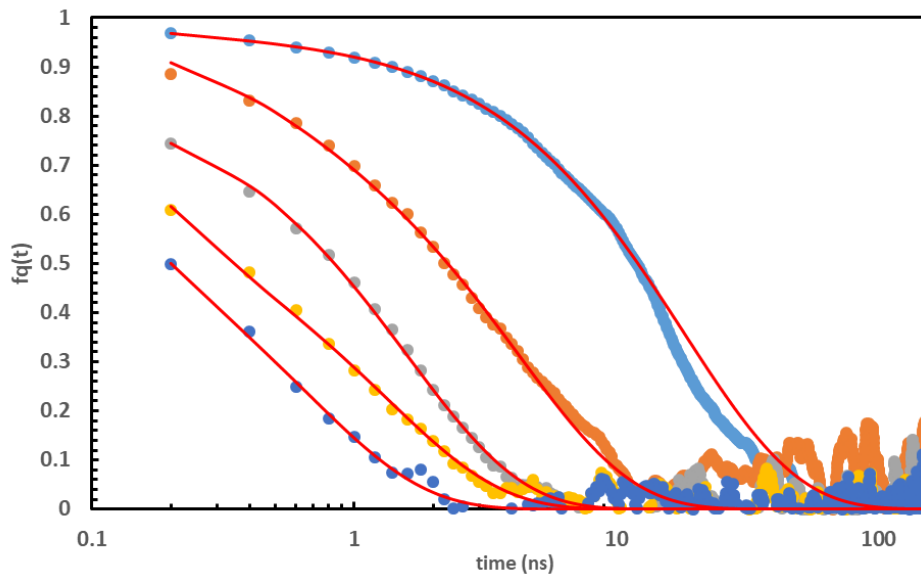
Figure 4.2-10   Autocorrelation functions for the water [pII](pI). The color of azure, orange, silver, yellow, and blue denote k=1, k=2, k=3, k=4, and k=5, respectively. Red line represents fitting result (for mode less than 5).
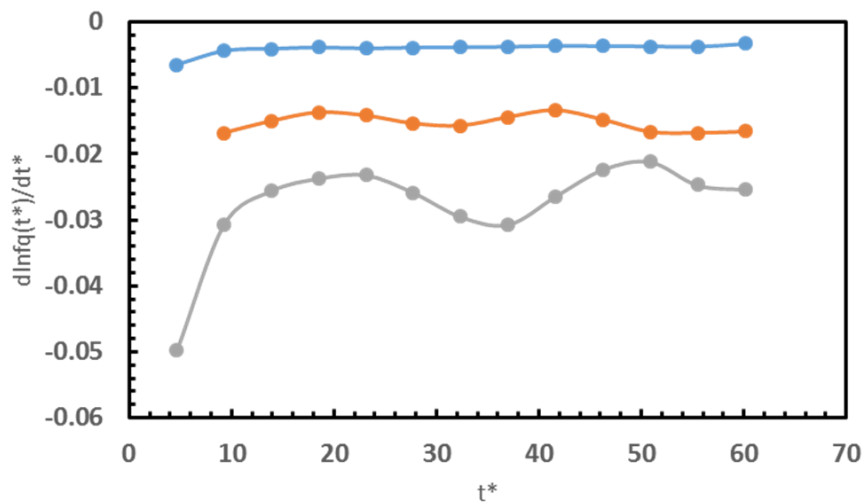
Figure 4.2-11 Representation of dln (f_q(t)/dt vs t for I_h [pI](pII). The color of azure, orange, and silver denote k=1, k=2, and k=3, respectively.

In Figure 4.2-12, we plot A as a function of dimensionless q for several orientations

82

of water/ice system. In this orientation, A is close to 1 for small frequency mode and decrease as q increase. This phenomenon corresponds to the Rayleigh and Kelvin wave theory, when q is larger, the wave behavior is more dominated by fast relaxation process.
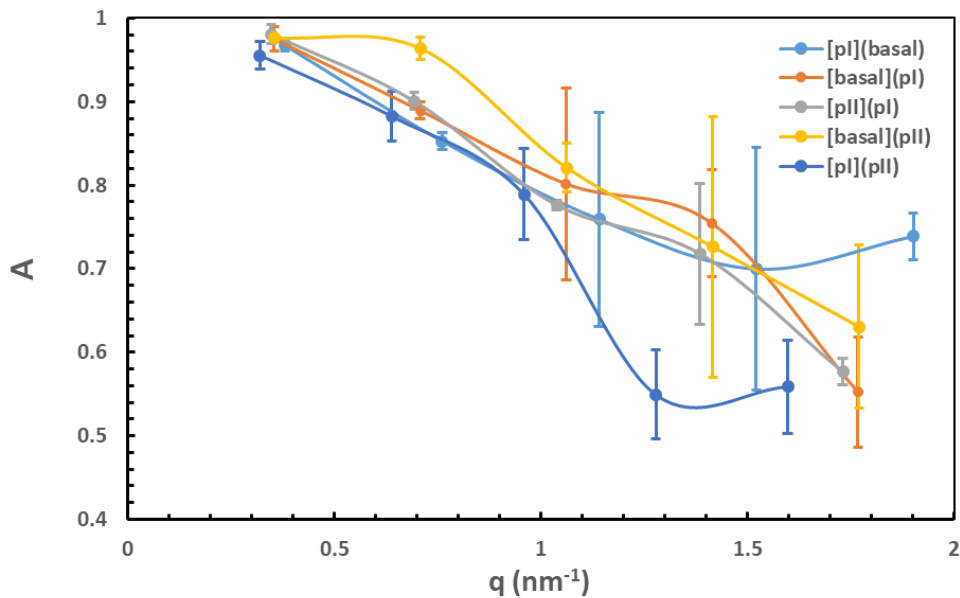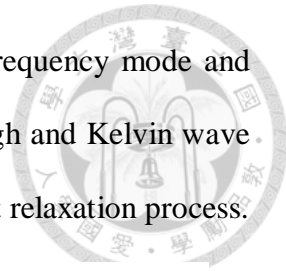
Figure 4.2-12 Prefactor for the double exponential fit as function of q for water [pII](pI).

We elucidate the nature for both slow and fast relaxation behavior by discussing the relationship between τ_{ds} and q, τ_{df} and q, respectively, and the results are shown in Figure 4.2.12. In Figure 4.2.12-(a), we plot $\tau_{ds}*$ against dimensionless q. We plot a dash line with -2 slope in the double logarithmic coordinate. Obviously, the relation between $\tau_{ds}*$, from double exponential fitting this work, and q is perfectly consisted with Karma's theory. However, the fast relaxation process shown in Figure 4.2-13-(b), there is no any evident relation between $\tau_{df}*$ and q, and it appoint out using capillary wave theory to describe the high frequency behavior is not reasonable though the theory can accurately analyze the low frequency behavior (CW). Not only the Figure 4.2-13-(b) but also Figure 4.2-2 can support our conclusion, at high frequency region, the data point is divergent from the -2
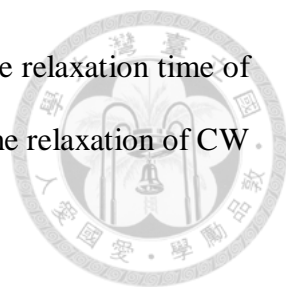
slope. Comparing the relaxation time of Figure 4.2-13 (a) and (b), the relaxation time of slow process is two order less than fast process, and this prove that the relaxation of CW is much longer than Rayleigh wave again.
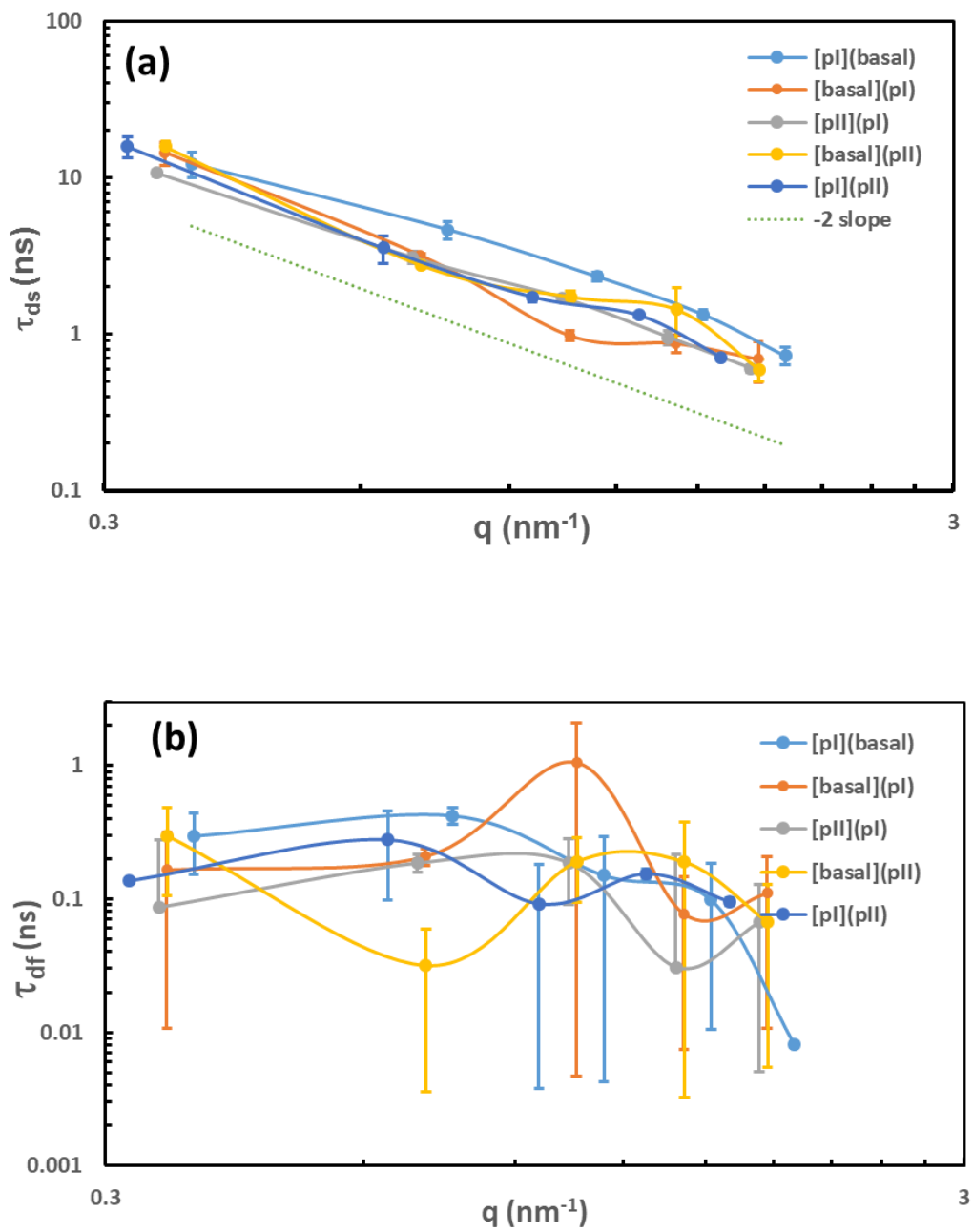
Figure 4.2-13   (a) Dimensionless characteristic time for the slow relaxation process, τ_{ds}, versus the dimensionless wave-vector q/σ^{-1} in a double logarithmic scale for all

84
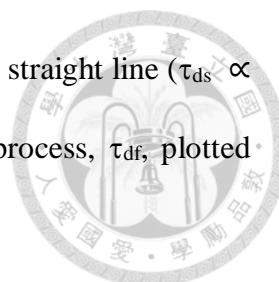
orientation interface. The orange dash line symbolizes -2 slope linear straight line ($\tau_{ds} \propto q^{-2}$) (b) Dimensionless characteristic time for the fast relaxation process, τ_{df}, plotted against the dimensionless wave-vector q/σ^{-1}.

We calculated the kinetic coefficient by plotting the $\tau_{ds} * q^2$ versus against with q, shown as Figure 4.2-14, and comparing to the results to other simulation work and experiment [116, 117], shown as Figure 4.2-15 and also listed the value of μ of different orientation in Table 4.2-11.
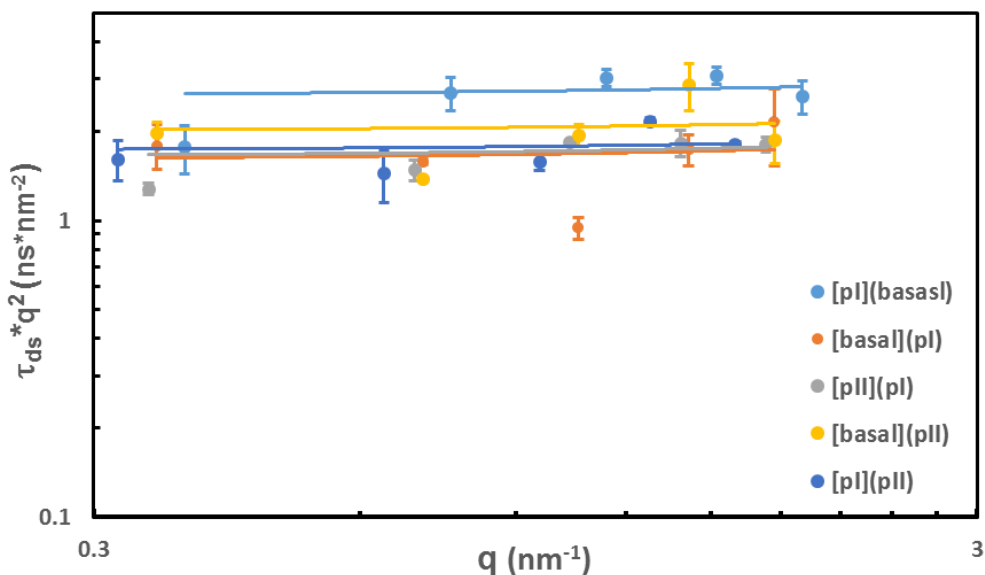
Figure 4.2-14 $\tau_{ds} * q^2$ in logarithmic scale versus against with q. Azure, orange, silver, yellow, and blue denote [pI](basal), [basal](pI), [pII[](pI), [basal](pII) and [pI](pII), respectively.

85
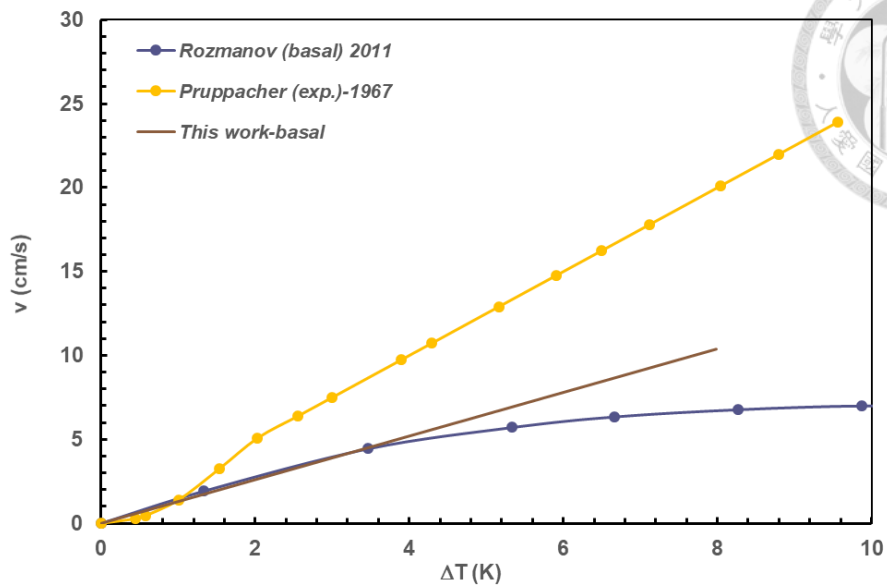
Figure 4.2-15 Crystal growth rate as a function of degree of subcooling (ΔT). Yellow

line denotes experimental result by Pruppacher[116]. Blue line indicates simulation

result by Rozmanov[117]. Brown line is the result by this work.

Table 4.2-11 Kinetic coefficient for different orientations of I_h/water

Model	Orientation	μ (cm/sK)
	Basal	1.30
TIP4P_ICE	pI	2.40
	pII	1.87

It is distinct that at the region that ΔT approaches to zero is more accurate than larger

ΔT region, the reason we presume that is the kinetic coefficient from CFT calculated

under the phase-equilibrium condition, in other words, the driving force is closed to zero,

so that the kinetic coefficient by CFT actually is under the condition that ΔT to zero, and

then extrapolated to other ΔT region. According to other simulation and experiment work,

86
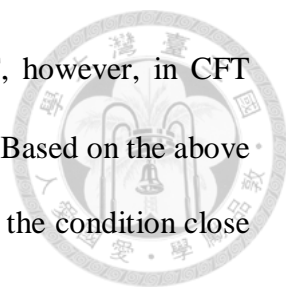
the kinetic coefficient of I_h/water varied from every region of ΔT, however, in CFT method, we assumed that it is not dependent with ΔT but a constant. Based on the above reason, the CFT is more suitable to measure the kinetic coefficient at the condition close to phase-equilibrium state.

4.2.7 Dynamics properties of CMI system of CH₄ hydrate

For each CMI orientation system of sI hydrate described in Table 3.1-4, we evaluate $f_q(t)$ by equation (42) for several values of q. Some of these autocorrelation functions are shown in Figure 4.2-16(a)-(c). The correlation functions decay from 1 to 0 as the wave-modes relax, the relaxation time of lower wave frequency q for a given interface is much slower than that of I_h system.

87
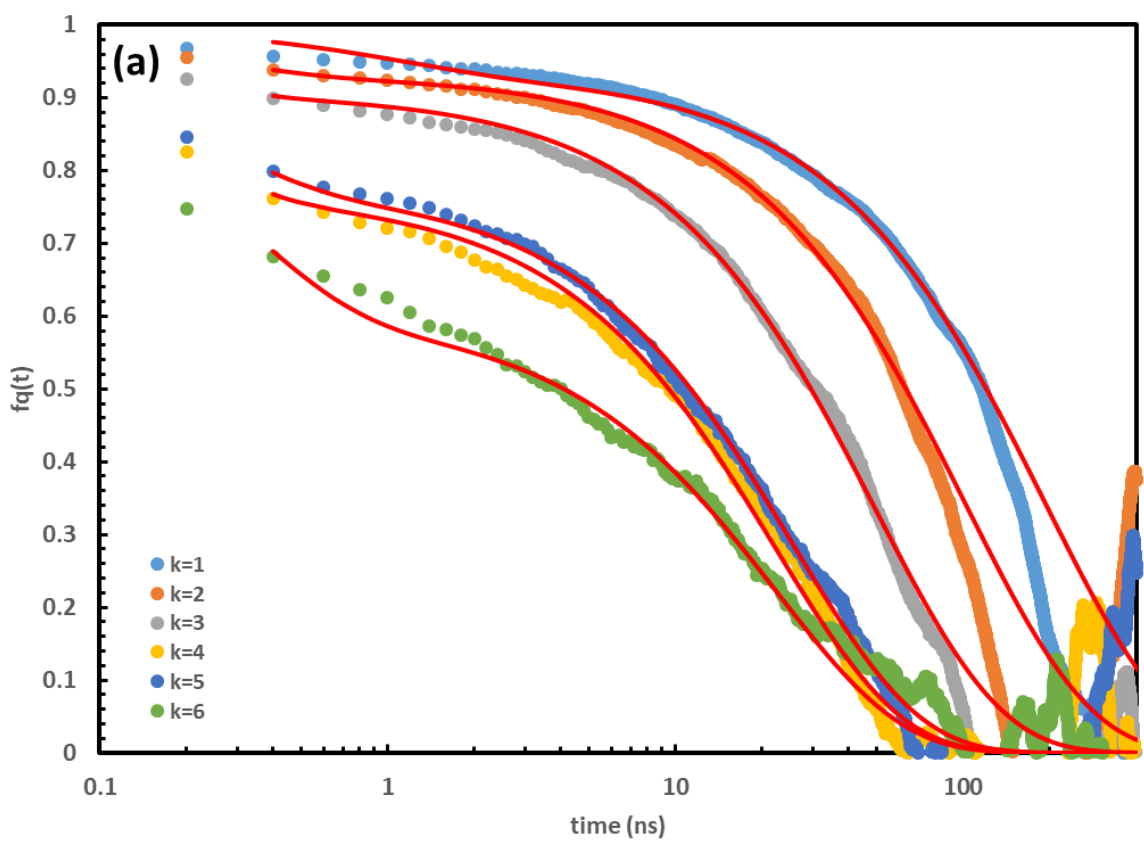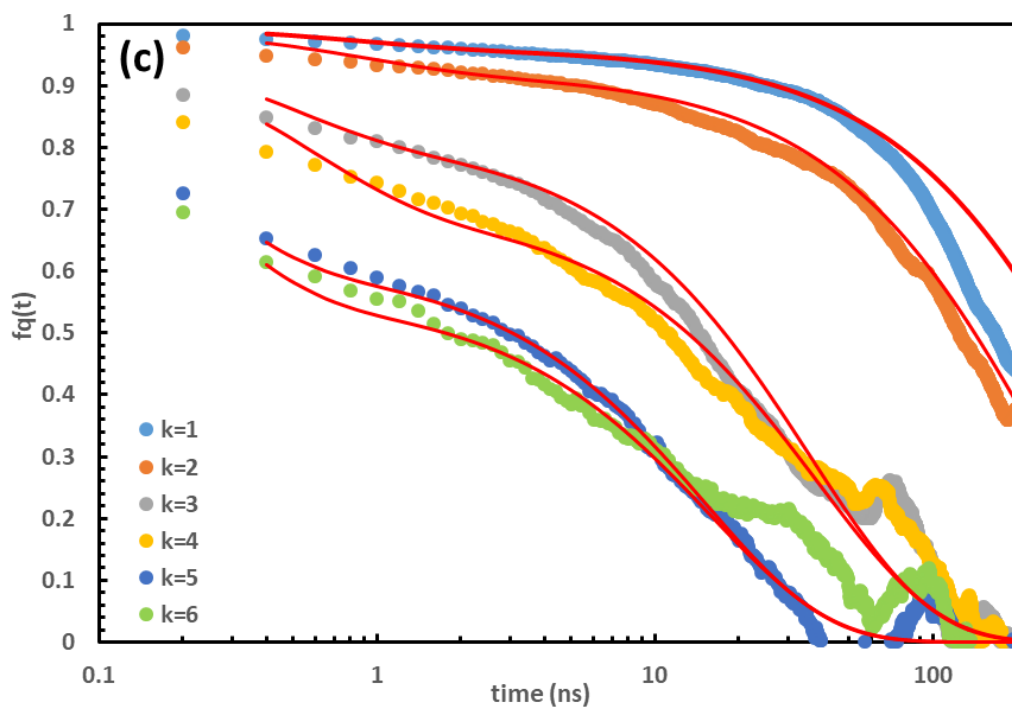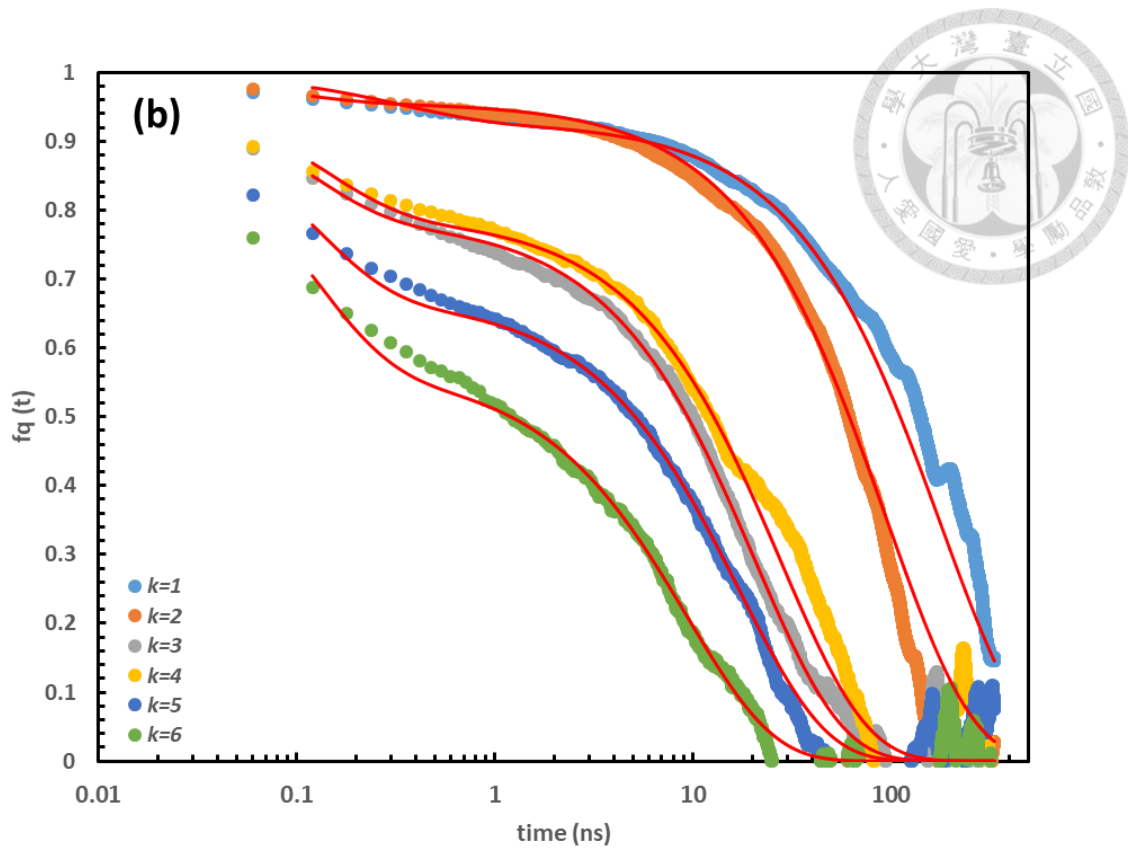
Figure 4.2-16 (a) Autocorrelation functions for the sI hydrate [010](100). (b) [110]($\bar{1}$10)

(c) [110](100). Red lines represent fitting results (for mode less than 6).

88

In Figure 4.2-17, we plot A as a function of dimensionless q for all hydrate system investigated. A is close to 1 for small frequency mode and decrease as q increase. This phenomenon also corresponds to the Rayleigh and Kelvin wave theory, when q is larger, the wave behavior is more dominated by fast relaxation process. Hence, the data point corresponding to A being above 0.5 is used in fitting -2 slope in Figure 4.2-4, which is the reason why we used 2nd to 6th data points in fitting (abandoning 1st data point will explain in latter part).
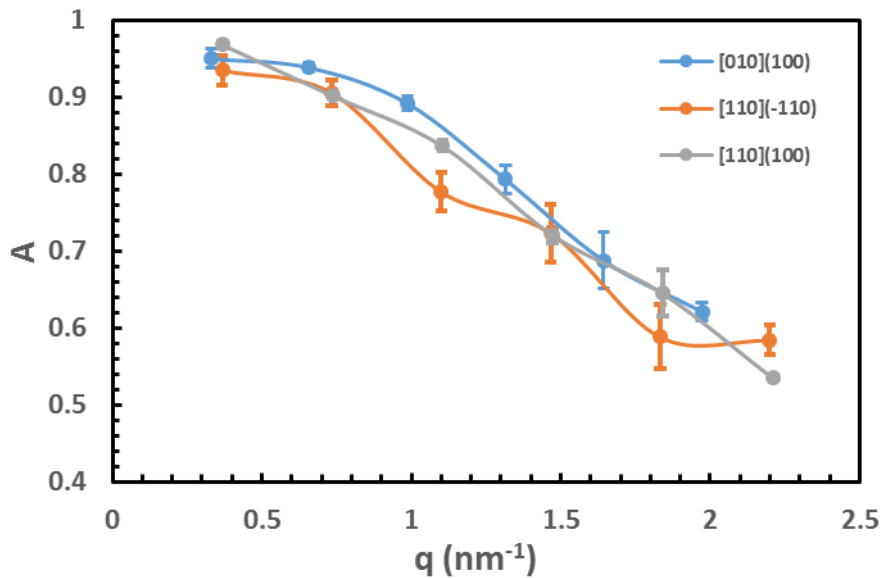
Figure 4.2-17 Prefactor for the double exponential fit as function of q for sI hydrate. The line color by azure, silver and orange is represented by [010](100), [110](-110) and [110](100), respectively

We elucidate the nature for both slow and fast relaxation behavior by discussing the relationship between τ_{ds} and q, τ_{df} and q, respectively, and the results are shown in Figure 4.2-18. In Figure 4.2-18-(a), we plot the $\tau_{ds}*$ against dimensionless q. We plot a dash line with -2 slope in the double logarithmic coordinate. Obviously, the relation between $\tau_{ds}*$,

89

from double exponential fitting this work, and q is perfectly consisted with Karma's theory except the 1st mode. This phenomenon is attributed to the number of statistic data point. In Figure 4.2-16, the lowest frequent mode needs a lot of simulation time to fully relax, in other words, it is hard for us to get enough statistic number, as same as other frequency mode, of sampling the lowest-q mode wave in limit time, and the above reason caused the 1st data point of both Figure 4.2-5 and Figure 4.2-18 deviate from expecting value.

In contrast to slow relaxation process, the fast relaxation process shown in Figure 4.2-18-(b). There is no any evident relation between τ_{df}^* and q, and this is same as the observation in CMI of I_h. Comparing the relaxation time of Figure 4.2-18 (a) and (b), the relaxation time of slow process is two to three order less than fast process. Furthermore, the relaxation time of slow process of hydrate is almost 30 times longer than I_h..
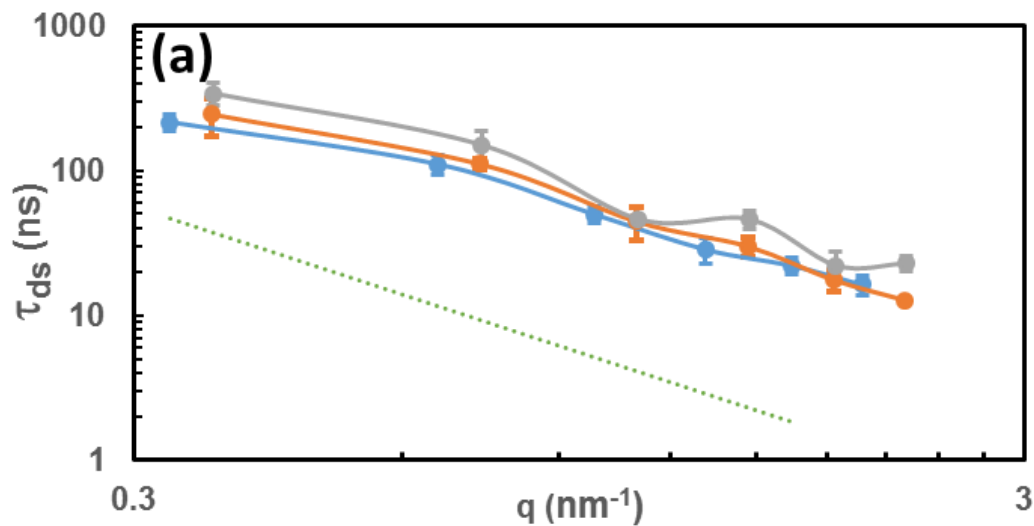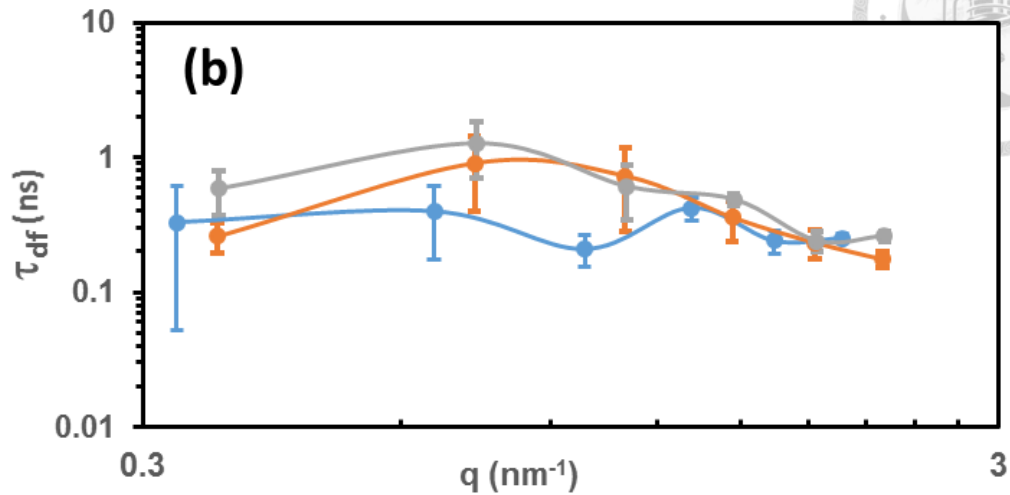
Figure 4.2-18 (a) Dimensionless characteristic time for the slow relaxation process, τ_{ds}, versus the dimensionless wave-vector q/σ^{-1} in a double logarithmic scale for all orientation interface. The green dash line symbolizes -2 slope linear straight line ($\tau_{ds} \propto q^{-2}$) (b) Dimensionless characteristic time for the fast relaxation process, τ_{df}, plotted against the dimensionless wave-vector q/σ^{-1}. The line color are shown in azure, silver and orange symbolized as [010](100), [110](-110) and [110](100), respectively.

Again, we calculated the kinetic coefficient by plotting the $\tau_{ds} * q^2$ versus against with q, shown as Figure 4.2-19, and comparing to the results to other simulation work and experiment [102, 118], shown as Figure 4.2-20 and also listed the value of μ of different orientation in Table 4.2-12.
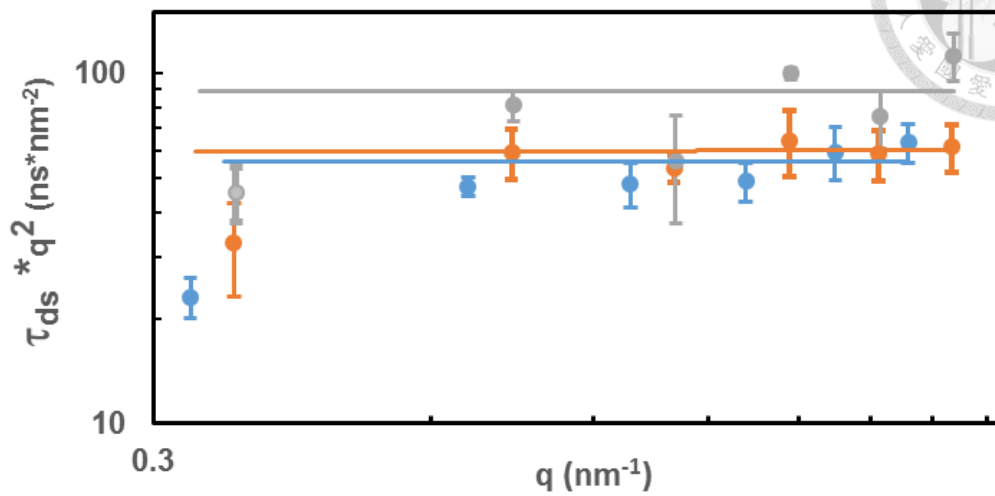
Figure 4.2-19 $\tau_{ds}* q^2$ in logarithmic scale versus against with q. Azure, orange, and

silver denote [010](100), [110]($\bar{1}$10), and [110](100), respectively.
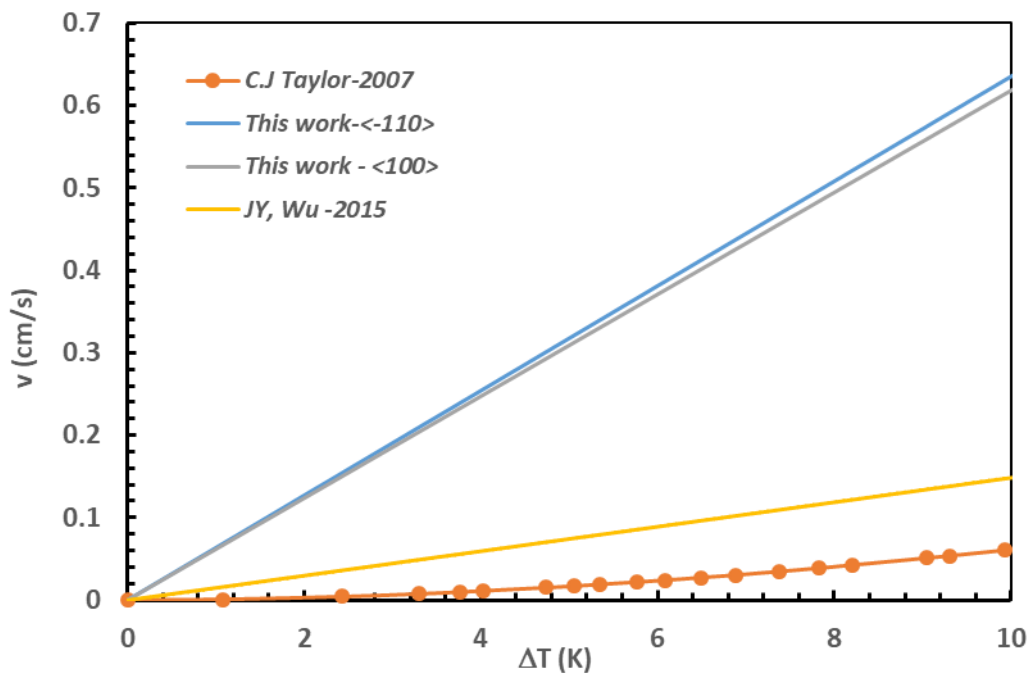
Figure 4.2-20 Crystal growth rate as a function of degree of subcooling (ΔT). Orange line

denotes experimental result by C.J.Taylor[118]. Yellow line indicates simulation result

by JY,Wu [102]. Azure and silver line are the results done by this work.

92

Table 4.2-12 Kinetic coefficient for different orientations of sI CH_4-hydrate/water

Model	Orientation	μ (cm/sK)
TIP4P_ICE+ OPLS_AA	<100>	0.059
	<$\bar{1}$10>	0.060

The results of kinetic coefficient by CFT from this work are much larger than both other simulation work and experiment data, almost 20~30 times. It is not consist with presumption deduced from **section 0**. Even in the region that degree of subcooling approaches to zero, the discrepancy of the magnitude of μ by CFT is still obvious. However, the data in the simulation work of JY, Wu *et al.*, shown in Figure 4.2-20 were conducted at the 20K of ΔT. In the other words, the yellow curve in Figure 4.2-20 is extrapolated from ΔT at 20K. The kinetic coefficient is a function of temperature, so the growth rate of yellow curve is not accurate at the region of ΔT approaching to zero, so we mimicked both the same method and system in JY, Wu *et al.* work at several ΔT to re-plot the growth-rate curve.

The results of growth-rate of several cases working at different degree of subcooling by the method used in JY, Wu *et al* is shown as Figure 4.2-21. Apparently, the growth-rate of CFT method works better than other methods in the region of ΔT close to zero. But there is still a lot of difference between CFT method and experiment result. We suspected that it must something happened at the hydrate/water interface of CMI system caused the kinetic coefficient by CFT is larger than experiment so much. In order to verify our assumption, the equilibrium of interfacial methane molecules system and methane concentration distribution from interface to bulk phase were considered.

93
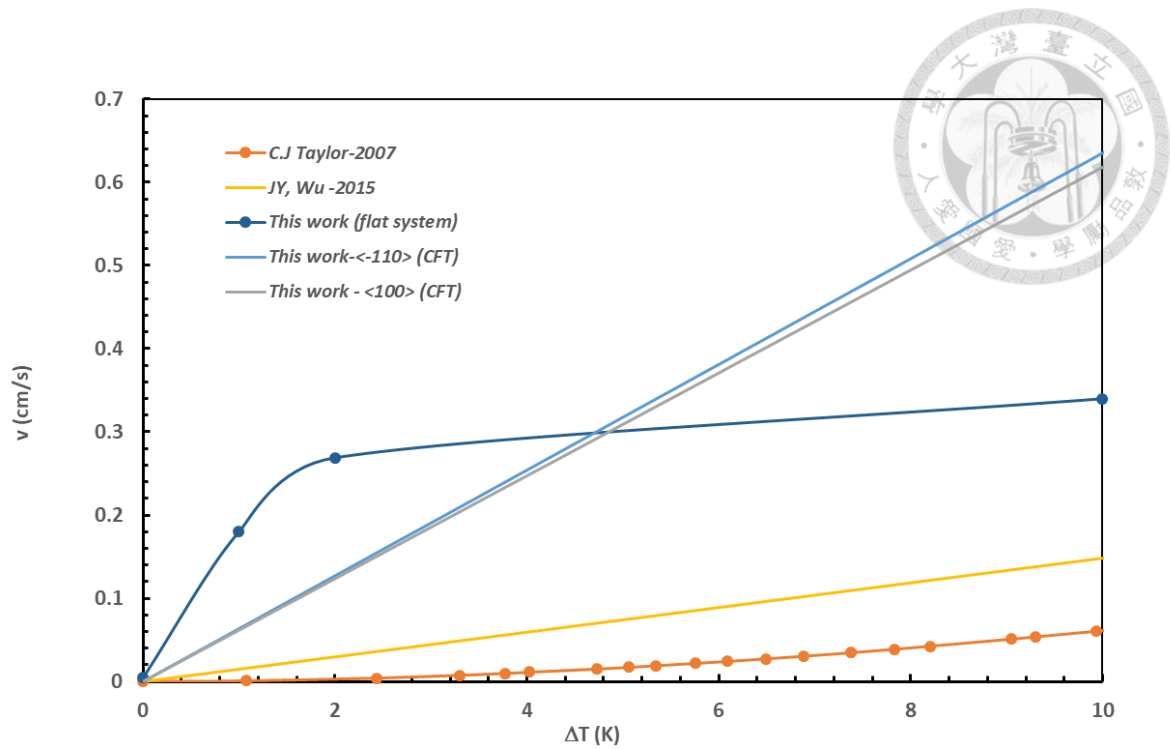
Figure 4.2-21 Crystal growth rate as a function of degree of subcooling (ΔT). The heavy-blue curve is plotted by the method as same as JY,Wu [102] but in multiple temperature condition.

Observe the exchange of methane in gas phase with that at interface so as to determine if the system reached to equilibrium, the progress of motion of methane atoms is shown as Figure 4.2-22. It is obvious that exchange behavior occurs. Therefore, the concern of equilibrium is not a factor of causing μ by CFT to be larger than other manners.
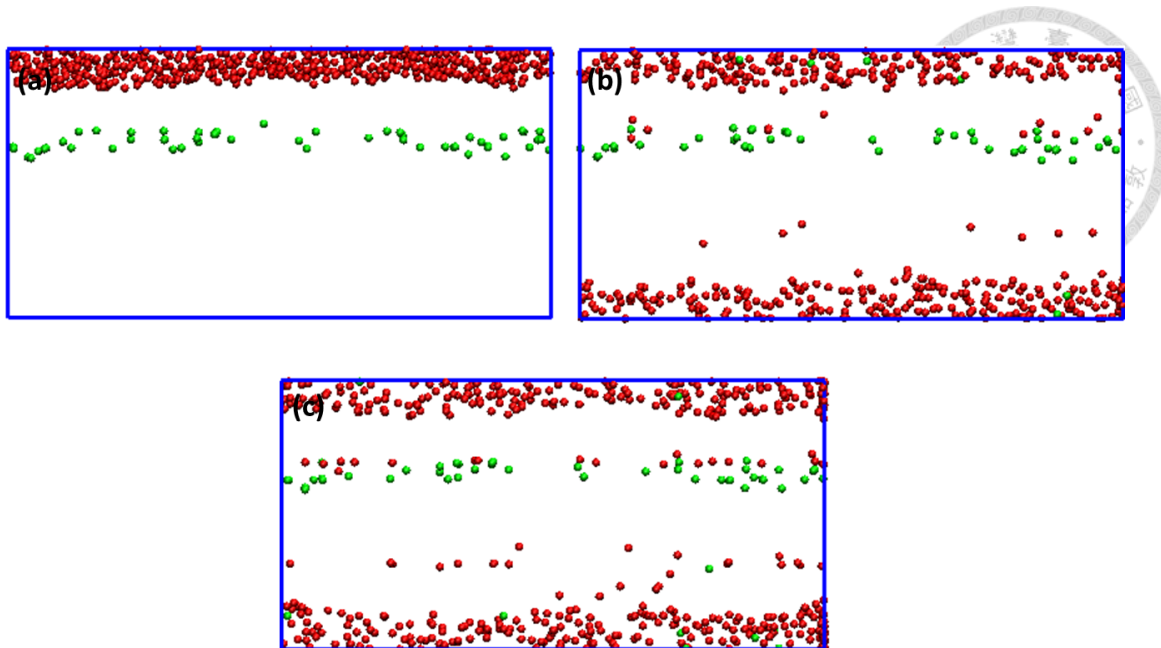
Figure 4.2-22 Motion of CH$_4$ atom during the simulation. Green and red denote the methane atoms initially located at the interface and gas phase, respectively. (a) t=0. (b) 42ns. (c) 84ns

To detect the distribution of concentration of methane varied from the interface to bulk phase, dividing the system into several layers and thickness of each layer is 4.125A which is the value of averaging radius of small cage and large cage. The results are shown in Figure 4.2-23.
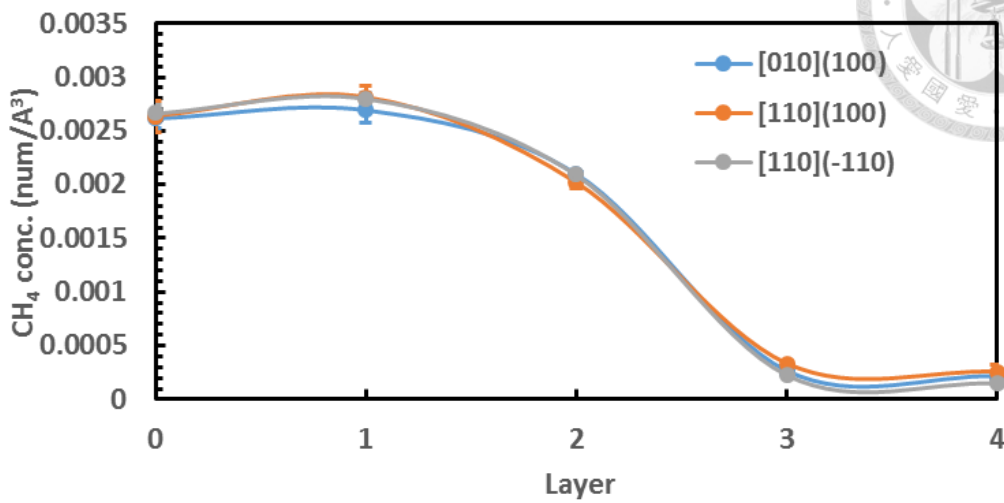
Figure 4.2-23 The CH$_4$ concentration in each of the layers compares with different orientation to CMI. Width of each of the layers is 4.125A which is the average of the radius of small cage and big cage of sI-hydrate. Layer 0 symbolizes the first layer under the CMI. Layer 1, 2, 3, and 4 denote 1st, 2nd, 3rd, and 4th layer over the CMI, respectively.
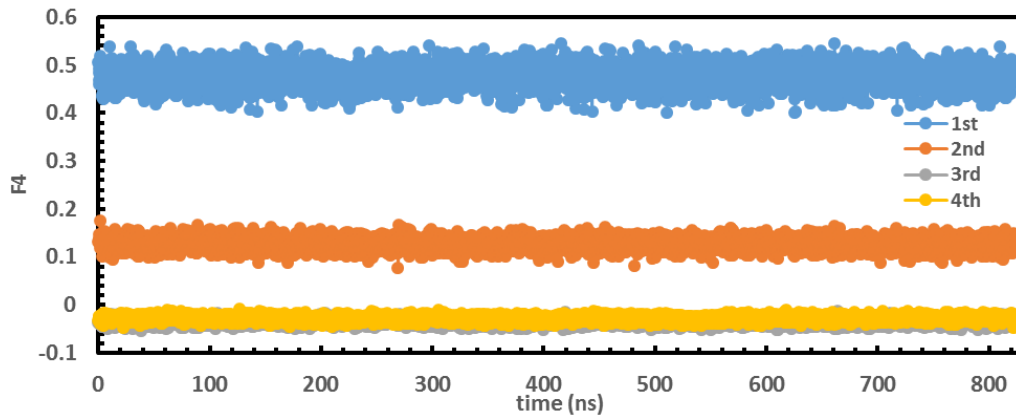
Figure 4.2-24 Average F4 value of H$_2$O molecules which are located in 1st, 2nd 3rd and 4th layer.

We find that methane concentration in the region within two layer thickness from interface is almost as same as that in sI-hydrate phase. If methane concentration at

96
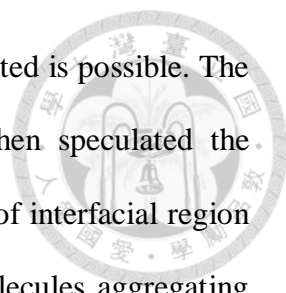
interface is enormous, that the kinetic coefficient by CFT overestimated is possible. The concept of CFT is measuring the fluctuation of interface and then speculated the thermodynamics and dynamics properties, in other word, the effect of interfacial region of CMI is the key of this manner. If there are lots of methane molecules aggregating around the interface, it indicates that the properties calculated by CFT method actually is based on the higher solubility condition at same specific temperature, this is to say, the other equilibrium state which at same temperature but higher pressure so that the solubility of methane is larger at phase-equilibrium condition. The sI methane-hydrate crystal growth rate is the function and sensitive of both temperature and pressure. The reason caused that the concentration of methane at interface (1st layer) huge is the methane molecules are trapped by hydrogen bonds which form and break promptly, this phenomenon is also observed in Figure 4.2-22, and the interfacial methane molecules are almost stagnant. However, it could not explain why the concentration of that in 2nd layer is still high. Maybe it is caused by morphology of the interface, we could not make any positive conclusion here, and however, we assure that there must some factors influence the interface of large CMI system and that makes the CH_4 concentration profile of this kind of system so distinct. Beside, average F4 value of H_2O molecules located in every layer is calculated, shown as Figure 4.2-24. This figure implies that the velocity of H_2O rearrangement from hydrate-like to fluid-like in 2nd layer is much faster than diffusion of CH_4 molecules.

4.2.8 Effect of parameters to CMI

In the last part, we want to analyze the effect of several parameters used in this work to the CMI. To differentiate the fluid, ice or hydrate-like of H_2O, using block-average analytic method is inevitable. However, there is a concern that because of block-average, the coordinate of atoms in system might be divergent from its real position. For example,

97

assuming the position x is the average position of overall high of CMI, if atom A at time t is located at position of x+Δx, and at x-Δx position at time t+n*Δt, using block-average of n size will cause the atom A located at average position x which means that atom A do not fluctuate if n is really huge. In order to examine the effect of block-average to the CMI, we plotted the wavelength of surface-wave against with the average result of interfacial height which is proceeded by Discrete Fourier transform at every different block size, shown as Figure 4.2-25. It is distinct that in lower frequency domain, the value of average Discrete-Fourier-transform-height is not influenced by block size at all; however, block size influences the higher frequency region. It is reasonable because the relaxation time of slow process (capillary wave) is above degree of nanosecond, in other words, the capillary waver is not affected if the block-size we used is much smaller than relaxation time of capillary waver process. In contrast, relaxation time of Rayleigh wave is very fast, almost dozens or hundreds picosecond, that will be affected by block size a lot, that is the reason why the data of high region in Figure 4.2-25 will change along with different block size.
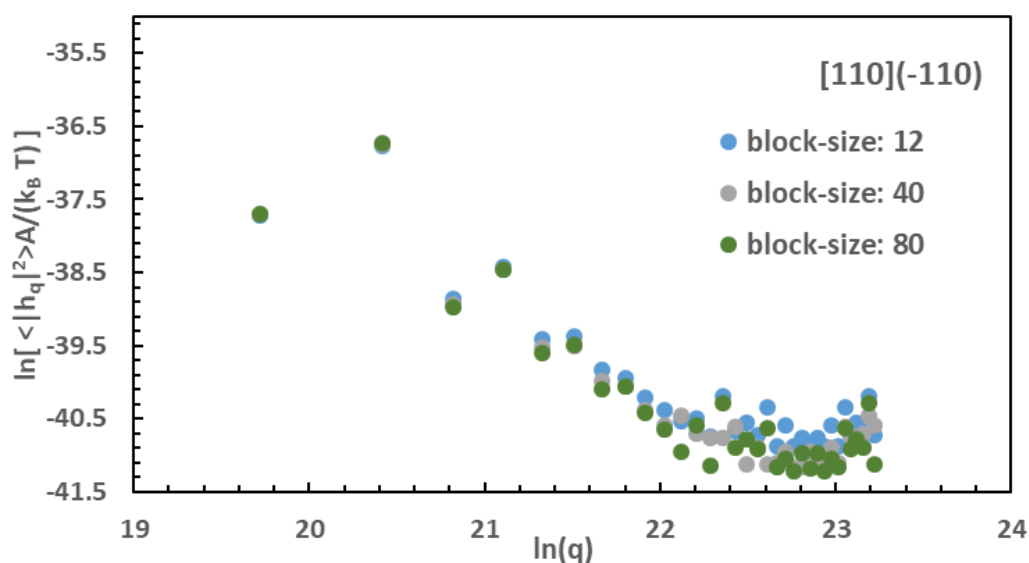
Figure 4.2-25 The effect of block size to the CMI
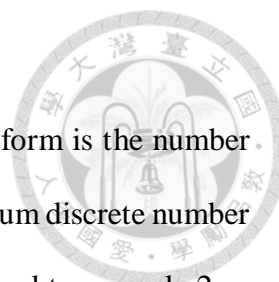
The other factor might affect the result of discrete Fourier transform is the number of points used to describe the CMI. Apparently, there must be a minimum discrete number of points needed to describe the continuous CMI, for example, it is hard to use only 2 or 3 etc. points to describe a plane. In this case, we used 30 points to describe the CMI, to prove this number is rational, we compared that with the 40 points, shown as Figure 4.2-26, and the results show that there is no difference between 30 and 40 points at low frequency region, in other words, 30 points is sufficient to describe the CMI.
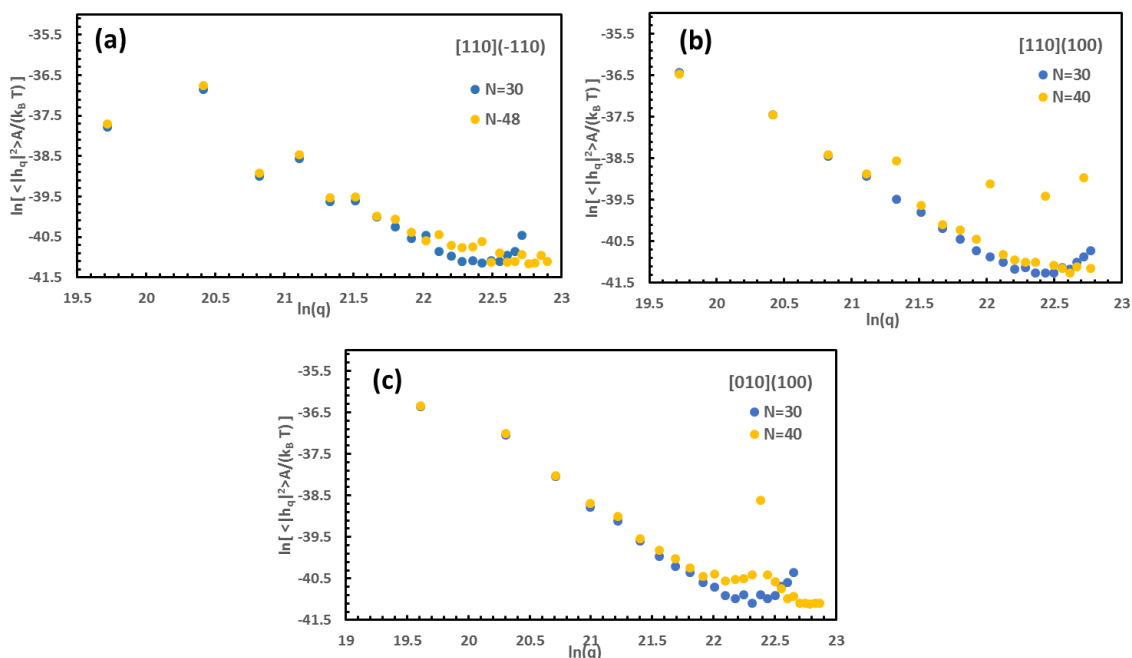
Figure 4.2-26 The effect of number of discrete points to the CMI (a) [110](-110). (b) [110](100). (c) [010](100).

Chapter 5   Conclusions
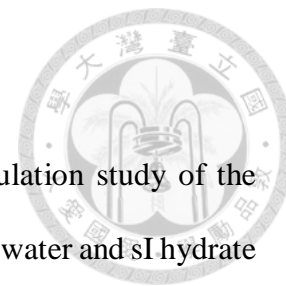
In this paper, we present a computer molecular dynamic simulation study of the crystal-melt interface for three different systems: TIP4P/Ice model of water and sI hydrate with TIP4P/Ice model, also SDS on hydrate with water, and OPLS_AA model. We focus on both the thermodynamics properties and the dynamics of surface waves for both I_h and sI hydrate crystal.

First, we generate an initial configuration in which a crystal slab is surrounded by its melt. The box geometry allows for the study of long wavelength capillary waves without having a prohibitively large number of molecules in the system (see Figure. 4 for an example). Then, we perform molecular dynamics simulations in the NV T ensemble at the melting temperature. The overall density of the system is comprised in between the coexistence densities of the fluid and the crystal phases, which guarantees that the system stays at coexistence throughout the NVT simulation. The area of the box side parallel to the interface (s and v directions) is chosen in such way that the solid phase is free of any stress.

Once we run the molecular dynamics simulations, we analyze the thermodynamics property (equation (37)) and dynamic autocorrelation function of the surface wave modes (equation (40)). To calculate both thermodynamics property and dynamics profile, we first obtain a function that describes the position of the interface, which we do by identifying the outermost crystalline particles of the solid slab. We show a feasibility of using F4 order parameter to identify the interface location of CMI system. In *ref.[31]*, it mentioned that simulations were not affected by the choice of the parameters needed to locate the interface or by the geometry of the box or the system size.
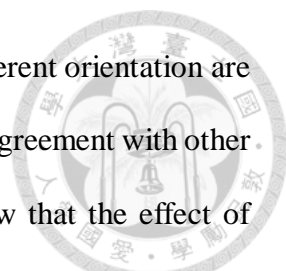
The average interfacial free energies of I_h and sI hydrate for different orientation are 29.24mN/m^2 and 34.60 mN/m^2, respectively. The results are in good agreement with other simulation methods and experimental works. Furthermore, we show that the effect of different orientations for sI hydrate to interfacial free energy is only 3%. To the best of our knowledge, this result has never been reported before our work in both the experiment and simulation field.

We also examine in detail the shape of the dynamic autocorrelation function as a function of the wave-vector q, and using a double exponential function describes the relaxation dynamics of crystal-melt surface waves and performs well for our system. This implies that there are two distinct time scales, fast and slow, involved in the relaxation of crystal-melt surface waves. The slow time scale is due to the recrystallization-melting occurring at the interface, and is governed by capillary forces. The fast relaxation is due to a combination of processes that readily alter the shape of the interface. We speculate these may be related to Rayleigh waves, sub-diffusion of the fluid and the attachment/detachment of particles to/from the crystal phase.

As the length scale of the capillary wave modes increases (or q decreases), the relaxation becomes increasingly dominated by the slow process and can be just described by a single exponential. Within the uncertainty of our data, we see that the characteristic time for the slow relaxation process is related to q by the power law: $\tau \propto q^{-2}$ for all systems.

We compare the relaxation dynamics of different systems in diffusive time units. We see that the crystal-melt interface of water relaxes about thirty times faster than that of sI hydrate crystal. We ascribe this difference to the presence of complicate hydrogen bond network and cage-like configuration of hydrate.

Furthermore, the kinetic coefficient of I_h/water obtained by CFT is same as both other simulation work and experiment work at the region degree of subcooling
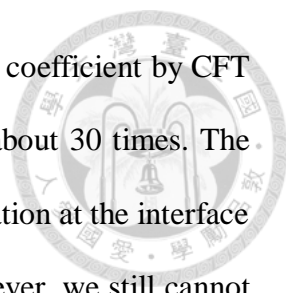
approaching to zero. In sI methane-hydrate/water system, the kinetic coefficient by CFT in this work is larger than other simulation and experiment work, about 30 times. The reason presumes that it is caused by the enormous methane concentration at the interface region whose concentration is same as methane-hydrate phase, however, we still cannot explain the fact that why the methane concentration is high within two layer thickness above the interface.

Last, we have already tried to calculate the interfacial free energy of hydrate/water with SDS adsorbing on the hydrate surface, however, that the SDS molecule will detach from the interface during the simulation cause failure to measure the interfacial free energy. The detaching phenomena should no happened according to other simulation work which calculate the adsorption free energy profile of SDS on hydrate interface. We still do not know the reason why that happened in the CMI system. However, there is a single run successfully shows that SDS could reduce the stiffness (interfacial free energy) of hydrate crystal, then according to CNT, the nucleation rate is faster almost 100 times than that without SDS.

References

1. Kvenvolden, K.A., *Gas hydrates-geological perspective and global change.* REVIEWS OF GEOPHYSICS-RICHMOND VIRGINIA THEN WASHINGTON-, 1993. **31**: p. 173-173.

2. Dickens, G.R., C. Paull, and P. Wallace, *Direct measurement ofin situ methane quantities in a large gas hydrate reservoir.* Nature, 1997. **385**: p. 426-428.

3. Haq, B.U., *Natural gas deposits - Methane in the deep blue sea.* Science, 1999. **285**(5427): p. 543-544.

4. Strobel, T.A., et al., *Properties of the clathrates of hydrogen and developments in their applicability for hydrogen storage.* Chemical physics letters, 2009. **478**(4): p. 97-109.

5. Sloan, E.D., *Clathrate Hydrate of Natural Gases: Revised and Expanded.* 1998.

6. Chatti, I., et al., *Benefits and drawbacks of clathrate hydrates: a review of their areas of interest.* Energy Conversion and Management, 2005. **46**(9-10): p. 1333-1343.

7. Davies, S.R., et al., *Hydrate plug dissociation.* Aiche Journal, 2006. **52**(12): p. 4016-4027.

8. Panter, J.L., et al., *Hydrate Plug Dissociation via Nitrogen Purge: Experiments and Modeling.* Energy & Fuels, 2011. **25**(6): p. 2572-2578.

9. Dickens, G.R., C.K. Paull, and P. Wallace, *Direct measurement of in situ methane quantities in a large gas-hydrate reservoir.* Nature, 1997. **385**(6615): p. 426-428.

10. Gornitz, V. and I. Fung, *POTENTIAL DISTRIBUTION OF METHANE HYDRATES IN THE WORLDS OCEANS.* Global Biogeochemical Cycles, 1994. **8**(3): p. 335-347.

11. Kvenvolden, K.A., *GAS HYDRATES - GEOLOGICAL PERSPECTIVE AND GLOBAL CHANGE.* Reviews of Geophysics, 1993. **31**(2): p. 173-187.

12. Sloan Jr, E.D. and C. Koh, *Clathrate hydrates of natural gases.* 2007: CRC press.

13. Boswell, R. and T.S. Collett, *Current perspectives on gas hydrate resources.* Energy & environmental science, 2011. **4**(4): p. 1206-1215.

14. Kuuskraa, V., S.H. Stevens, and K.D. Moodhe, *Technically recoverable shale oil and shale gas resources: an assessment of 137 shale formations in 41 countries outside the United States.* 2013.

15. Chen, L., et al., *Two dimensional fluid flow models at two gas hydrate sites offshore southwestern Taiwan.* Journal of Asian Earth Sciences, 2014. **92**: p. 245-253.

16. Gbaruko, B.C., et al., *Gas hydrates and clathrates: Flow assurance, environmental and economic perspectives and the Nigerian liquified natural gas project.* Journal of Petroleum Science and Engineering, 2007. **56**(1-3): p. 192-198.

17. Chapoy, A., R. Anderson, and B. Tohidi, *Low-pressure molecular hydrogen storage in semi-clathrate hydrates of quaternary ammonium compounds.* Journal of the American Chemical Society, 2007. **129**(4): p. 746-747.

18. Kim, D.-Y., Y. Park, and H. Lee, *Tuning clathrate hydrates: Application to hydrogen storage.* Catalysis Today, 2007. **120**(3-4): p. 257-261.

19. Prasad, P.S.R., Y. Sowjanya, and K.S. Prasad, *Micro-Raman investigations of mixed gas hydrates.* Vibrational Spectroscopy, 2009. **50**(2): p. 319-323.

20. Sugahara, T., et al., *Increasing Hydrogen Storage Capacity Using Tetrahydrofuran.* Journal of the American Chemical Society, 2009. **131**(41): p.

14616-14617.

21. Ogata, K., et al., *Hydrogen storage in trimethylamine hydrate: Thermodynamic stability and hydrogen storage capacity of hydrogen plus trimethylamine mixed semi-clathrate hydrate.* Chemical Engineering Science, 2010. **65**(5): p. 1616-1620.

22. Nakata, T., K. Hirai, and T. Takaoki, *Study of natural gas hydrate (NGH) carriers*, in *Proceedings of the 6th International conference on Gas Hydrates*. 2008: Vancouver, British Columbia, Canada.

23. Koh, D.-Y., et al., *Energy-efficient natural gas hydrate production using gas exchange.* Applied Energy, 2016. **162**: p. 114-130.

24. D. Jasnow, *Critical phenomena at interfaces,.* Rep. Prog.Phys.,, 1984.

25. V. Privman, *Fluctuating interfaces, surface tension and capillary waves: an introduction,.* Int. J. Mod. Phys. C,, 1992.

26. D. Nelson, T.P.a.S.W., *Statistical Mechanics of Membranes and Surfaces,.* Word Scientific, Singapore,, 2004.

27. S. C. Hardy, *A grain boundary groove measurement of the surface tension between ice and water,.* Philos. Mag.,, 1977,.

28. H. R. Pruppacher, *A new look at homogeneous ice nucleation in supercooled water drops.* J. Atmos. Sci.,, 1995,.

29. Granasy, L., T. Pusztai, and P.F. James, *Interfacial properties deduced from nucleation experiments: A Cahn-Hilliard analysis.* Journal of Chemical Physics, 2002. **117**(13): p. 6157-6168.

30. Ickes, L., et al., *Classical nucleation theory of homogeneous freezing of water: thermodynamic and kinetic parameters.* Physical Chemistry Chemical Physics, 2015. **17**(8): p. 5514-5537.

31. Benet, J., L.G. MacDowell, and E. Sanz, *Computer simulation study of surface wave dynamics at the crystal-melt interface.* Journal of Chemical Physics, 2014. **141**(3).

32. M. V. von Smoluchowski, ,Ann. Phys. , 1908.

33. Karma, A., *FLUCTUATIONS IN SOLIDIFICATION.* Physical Review E, 1993. **48**(5): p. 3441-3458.

34. Hoyt, J.J., M. Asta, and A. Karma, *Atomistic and continuum modeling of dendritic solidification.* Materials Science & Engineering R-Reports, 2003. **41**(6): p. 121-163.

35. Amini, M. and B.B. Laird, *Kinetic coefficient for hard-sphere crystal growth from the melt.* Physical Review Letters, 2006. **97**(21).

36. Benet, J., L.G. MacDowell, and E. Sanz, *A study of the ice-water interface using the TIP4P/2005 water model.* Physical Chemistry Chemical Physics, 2014. **16**(40): p. 22159-22166.

37. Rayleigh, L., *On Waves Propagated along the Plane Surface of an ElasticSolid.* 1885.

38. Baus, M. and C.F. Tejero, *INTERFACIAL HYDRODYNAMICS - A MICROSCOPIC APPROACH.* Journal of Chemical Physics, 1983. **78**(1): p. 483-496.

39. Tejero, C.F. and M. Baus, *VISCOELASTIC SURFACE-WAVES AND THE SURFACE-STRUCTURE OF LIQUIDS.* Molecular Physics, 1985. **54**(6): p. 1307-1324.

40. Pleiner, H., J.L. Harden, and P. Pincus, *SURFACE-MODES ON A VISCOELASTIC MEDIUM.* Europhysics Letters, 1988. **7**(5): p. 383-387.
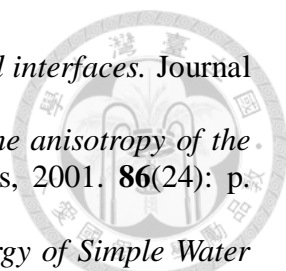
41. Jeng, U.S., et al., *Viscosity effect on capillary waves at liquid interfaces.* Journal of Physics-Condensed Matter, 1998. **10**(23): p. 4955-4962.

42. Hoyt, J.J., M. Asta, and A. Karma, *Method for computing the anisotropy of the solid-liquid interfacial free energy.* Physical Review Letters, 2001. **86**(24): p. 5530-5533.

43. Davidchack, R.L., et al., *Ice I-h-Water Interfacial Free Energy of Simple Water Models with Full Electrostatic Interactions.* Journal of Chemical Theory and Computation, 2012. **8**(7): p. 2383-2390.

44. Handel, R., et al., *Direct calculation of solid-liquid interfacial free energy for molecular systems: TIP4P ice-water interface.* Physical Review Letters, 2008. **100**(3).

45. Sanz, E., et al., *Homogeneous Ice Nucleation at Moderate Supercooling from Molecular Simulation.* Journal of the American Chemical Society, 2013. **135**(40): p. 15008-15017.

46. Espinosa, J.R., C. Vega, and E. Sanz, *The mold integration method for the calculation of the crystal-fluid interfacial free energy from simulations.* Journal of Chemical Physics, 2014. **141**(13).

47. Espinosa, J.R., C. Vega, and E. Sanz, *Ice-Water Interfacial Free Energy for the TIP4P, TIP4P/2005, TIP4P/Ice, and mW Models As Obtained from the Mold Integration Technique.* Journal of Physical Chemistry C, 2016. **120**(15): p. 8068-8075.

48. Kalogerakis, N.J., A. K. M.; Dholabhai, P. D.; Bishnoi,P. R.,, *Effect of Surfactants on Hydrate Formation Kinetics. .* In SPE International Symposium on Oilfield Chemistry; Society of Petroleum Engineers: New Orleans, LA,, 1993.

49. Okutani, K., Y. Kuwabara, and Y.H. Mori, *Surfactant effects on hydrate formation in an unstirred gas/liquid system: An experimental study using methane and sodium alkyl sulfates.* Chemical Engineering Science, 2008. **63**(1): p. 183-194.

50. Yoslim, J., P. Linga, and P. Englezos, *Enhanced growth of methane-propane clathrate hydrate crystals with sodium dodecyl sulfate, sodium tetradecyl sulfate, and sodium hexadecyl sulfate surfactants.* Journal of Crystal Growth, 2010. **313**(1): p. 68-80.

51. Sloan, E.D.C., A. K., *Clathrate Hydrates of Natural Gases,3rd ed.* 2008: CRC Press.

52. Sloan, E.D., *Fundamental principles and applications of natural gas hydrates.* Nature, 2003. **426**(6964): p. 353-359.

53. Sloan, E.D. and F. Fleyfel, *A MOLECULAR MECHANISM FOR GAS HYDRATE NUCLEATION FROM ICE.* Aiche Journal, 1991. **37**(9): p. 1281-1292.

54. Jr, E.D.S., *Proc. 69th Annual Gas Processors Convention.* Phoenix, 1990.

55. B. Muller-Bongartz, T.R.W.a.E.D.S.J., *Proc. Second International Offshore and Plar Engineering Conference.* 1992.

56. Sloan, R.L.C.a.E.D., *Proc. First International Conference Natural Gas Hydrates.* Annals of the New York Academy of Sciences, New Paltz, NY, 1994.

57. Himmelblau, D.M., J. Phys. Chem, 1959.

58. R. Radhakrishnan , B.L.T., J. Chem. Phys., 2002.

59. Hawtin, R.W., D. Quigley, and P.M. Rodger, *Gas hydrate nucleation and cage formation at a water/methane interface.* Physical Chemistry Chemical Physics, 2008. **10**(32): p. 4853-4864.

60. Walsh, M.R., et al., *Microsecond Simulations of Spontaneous Methane Hydrate Nucleation and Growth.* Science, 2009. **326**(5956): p. 1095-1098.

61. Barnes, B.C., et al., *Two-component order parameter for quantifying clathrate hydrate nucleation and growth.* Journal of Chemical Physics, 2014. **140**(16).

62. Barnes, B.C., et al., *Reaction Coordinate of Incipient Methane Clathrate Hydrate Nucleation.* Journal of Physical Chemistry B, 2014. **118**(46): p. 13236-13243.

63. Jacobson, L.C., W. Hujo, and V. Molinero, *Amorphous Precursors in the Nucleation of Clathrate Hydrates.* Journal of the American Chemical Society, 2010. **132**(33): p. 11806-11811.

64. Vatamanu, J. and P.G. Kusalik, *Observation of two-step nucleation in methane hydrates.* Physical Chemistry Chemical Physics, 2010. **12**(45): p. 15065-15072.

65. Pruppacher, H.R., *A NEW LOOK AT HOMOGENEOUS ICE NUCLEATION IN SUPERCOOLED WATER DROPS.* Journal of the Atmospheric Sciences, 1995. **52**(11): p. 1924-1933.

66. Sosso, G.C., et al., *Crystal Nucleation in Liquids: Open Questions and Future Challenges in Molecular Dynamics Simulations.* Chemical Reviews, 2016. **116**(12): p. 7078-7116.

67. Anderson, R., et al., *Experimental measurement of methane and carbon dioxide clathrate hydrate equilibria in mesoporous silica.* Journal of Physical Chemistry B, 2003. **107**(15): p. 3507-3514.

68. Jacobson, L.C. and V. Molinero, *Can Amorphous Nuclei Grow Crystalline Clathrates? The Size and Crystallinity of Critical Clathrate Nuclei.* Journal of the American Chemical Society, 2011. **133**(16): p. 6458-6463.

69. Knott, B.C., et al., *Homogeneous Nucleation of Methane Hydrates: Unrealistic under Realistic Conditions.* Journal of the American Chemical Society, 2012. **134**(48): p. 19544-19547.

70. Zhong, Y. and R.E. Rogers, *Surfactant effects on gas hydrate formation.* Chemical Engineering Science, 2000. **55**(19): p. 4175-4187.

71. Sun, Z.G., et al., *Experimental studying of additives effects on gas storage in hydrates.* Energy & Fuels, 2003. **17**(5): p. 1180-1185.

72. Zhang, J.S., et al., *Competitive adsorption between SDS and carbonate on tetrahydrofuran hydrates.* Journal of Colloid and Interface Science, 2010. **341**(2): p. 286-288.

73. Di Profio, P., et al., *Surfactant promoting effects on clathrate hydrate formation: Are micelles really involved?* Chemical Engineering Science, 2005. **60**(15): p. 4141-4145.

74. Watanabe, K., S. Imai, and Y.H. Mori, *Surfactant effects on hydrate formation in an unstirred gas/liquid system: An experimental study using HFC-32 and sodium dodecyl sulfate.* Chemical Engineering Science, 2005. **60**(17): p. 4846-4857.

75. Zhang, J.S., S. Lee, and J.W. Lee, *Does SDS micellize under methane hydrate-forming conditions below the normal Krafft point?* Journal of Colloid and Interface Science, 2007. **315**(1): p. 313-318.

76. Hockney, R.W., S.P. Goel, and J.W. Eastwood, *10000 Particle Molecular Dynamics Model with Long-Range Forces.* Chemical Physics Letters, 1973. **21**(3): p. 589-591.

77. Verlet, L., *COMPUTER EXPERIMENTS ON CLASSICAL FLUIDS .I. THERMODYNAMICAL PROPERTIES OF LENNARD-JONES MOLECULES.* Physical Review, 1967. **159**(1): p. 98-&.

78. Toukmaji, A.Y. and J.A. Board Jr, *Ewald summation techniques in perspective: A survey.* Computer Physics Communications, 1996. **95**(2-3): p. 73-92.

79. Kittel, C.H.K., *Thermal Physics, 2nd* 1980, San Francisco: W.H. Freeman and

106

Company. P 31.

80.   Landau, L.D.L., E.M., *Statistical Physics. Pergamon Press.* 1980.

81.   Hoover, W.G., *CANONICAL DYNAMICS - EQUILIBRIUM PHASE-SPACE DISTRIBUTIONS.* Physical Review A, 1985. **31**(3): p. 1695-1697.

82.   Berendsen, H.J.C., et al., *MOLECULAR-DYNAMICS WITH COUPLING TO AN EXTERNAL BATH.* Journal of Chemical Physics, 1984. **81**(8): p. 3684-3690.

83.   Berendsen, H.J.C., *Transport Properties Computed by Linear Response through Weak Coupling to a Bath*, in *Computer Simulation in Materials Science*, M. Meyer and V. Pontikis, Editors. 1991, Springer Netherlands. p. 139-155.

84.   Parrinello, M. and A. Rahman, *POLYMORPHIC TRANSITIONS IN SINGLE-CRYSTALS - A NEW MOLECULAR-DYNAMICS METHOD.* Journal of Applied Physics, 1981. **52**(12): p. 7182-7190.

85.   Allen, M.P., Tildesley, D. J, *Computer Simulations of Liquids.* 1987: Oxford: Oxford Science Publications.

86.   Shuttleworth, R., *THE SURFACE TENSION OF SOLIDS.* Proceedings of the Physical Society of London Section A, 1950. **63**(365): p. 444-457.

87.   Evans, R., *MOLECULAR THEORY OF CAPILLARITY - ROWLINSON,JS, WIDOM,B.* Journal of the Chemical Society-Faraday Transactions Ii, 1983. **79**: p. 643-644.

88.   Pronk, S., et al., *GROMACS 4.5: a high-throughput and highly parallel open source molecular simulation toolkit.* Bioinformatics, 2013. **29**(7): p. 845-854.

89.   Module, F., *Material Studio 6.0.* Accelrys Inc., San Diego, CA, 2011.

90.   Hayward, J.A. and J.R. Reimers, *Unit cells for the simulation of hexagonal ice.* Journal of Chemical Physics, 1997. **106**(4): p. 1518-1529.

91.   Takeuchi, F., et al., *Water proton configurations in structures I, II, and H clathrate hydrate unit cells.* Journal of Chemical Physics, 2013. **138**(12).

92.   Bernal, J. and R. Fowler, *A theory of water and ionic solution, with particular reference to hydrogen and hydroxyl ions.* Journal of Chemical Physics, 1933. **1**(8): p. 515-548.

93.   Abascal, J., et al., *A potential model for the study of ices and amorphous water: TIP4P/Ice.* The Journal of chemical physics, 2005. **122**: p. 234511.

94.   Kaminski, G.A., et al., *Evaluation and reparametrization of the OPLS-AA force field for proteins via comparison with accurate quantum chemical calculations on peptides.* The Journal of Physical Chemistry B, 2001. **105**(28): p. 6474-6487.

95.   Luzar, A. and D. Chandler, *Structure and hydrogen bond dynamics of water–dimethyl sulfoxide mixtures by computer simulations.* The Journal of chemical physics, 1993. **98**(10): p. 8160-8173.

96.   Lechner, W. and C. Dellago, *Accurate determination of crystal structures based on averaged local bond order parameters.* Journal of Chemical Physics, 2008. **129**(11).

97.   Rodger, P.M., T.R. Forester, and W. Smith, *Simulations of the methane hydrate methane gas interface near hydrate forming conditions.* Fluid Phase Equilibria, 1996. **116**(1-2): p. 326-332.

98.   Liang, S. and P.G. Kusalik, *Nucleation of Gas Hydrates within Constant Energy Systems.* Journal of Physical Chemistry B, 2013. **117**(5): p. 1403-1410.

99.   Yan, J.Y. and G.N. Patey, *Molecular Dynamics Simulations of Ice Nucleation by Electric Fields.* Journal of Physical Chemistry A, 2012. **116**(26): p. 7057-7064.

100.   Krynicki, K., C.D. Green, and D.W. Sawyer, *PRESSURE AND TEMPERATURE-DEPENDENCE OF SELF-DIFFUSION IN WATER.* Faraday Discussions, 1978.

66: p. 199-208.

101. Weiss, V.C., et al., *Kinetic aspects of the thermostatted growth of ice from supercooled water in simulations.* Journal of Chemical Physics, 2011. **135**(3).

102. Wu, J.Y., et al., *Molecular Dynamics Study on the Growth Mechanism of Methane plus Tetrahydrofuran Mixed Hydrates.* Journal of Physical Chemistry C, 2015. **119**(34): p. 19883-19890.

103. V. F. Petrenko and R. W. Whitworth, *Physics of Ice.* Oxford University Press, Oxford, 1999.

104. Gayet, P., et al., *Experimental determination of methane hydrate dissociation curve up to 55 MPa by using a small amount of surfactant as hydrate promoter.* Chemical Engineering Science, 2005. **60**(21): p. 5751-5758.

105. Gupta, A., et al., *Measurements of methane hydrate heat of dissociation using high pressure differential scanning calorimetry.* Chemical Engineering Science, 2008. **63**(24): p. 5848-5853.

106. Wu, J.Y., et al., *Molecular dynamics study on the nucleation of methane plus tetrahydrofuran mixed guest hydrate.* Physical Chemistry Chemical Physics, 2016. **18**(15): p. 9935-9947.

107. Zhang, Z.C., M.R. Walsh, and G.J. Guo, *Microcanonical molecular simulations of methane hydrate nucleation and growth: evidence that direct nucleation to sI hydrate is among the multiple nucleation pathways.* Physical Chemistry Chemical Physics, 2015. **17**(14): p. 8870-8876.

108. Kara, M. and K. Kurkisuonio, *SYMMETRIZED MULTIPOLE ANALYSIS OF ORIENTATIONAL DISTRIBUTIONS.* Acta Crystallographica Section A, 1981. **37**(MAR): p. 201-210.

109. Sun, D.Y., et al., *Crystal-melt interfacial free energies in hcp metals: A molecular dynamics study of Mg.* Physical Review B, 2006. **73**(2).

110. Hardy, S.C., *A grain boundary groove measurement of the surface tension between ice and water.* 1977.

111. Koo, K.K., R. Ananth, and W.N. Gill, *TIP SPLITTING IN DENDRITIC GROWTH OF ICE CRYSTALS.* Physical Review A, 1991. **44**(6): p. 3782-3790.

112. English, N.J. and J.M.D. MacElroy, *Perspectives on molecular simulation of clathrate hydrates: Progress, prospects and challenges.* Chemical Engineering Science, 2015. **121**: p. 133-156.

113. Fehlner, W.R. and S.H. Vosko, *PRODUCT REPRESENTATION FOR CUBIC HARMONICS AND SPECIAL DIRECTIONS FOR DETERMINATION OF FERMI-SURFACE AND RELATED PROPERTIES.* Canadian Journal of Physics, 1976. **54**(21): p. 2159-2169.

114. Yagasaki, T., M. Matsumoto, and H. Tanaka, *Adsorption Mechanism of Inhibitor and Guest Molecules on the Surface of Gas Hydrates.* Journal of the American Chemical Society, 2015. **137**(37): p. 12079-12085.

115. Bertolazzo, A.A., et al., *The Clathrate-Water Interface Is Oleophilic.* Journal of Physical Chemistry Letters, 2018. **9**(12): p. 3224-3231.

116. Pruppacher, H.R., *INTERPRETATION OF EXPERIMENTALLY DETERMINED GROWTH RATES OF ICE CRYSTALS IN SUPERCOOLED WATER.* Journal of Chemical Physics, 1967. **47**(5): p. 1807-+.

117. Rozmanov, D. and P.G. Kusalik, *Temperature dependence of crystal growth of hexagonal ice (I-h).* Physical Chemistry Chemical Physics, 2011. **13**(34): p. 15501-15511.

118. Taylor, C.J., et al., *Macroscopic investigation of hydrate film growth at the*

hydrocarbon/water interface. Chemical Engineering Science, 2007. **62**(23): p. 6524-6533.